Geometrical Analysis of Parabolic Trough Solar Collector

Mohamed Salim Djenane, Seddik Hadji, and Omar Touhami

Abstract—The geometric of the parabolic trough collector (PTC) is a field that should be paid special attention, knowing that a better geometry induces a better efficiency and lower costs. Nowadays, many types of geometry exist, such as LS-2, LS-3, Euro trough, ENEA, SGX-2, Sener trough, Helio trough, Sky trough, Ultimate trough. This paper deals with a geometrical analysis of PTC. The analysis is based on the coefficient of deviation angle to highlight the effect of PTC (LS-2) parameters on the optical efficiency. The effects of focal length, tube diameter, and collector width on the coefficient of deviation angle have been considered using a two-dimensional problem, and the simulation has been done employing MATLAB software. The derived results confirm that the tube diameter is the parameter most influencing compared to the other parameters. In addition, the width and length of the Euro trough, Helio trough, and Ultimate trough were considered to simulate thermal efficiency. The best observed performance is that of the Ultimiate trough, which presents a 2% higher difference in efficiency and also represents a better size, which allows reducing the number of units to be assembled in the solar field. That leads to reducing the count of motors, sensors, connection joints, foundations, controllers, pylons.

***Keywords*—Parabolic trough, Geometric, Coefficient of deviation angle, Efficiency.**

Nomenclature

β: Deviation angle $(degree)$.
d: Tube diameter (m).
f: Focal length (m).
B: Collector's width (m).
A_a: Aperture Area of the mirror (m^2).
A_{ro}: Receiver outer area (m^2).
A_{ri}: Receiver inner area (m^2).
L: Collector length (m).
D_{ri}: Receiver inner diameter (m).
D_{ro}: Receiver outer diameter (m).
D_{ci}: Cover inner diameter (m).
D_{co}: Cover outer diameter (m).
T: Temperature (K).
C_p: Specific heat capacity $(Jkg^{-1}K^{-1})$.
T_{am}: Ambient temperature (K).
μ: Dynamic viscosity.
k: Thermal conductivity $(Wm^{-1}K^{-1})$.
ρ: Density (kg/m^3)..
m: Mass flow rate (kg/s).
Re: Reynolds number.
Pr: Prandtl number.
Nu: Nusselt number.
h: Heat transfer coefficient fluid/absorber (w/m^2K).
h_{out}: Heat transfer coefficient cover/environment (w/m^2K).
σ: Stefan Boltzmann constant.

Manuscript received February 7, 2024; revised July 12, 2024.

M.S. Djenane and O. Touhami is with the Electrical Engineering Department, Ecole Nationale Polytechnique, Algiers, ALGERIA (e-mail: mohamed_salim.djenane@g.enp.edu.dz, omar.touhami@g.enp.edu.dz).

S. Hadji is with the Electrical Engineering Department, Ecole Nationale Polytechnique, and Ecole Supérieure des Sciences Appliquées, Algiers, ALGERIA (e-mail: seddik.hadji@g.essaa.edu.dz).

Digital Object Identifier (DOI): 10.53907/enpesj.v4i2.258

I. Introduction

Nowadays, the main primary sources used in power plants are fossil fuels. Unfortunately, these raise major ecological concerns. They represent exhaustible sources of energy and constitute reservoirs of toxic wastes. There is also the risk linked to radioactivity in nuclear power plants. The world is then moving towards the solution of exploiting renewables energies to remedy these problems [1]. Among renewable energies, solar energy is the most used source for producing electricity, especially through CSP (Concentrated Solar Power) systems. Among CSP systems is found the parabolic trough system, which is the most successful worldwide [2], as many parabolic trough solar power plants are built in many countries such as the USA, Spain, Morocco, Algeria.

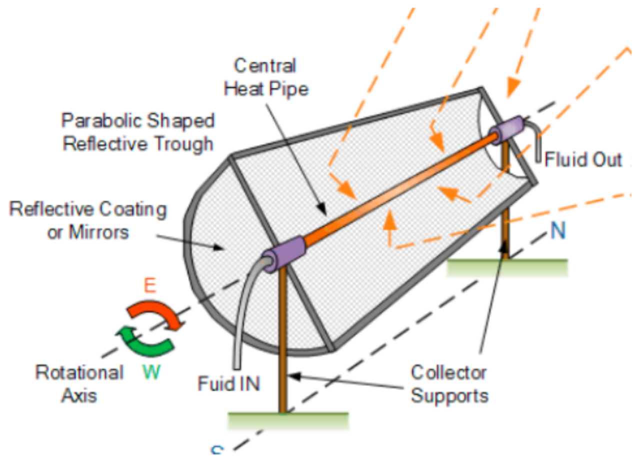

Fig. 1: Parabolic Trough Collector basic elements [15]

Many works have been carried out focusing on the geometrical shape of parabolic trough solar collector [3-5]. The geometrical modifications are done on absorber tubes to improve the PTC's performance such as the circular-trapezoidal absorber tube [6], sinusoidal absorber tube [7], and helecoidal absorber tube [8]. Also, a modification is introduced inside the absorber tube, as seen in Single-sided spiral ribbed absorber tube [9], and in absorber tube with pin fin array insertion [10]. In addition, geometrical analyses have been done on PTC, among which the geometric optimization based on the local concentration ratio using the Monte Carlo method [11], and also on the optical performance employing particle swarm optimization algorithm [12]. An optics and thermodynamics analysis have been carried out on several configurations, considering the concentrating ration and cost factor [13]. However, changes are simultaneously made in the internal and external geometry of the receiving tube in [14].

In this paper, the variation of the coefficient of deviation angle is considered in view of simulating the effect of focal length, tube diameter and collector's width on the optical efficiency of PTC (LS-2). These effects are determined as a function of deviation angle. Then an interpretation is performed showing that the tube diameter influences the optical efficiency more than the focal length and collector's width. Moreover, Euro trough, Helio trough, Ultimate trough are examined to highlight the effects of aperture area and tube diameter length. The Ultimate Trough is the most efficient type regarding the thermal efficiency.

This paper is organized in six sections: The parabolic trough collector is presented in section II. Then the coefficient of deviation angle is studied in section III, showing the effects of focal length, tube diameter, and collector's width (Section IV). Section V is devoted to thermal efficiency considering Euro trough, Helio trough, and Ultimate trough types. Finally, the conclusions of this work are presented in section VI.

II. Parabolic Trough Collector

Parabolic trough collector is conceived by a long mirror in parabolic shape, an absorber tube placed at the focal line of the collector, in which a heat transfer fluid flows (Fig. 1). Glasses to reduce heat losses by convection cover the absorber tube. The PTC is attached to a support and a system assuring the tracking of the sun.

The parabolic trough types considered in this study are: LS-2, Euro trough, Helio trough and Ultimate trough, focusing on the geometrical analysis.

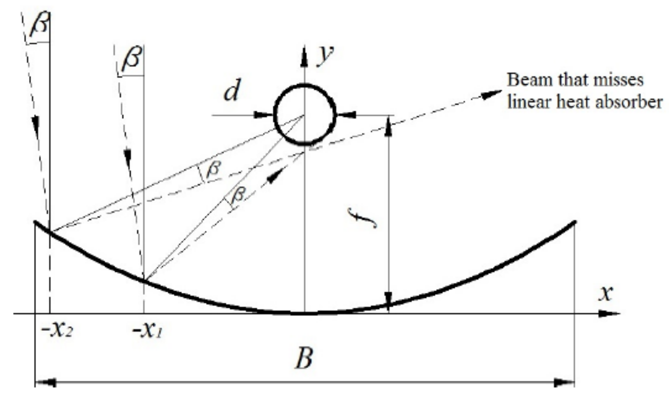

Fig. 2: Small deviation of incidence angle of sun beam at parabolic trough collector [16]

III. Coefficient of deviation angle

The coefficient of deviation angle depends on the deviation angle (η_β), it takes into account the decrease in thermal performance due to small deviation angle between the solar beam and focal plane. The small deviation of incidence angle of sun beam at parabolic trough collector is shown in Fig. 2.

Figure 2 shows a cross section of parabolic trough collector on which can be seen the effect of small deviation angle, the rays coming onto the collector at the point with the coordinate $-x_2$ can not reach the absorber tube and is lost. Also the rays with coordinates $(-x_i; i > 2)$ can not reach the absorber tube neither. It can be observed that at each point of collector there is a defined interval of the deviation angle $[\beta_{min}; \beta_{max}]$ where the rays reach the absorber tube. After analyzing this two dimensional problem, the coefficient of deviation angle η_β can be defined as, [16, 17]:

$$\eta_\beta = \begin{cases} 1, & \beta \leq \beta_{min} \\ \frac{4f}{B}\sqrt{\frac{d}{2f sin(\beta)}} - 1, & \beta_{min} \leq \beta \leq \beta max \\ 0, & \beta \leq \beta_{max} \end{cases} \tag{1}$$

with β_{min} and β_{max} being determined as, [5]:

$$\beta_{min} = \arcsin(\frac{8fd}{16f^2 + B^2}) \tag{2}$$

$$\beta_{max} = \arcsin(\frac{d}{f}) \tag{3}$$

Figure 3 shows the variation of the coefficient of deviation angle versus deviation angle (β, radians), obtained for $B = 2.75m$; $f = 0.81m$ and $d = 0.04m$.

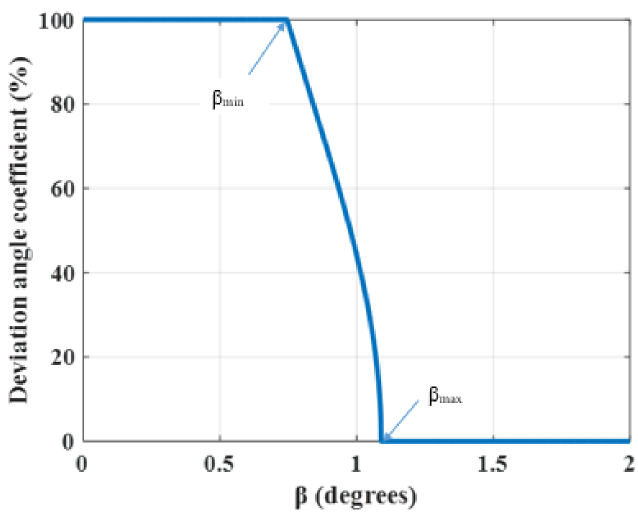

Fig. 3: variation of the coefficient of deviation angle versus the deviation angle

It is to be noted that, actually, the interval of deviation angle (β) referred to above represents the concentrator's operating margin, i.e. it exhibits a significant efficiency within this margin, particularly when approaching β_{min}. So, the concentrator should be better operated from 0 to β_{max}.

IV. EFFECT OF PARABOLIC TROUGH PARAMETERS ON THE COEFFECIENT OF DEVIATION ANGLE

A. *Effect of focal lenght*

To evaluate the influence of the focal length on the coefficient of deviation angle, the collector's width and tube diameter are fixed and the focal length is varied. The shape of the collector evoles as shows Fig. 3, and the variation of the coefficient of deviation angle is shown in Fig. 4. The equation of the parabola is given by Eq. (4).

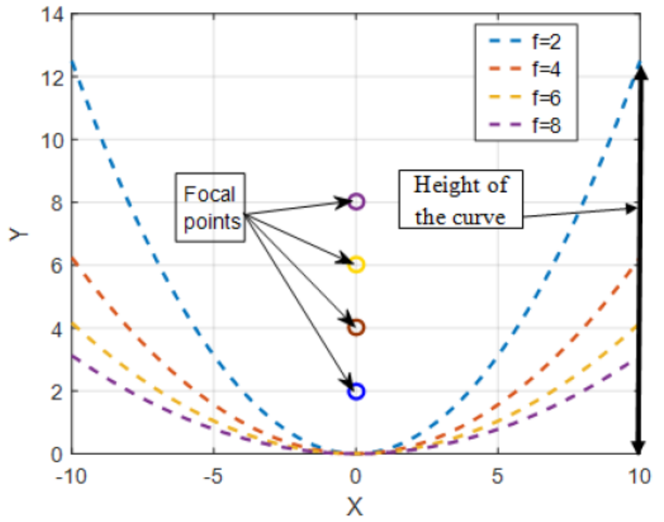

Fig. 4: variation of the collector shape versus coordinate x with the focal length as a parameter.

$$Y(x) = \frac{x^2}{4f} \tag{4}$$

Figure 4 is obtained by varying the focal length for the following values: $2m, 4m, 6m$ and $8m$. It can be observed that the more the focal length is increased the more the width decreases and consequently the collector's area decreases and the costs decrease as well.

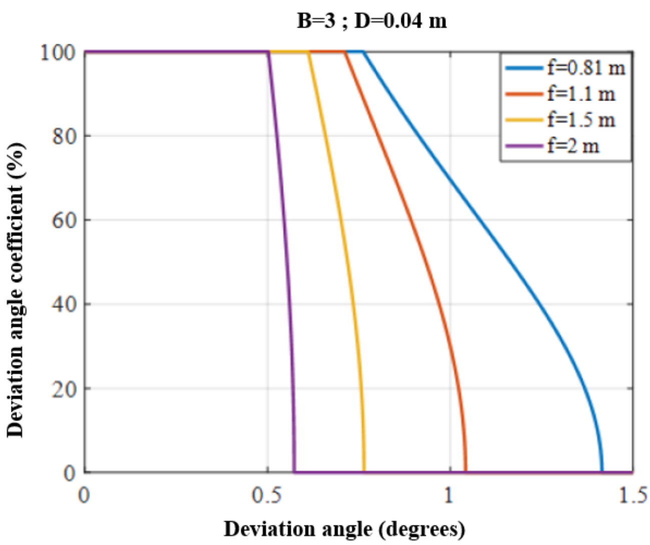

Fig. 5: Variation of the coefficient of deviation versus deviation angle with the focal length as a parameter.

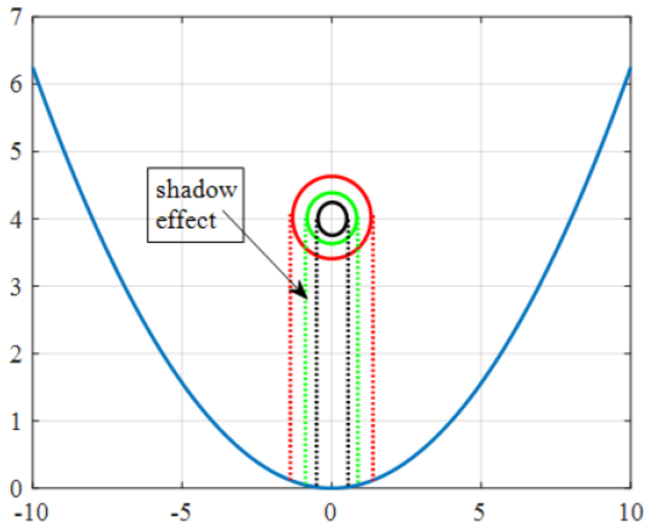

Fig. 6: Shadow effect with variation of tube diameter

The plot relative to the evolution of the coefficient of deviation angle versus the deviation angle with the focal length as a parameter is shown in Fig. 5. From this latter, it can be seen that the operating margin of the concentrator (within which the solar rays reach the absorber tube) goes larger as the focal length becomes smaller. And when the margin is large it means that the angle of incidence has a large margin of variation, For example, comparing for $f_1 = 0.81m$ and $f_2 = 1.1m$, gives for: $f_2 = 1.1m$, $\beta = 1$ degree, and $\eta_\beta = 29.95\%$, and for $f_1 = 0.81m$, $\beta = 1.314$, and $\eta_\beta = 29.95\%$, i.e. the same value of the coefficient of deviation angle η_β for both the focal length values. Note that the margin $[1.314; \beta_{max-f_1}]$ is higher compared to $[1; \beta_{max} - f_2]$. In other words, $0.101 degrees > 0.042 degrees$.

Now assume the effect of wind or an inaccuracy in the tracking system exists. Then at a given moment the concentrator changes its position which causes a change in the angle of incidence of 0.042 degrees implying that $\eta_{\beta-f2} = 0\%$ against $\eta_{\beta-f_1} = 22.58\%$. So, it is beneficial to work adopting a large margin. However, lowering the focal point involves increasing the aperture area and, subsequently, incresing the costs.

B. *Effect of tube diameter*

To see the influence of the tube diameter on the coefficient of deviation angle, the collector's width and focal length are fixed and the tube diameter is varied.

Figure 6 shows the shadow effect due to the increase of the tube diameter.

It can be seen that if the diameter of the absorber tube is increased, the shadow area at the surface of the collector increases and then the corresponding materials do not contribute to the reflection process thus causing an increase in the costs. On the other hand, it is advantageous to increase the tube diameter, as shown in Fig. 7. This latter shows the variations of the coefficient of deviation angle with the tube diameter (d) as a parameter for the following values of $(d = 0.04m; d = 0.06m; d = 0.08m$ and $d = 0.1m)$.

It can be seen that the increase in diameter of the receiver (d) increases the margin within which the rays reach the absorber

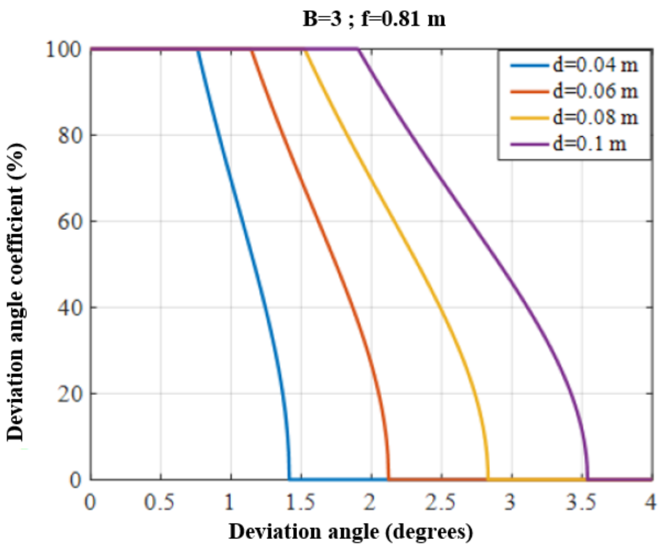

Fig. 7: Variation of the coefficient of deviation angle versus deviation angle with the tube diameter as a parameter.

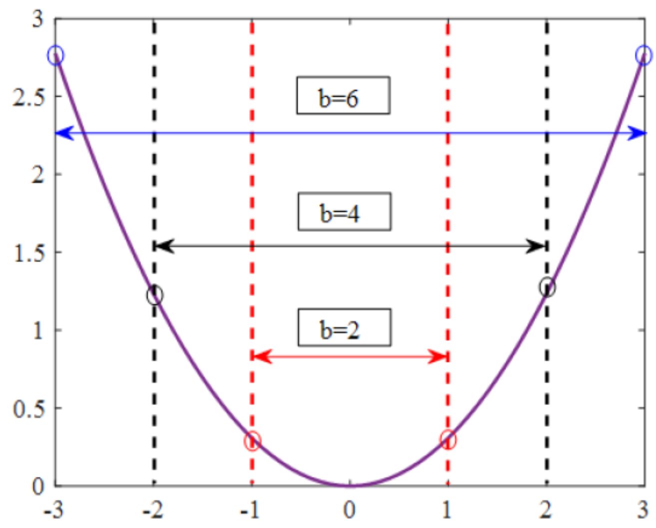

Fig. 8: Variation of collector's width

tube.

C. *Effect of collector's width*

Proceeding the same way, to see the influence of the collector's width on the coefficient of deviation angle, the tube diameter and focal length are fixed and the collector's width is varied. Figure 8 is obtained for the following values of the collector's width: 2m, 4m and 6m.

It can be seen from Fig. 8 that if the collector's width is increased, a larger sensing section is obtained, but still remains the disadvantage related to the costs. The variations of the coefficient of deviation angle against the collector's width are shown in Fig. 9. From this latter, it appears that the collector's width does not affect β_{max} but influences β_{min}. The variation of the coefficient of deviation angle according collector's width is given by Fig. 9. So, the increase of (B) decreases β_{min}, which increases the margin of variation of β, and that because of the increase in the collector's area.

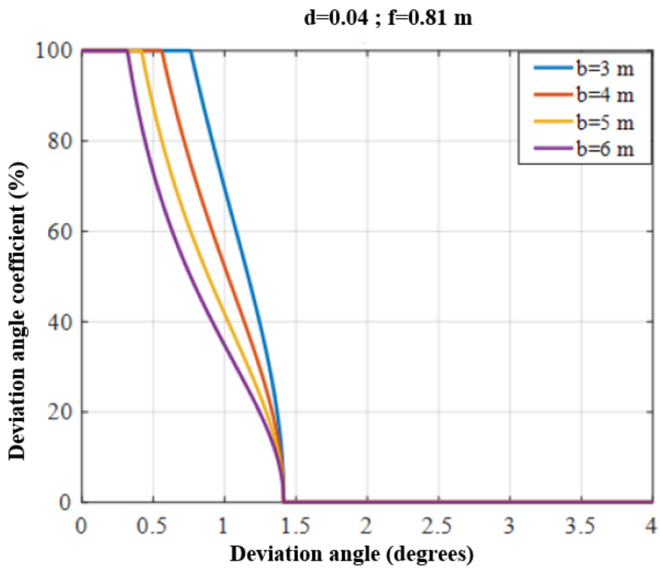

Fig. 9: Variation of the coefficient of deviation angle versus deviation angle with the collector's width as a parameter.

V. Thermal analysis

In this section, three types of parabolic trough collector are examined, the Euro trough, Helio trough, and Ultimate trough, to highlight the effect of the geometry of the collector on the thermal efficiency.

The three types are considered here as concieved with the same materials, the only one difference being in the collector's area.

The energy balanced model is used to simulate the thermal efficiency. The different heat modes are represented in Fig.10 while the Euro trough, Helio trough and Ultimate trough are represented in Fig. 11.

The solar energy comes onto the collector, then will be reflected towards the absorber tube, and the heat will be transferd to the heat transfer fluid with some losses that should be considered.

The heat coming onto the collector can be expressed as, Eq. (5).

$$Q_s = A_a * G_b \tag{5}$$

The useful heat absorbed by the heat transfer fluid is determined by Eq. (6).

$$Q_u = mC_p(T_{out} - T_{in}) \tag{6}$$

And the heat losses are determined by Eq. (7).

$$Q_{loss} = h_{out}A_{co}(T_{T_c} - T_{am}) + A_{co}\sigma\varepsilon_c(T_c^4 - T_{am}^4) \tag{7}$$

The useful heat can then be written as follows :

$$Q_u = Q_s\eta_{op} - Q_{loss} \tag{8}$$

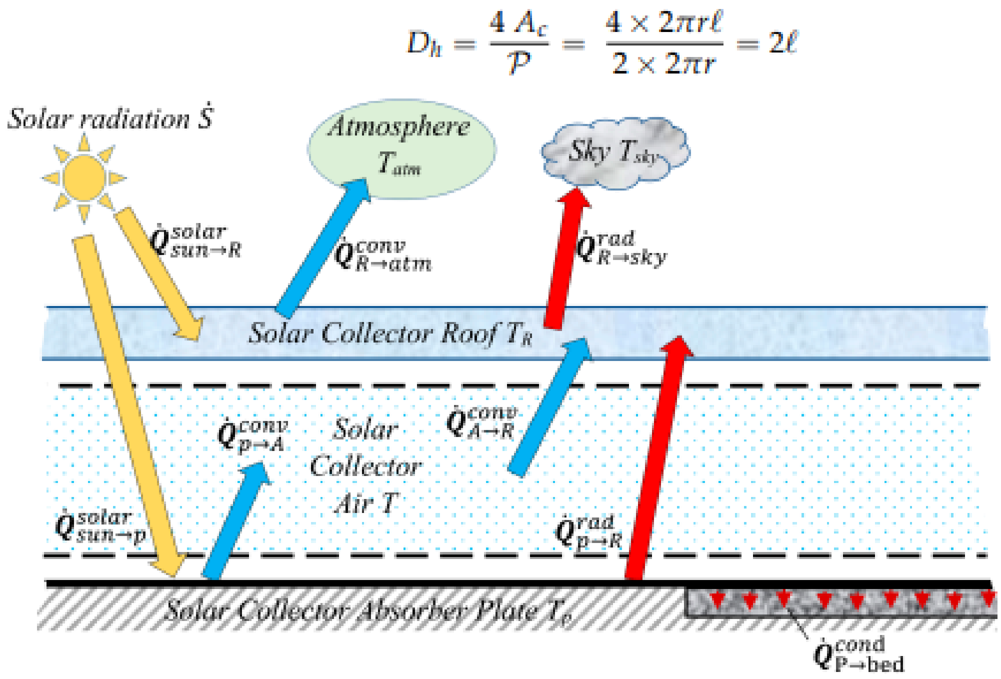

Fig. 10: Heat transfert modes [18]

Which is rewritten as a function of receiver temperature as (Eq. (9)):

$$Q_u = hA_{ri}(T_r - T_{fm}) \tag{9}$$

Finally, the thermal efficiency is evaluated by Eq. (10).

$$\eta_{th} = \frac{Q_u}{Q_s} \tag{10}$$

The fluid used in this study is the Syltherm 800, its parameters are as defined below :

The dynamic viscosity is determined as follows:

$$\begin{aligned}\mu = (5.14887*10^4 - \\ (9.61656*10^2)*Tam + \\ 7.50207*(Tam^2) - \\ (3.12468*10^{-2})*(Tam^3) + \\ (7.32194*10^{-5})*(Tam^4) - \\ (9.14636*10^{-8})*(Tam^5) + \\ (4.75624*10^{-11})*(Tam^6))*10^{-3}\end{aligned} \tag{11}$$

While the thermal conductivity is evaluated as follows :

$$k = 1.90134*10^{-1} - (1.88053*10^{-4})*T_{am} \tag{12}$$

On ther other hand, the density is expressed as follows :

$$\begin{aligned}\rho = 1.2691*103 - 1.52115*T_{am} + \\ (1.79133*10^{-3})*(T^2_{am}) - \\ (1.67145*10^-6)*(T^3_{am})\end{aligned} \tag{13}$$

And the specific heat capacity is expressed by the following equation :

$$Cp = (1.10787 + (1.70736*10^{-3})*T_{am})*1000 \tag{14}$$

Finally, the mass flow is determined by Eq. (15).

$$m = \rho * V \tag{15}$$

Reynolds number, Prandtl number, and Nusselt number are defined successively by Eqs. (16-18).

$$Re = 4*m/(\Pi * D_{ri} * \mu), \tag{16}$$

$$Pr = \mu * Cp/k, \tag{17}$$

and,

$$Nu = 0.023*(Re^{0.8})*(Pr^{0.4}) \tag{18}$$

The heat transfer coefficient is then determined by Eq. (19).

$$h = (k*Nu)/D_{ri} \tag{19}$$

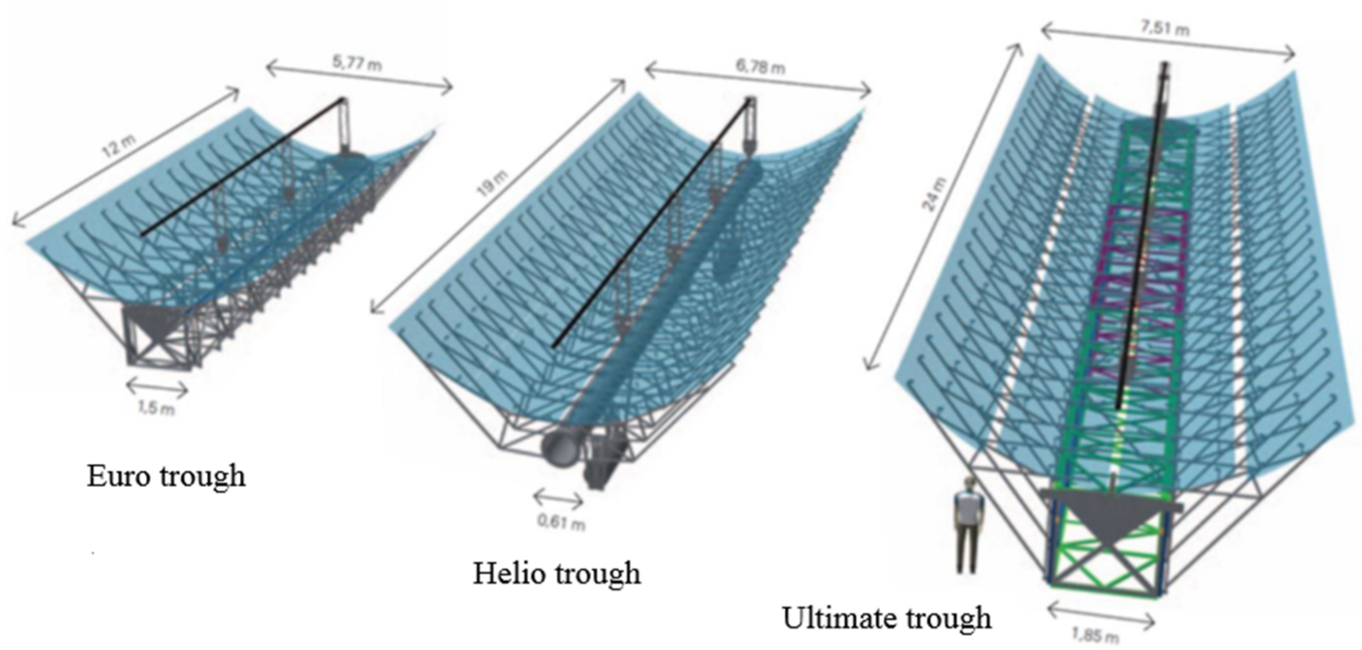

Fig. 11: Euro trough, Helio trough and Ultimate trough collectors [19]

Table. I

EURO TROUGH, HELIO TROUGH, AND ULTIMATE TROUGH PARAMETERS

Parameters	Euro trough	Helio trough	Ultimate trough
A_{am}	69.24 m^2	128.82 m^2	180.24 m^2
A_{ri}	2.487 m^2	3.938 m^2	4.974 m^2
A_{ro}	2.638 m^2	4.1762 m^2	5.257 m^2

And h_{out} is the heat coefficient between the annulus and the ambiant, it is defined by Eq. (20).

$$h_{out} = 4 * (V_{wind}^{0.58}) * (D_{co}^{-0.42}) \tag{20}$$

The parameters of simulation that are considered for these types of collector are shown in Table 1.

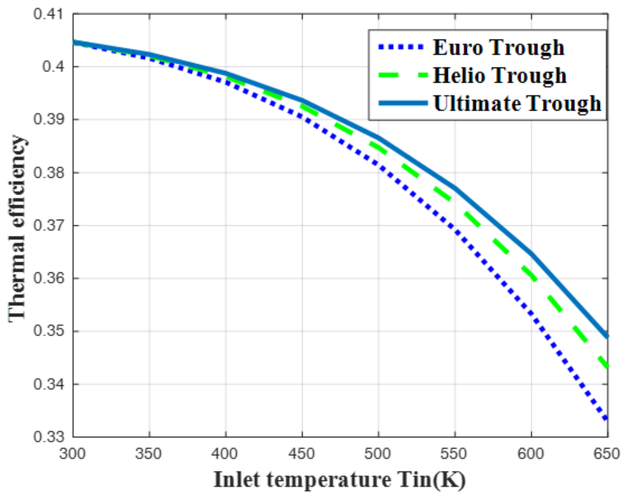

Fig. 12: Thermal efficiencies of Euro trough, Helio trough and Ultimate trough collectors

The results related to the thermal efficiency are shown in Fig. 12 highlighting the difference between the Euro trough, Helio trough and Ultimate trough. The most efficient collector is the Ultimate trough, the less efficient one being the Euro trough, and that depends on the Aperture area, the larger it is the better the efficiency is improved, the difference being more than 2% higher compared to the other ones. The larger aperture area induces the use of more construction materials, but it is to be noted that, on the other hand, the number of assembled collectors is lower. This leads to a reduction in motors, sensors, connection joints, foundations, controllers, pylons, etc. Which in turn reduces the costs of the power plant.

VI. CONCLUSIONS

In this paper, we have highlighted the effects of tube diameter, focal length and collector's width on the coefficient of deviation angle. The variation of tube diameter mainly affects mainly the coefficient of deviation angle. Therefore a compromise must be found between the parabolic through parameters to reach its right value and thus a high thermal efficiency value and appropriate related economic figures.

The width and the length of Euro trough, Helio trough, and Ultimate trough were examined. The observed best performance was that related to the Ultimate trough, which presents a 2% difference in efficiency, and allows reducing the number of units to be assembled in solar field, i.e. reducing the cost of the power plant.

REFERENCES

[1] A. Ahmad, O. Prakash, R. Kausher, G. Kumar, S. Pandey, S.M. Hasnain, "Parabolic trough solar collectors: A sustainable and efficient energy source", *Materials Science for Energy Technologies.*, Vol. 7, ISSN 2589-2991, pp. 99–106, 2024. DOI:

10.1016/j.mset.2023.08.002.

[2] E. C. Okonkwo, M. Abid, and T. A.H. Ratlamwala. "Numerical analysis of heat transfer enhancement in a parabolic trough collector based on geometry modifications and working fluid usage." *Journal of Solar Energy Engineering*, Vol. 140, no 5, 051009, 2018.

[3] L. G.. Fadodun, A. Kaood, M. A. Hassan, "Investigation of the entropy production rate of ferrosoferric oxide/water nanofluid in outward corrugated pipes using a two-phase mixture model", *International Journal of Thermal Sciences*, Vol. 178, 107598, ISSN 1290-0729, 2022 DOI: 10.1016/j.ijthermalsci.2022.107598.

[4] A. Kaood, G. F. Olatomide, "Numerical investigation of turbulent entropy production rate in conical tubes fitted with a twisted-tape insert", International Communications in Heat and Mass Transfer, Vol. 139, 106520, ISSN 0735-1933, 2022 DOI: 10.1016/j.icheatmasstransfer.2022.106520.

[5] A. Kaood, O. A. Ismail, A.H. Al-Tohamy, "Hydrothermal performance assessment of a parabolic trough with proposed conical solar receiver", *Renewable Energy*, Vol. 222, 119939, ISSN 0960-1481, 2024, DOI: 10.1016/j.renene.2024.119939.

[6] M. S. Djenane, S. Hadji, O. Touhami, A.H. Zitouni, "A Novel Design of Parabolic Trough Solar Collector's Absorber Tube". *Journal of Solar Energy Engineering*, Vol. 146, no 3, 031001, 2024, DOI: 10.1115/1.4063700.

[7] Y. Demagh, A. Hachicha, H. Benmoussa, Y. Kabar, "Numerical investigation of a novel sinusoidal tube receiver for parabolic trough technology", *Applied Energy*, Vol. 218, pp.494–510, 2018.

[8] O. Chakraborty, S. Roy, B. Das, R. Gupta,"Effects of helical absorber tube on the energy and exergy analysis of parabolic solar trough collector– A computational analysis", *Sustainable Energy Technologies and Assessments*, Vol. 44, 101083, 2021.

[9] B. Zou, Y. Jiang, Y. Yao, H. Yang, "Thermal performance improvement using unilateral spiral ribbed absorber tube for parabolic trough solar collector. *Solar Energy*, Vol. 183, pp.371–38, 2019.

[10] X. Gong, F. Wang, H. Wang, J. Tan, Q. Lai, H. Han,"Heat transfer enhancement analysis of tube receiver for parabolic trough solar collector with pin fin arrays inserting", *Solar Energy*, Vol.144, pp.185–202, 2017.

[11] H. Hoseinzadeh, A. Kasaeian, M. Shafii, M. B, "Geometric optimization of parabolic trough solar collector based on the local concentration ratio using the Monte Carlo method", *Energy Conversion and Management*, Vol.175, pp.278–287, 2018.

[12] Cheng, Z. D., He, Y. L., Du, B. C., Wang, K., Liang, Q. Geometric optimization on optical performance of parabolic trough solar collector systems using particle swarm optimization algorithm. *Applied energy*, 148, 282-293, 2015.

[13] Behram, Saqib, et al. "Design, fabrication and thermal analysis of parabolic trough collector." *MATEC Web of Conferences, EDP Sciences*, Vol. 398, 2024.

[14] Peng, Wei, and Omid Karimi Sadaghiani. "Geometrical variation in receiver tube of SEGS LS-2 parabolic trough collector (PTC) based on heat flux distribution to improve the thermal performance." *International Journal of Thermal Sciences* 163, 106858, (2021).

[15] H. Olia, M. Torabi, M. Bahiraei, M. Ahmadi, M. Goodarzi, M. Safaei, "Application of nanofluids in thermal performance enhancement of parabolic trough solar collector: state-of-the-art", *Applied Sciences*, 9(3), 463, 2019.

[16] T. Simonović, M. Stamenić, N. Tanasić, M. Trninić, "Effect of small deviation of incident angle on thermal performance of parabolic trough solar collector". In 2016 4th International Symposium on Environmental Friendly Energies and Applications (EFEA) (pp. 1-4). IEEE, 2016.

[17] M.S. Djenane, S. Hadji, O. Touhami, "Effect of Deviation Angle on the Parabolic Trough Solar Collector Performances," Proceedings of the 2019 International Conference on Advanced Electrical Engineering (ICAEE), Algiers, Algeria, Nov. 19–21, pp. 1–6, 2019.

[18] H.Z Hassan, "Transient Analysis of a Solar Chimney Power Plant Integrated with a Solid-Sorption Cooling System for Combined Power and Chilled Water Production" *Energies*, 15(18), 6793, 2022.

[19] C. Caliot, G. Flamant, " Technologie des concentrateurs cylindro-paraboliques", Laboratoire proceeds, Matériaux et energie solaire, Formation CSP, OUARZAZATE 25, 27 mai 2016.

Mohamed Salim Djenane is currently Electrical substation engineer at SONELGAZ, He earned his PhD in Electrical Engineering from Ecole Nationale Polytechnique, Algiers in June 2024.

Seddik Hadji is Professor in Electrical Engineering at Ecole Supérieure des Sciences Appliquées, Algiers. His field of expertise is in Power Electronics, Actives Filters and Renewable Energies Solar.

Omar Touhami is a Professor in Electrical Engineering at Ecole Nationale Polytechnique, Algiers. He received the Engineering, M.S., and Ph.D. degrees in electrical engineering from the Ecole Nationale Polytechnique d'Alger, Algiers, Algeria, in 1981, 1986, and 1994, respectively. From 1989 to 1994, he was an Associate Researcher with the Research Center on Automatic of Nancy (CRAN-ENSEM-INPL), where his works on the identification of electric machines were a success in the industries. He has been a Scientific Adviser to the Ministry of Higher Education in Algeria and an Expert Member of the CNEPRU commission since 1997 until 2011. His domains of research are electrical machines, power systems and variable speed drives, and diagnosis of dynamical systems.

Analysis of Multiphase Electrical Systems According to the Number of Phases

Abdelhakim Khelafi, Abdelmalek Djebli, Omar Touhami, and Rachid Ibtiouen

Abstract−This paper studies multiphase electrical systems based on the properties of their number of phases. Depending on its parity, the latter can be even or odd. Its factorization provides numerous ways to represent the phase number. Thus, this paper presents the possibilities of modifications together with the properties that arise from the factorizations of the number of phases. Furthermore, we present the formulation of symmetrical components for both even and odd numbers of phases.

***Keywords*−Multiphase systems, multi-star systems, connections of Multiphase systems, symmetrical components, instantaneous symmetrical components.**

I. INTRODUCTION

The continuous increase in the demand,driven by significant industrial development, accounts for approximately 40% of global consumption [1]. Additionally, urban growth and the expansion of cities contribute to this trend by creating more complex and extensive infrastructure. This leads to a higher demand for electricity, which is essential for public sectors such as transportation and utilities, as well as for the growing needs of households. This makes an increase in electricity production inevitable. Therefore, upgrading and improving the efficiency of conventional methods of electricity generation and transmission has become an important requirement. Also searching for new sources of energy and better use of renewable energies. In addition, the consumption of electrical energy must be rationalized in the sectors that consume the most electricity which are mainly industrial and transport sectors, through the use of high efficiency systems. High-power electrical and electromagnetic systems are increasingly in demand in areas such as marine propulsion and electric traction. This demand is driven by the suitability of these systems, since electromagnetic systems are characterized by high reliability. Therefore, multiphase electrical systems MES have attracted significant interest from researchers due to their numerous advantages such as higher power density, higher fault tolerance [2].These advantages have led to an increased use of MES in the electric traction systems, marine propulsion, more electric aircraft, electrical vehicles and industry[3-8]. Multiphase electric power generators have obvious advantages over conventional three-phase generators, including the ability to achieve higher power at lower voltages [9], which reduces the level of winding insulation. In the literature, multiphase generators are not discussed for their use in conventional power plants (gas power plant, and combined cycle). However, they have been proposed as alternatives to their three-phase counterparts in renewable energy conversion systems [7]. Where the most important objective is to maintain a stable and continuous output power which will be transferred to the electrical networks. The number of phases (greater than 3) of multiphase generators offers to generator higherfaults tolerance and a higher degree of freedom, which allow the development of new controls in the faulty case. This makes multiphase generators suitable for wind power systems, especially variable speed ones, and suitable for marine power systems [10-13], [9]. Multiphase generators have also proven themselves in the field of aeronautics, electric vehicles and ships [14-15]. In aeronautics, the current trend is to replace hydraulic and mechanical systems in aircraft with other electrical and electromagnetic ones [16]. And it is an application of the concept known as the more electric aircraft [17]. The market for electric cars has also experienced enormous development, especially since the beginning of the second decade of the 21st century, due to the success recorded in the field of batteries. However, research is still ongoing to develop more reliable driving systems, and to increase the storage capacity of the batteries. The majority of studies on MES have aimed to deal with system performances, design, and control development. Most of them concluded that multiphase systems are appropriate for the applications requiring higher reliability, higher power density and fault tolerance. However, in the literature few works address the additional properties offered by an appropriate choice of number of phases. Hence, this work presents an analytical study of the advantages offered by the characteristics of the number of phases, which is a positive integer.

Manuscript received July 4, 2023; revised August 7, 2024.

A. Khelafi, A. Djebli, O. Touhami, and R. Ibtiouen are with Electical Department, Ecole Nationale Polytechnique, Algiers, ALGERIA. (e-mail: abdelhakim.khelafi@g.enp.edu.dz, abdelmalek.djebli@g.enp.edu.dz, omar.touhami@g.enp.edu.dz, rachid.ibtiouen@g.enp.edu.dz)

Digital Object Identifier (DOI): 10.53907/enpesj.v4i2.217

II. PROPERTIES OF THE NUMBER OF PHASES AND THE MODIFIABILITY OF THE MULTIPHASE SYSTEM

The concept of multiphase systems became important, after the advent of multiphase electric machines in the late 19th century [18], in which the electromagnetic quantities are rigidly linked to the multiphase windings of these machines. Since then, the three-phase systems are adopted for the production, transmission of electricity, transportation and industry applications. A symmetric multiphase system by definition is a set of *m* sinusoidal quantities of the same frequency and the same amplitude, where the phase difference between the adjacent phases is $2\pi/m$ [19]. The set of *m* quantities defined as MES, can be *m* currents, *m* voltages, or *m* magnetic fluxes. The name of a multiphase system is associated with its number of phases, in the English nomenclature, a multiphase system of m phases is called "m-phase", often m is in letter. In contrast, in French nomenclature, the name of a multiphase system with m phases consists of a Greek prefix followed by the word "phasé", the Greek prefix corresponds to Greek numbers. Examples of multiphase system nomenclatures are given in Table. I. There is however an exception in French nomenclature, when m=2, in this case the system is called “biphasé” [20].

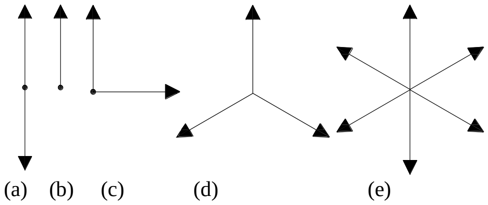

Fig.1 Representation of MES using phasor diagrams (a) two phase system (b) One-phase system (c) two-phase system the angle between the two phases is $\pi/2$ (d) three-phase system (e) six-phase system.

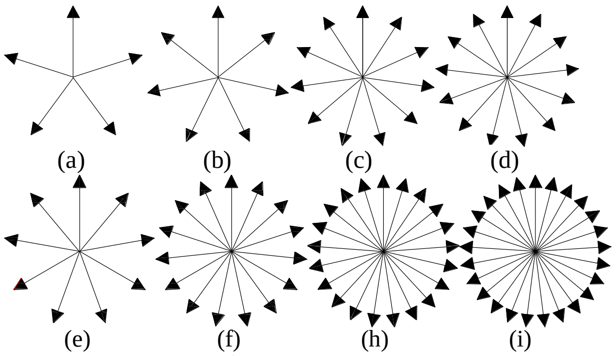

Fig.2 Phasor diagrams of multiphase systems with prime and odd phase numbers (a) Five-phase (prime) (b) Seven-phase (prime)(c) Eleven-phase (prime) (d) Thirteen-phase (prime) (e) Nine-phase (f) 15-phase (h) 21-phase (i) 25-phase.

The geometric representation of MES, known as phasor diagrams Fig.1, is the most suitable in the steady state [21]. Phasor diagram is a geometric tool allowing calculations such as addition, as well asdifferentiation and integration of sinusoidal functions of the same frequency. This makes them invaluable for analyzing MES, where they visually represent phase relationships and magnitudes of voltages or currents. Theoretically, the number of phases can be any integer number. Nevertheless, in the literature, there are few references dealing with the properties of multiphase electrical systems MES according to the number of phases m, including the most interesting [21-25]. Thus, based on [21-23] the MESs can be classified according to the nature of their number of phases m. This classification distinguishes MESs with even m, odd m, and prime number m of phases, each representing distinct configurations that contribute to understanding the varied characteristics and behaviors of MESs. If the phase number m of a multiphase system equals two ($m=2$), then m is both even and prime. By applying the previously mentioned definition, the phase angle between the two phases is π Fig.1 (a), this system is said to be two-phase [21]. It can be seen that the representation Fig.1 (a) of this system consists of two vectors, each vector represent one phase as shown in Fig.1 (b), these vectors having the same axe, whereas their directions are opposite.Thus, in the case where this system represents machine, its winding consists of two coils with an angle of π between their axes.The field lines are parallel, and hence, no rotating magnetic field is produced [21]. The system shown in Fig1(c) is also a two-phase system, nevertheless these two phases are in quadrature, the phases are shifted by π/2, in English nomenclature such a system is called Two-phase system. It should also be noted that the two-phase system is a particular case of the four-phase system [20]. Two-phase systems are still used, for example Scott's transformer in high-speed train. Currently, two-phase machines are not used, however the principle of two-phase machines is used in single-phase machines, where an auxiliary winding shifted by π/2 is introduced. This winding is usually connected to a capacitor called a start capacitor, which generates the voltage phase shift necessary to create rotating field, thereby producing the electromagnetic torque. The MESs with an even number of phases can be seen as being composed of m/2 two-phase systems (as shown in Fig.1 (a)) displaced by π/m, such as the six-phase system in Fig.1 (e) which is formed by three two-phase systems. In practice, this system can be realized with a three-phase transformer, where each secondary phase coil has midpoint. According to the above, MESs can be classified according to the nature of the number of phases into three categories: MES with an even number of phases, MES with an odd number of phases and MES with a prime number of phases.

A. Multiphase System with Odd Number of Phases

The theory of arithmetic states that every odd number m can be uniquely factored into a product of prime factors different from two. Moreover, a prime number cannot be factorized. Figure (2) shows phasor diagrams of MESs with number of phases odd, and prime, the systems in Fig.2 (a) (b) (c) (d) are with prime number of phases which are 5, 7, 11 and 13 respectively, the systems in Fig.2 (e) (f) (h) (h) are with non-prime odd number of phases which are 9, 15, 21 and 25 respectively .
Thus, m is written as (1).

$$m=s_1\times s_2\times\ldots\times s_k \tag{1}$$

Where s_1, s_2, s_k are non-two prime numbers, and k is an integer number.
According to (1), there are several manners to express m and therefore, several ways of seeing the MES. The most appropriate m expression is the product of two numbers, because this allow to analyze the system properly. Thus, by rewriting (1) assuming $m_{ph} = s_1$, and $s = s_2 \times ... \times s_k$, the equation (2) is obtained.

$$m= s \times m_{ph} \tag{2}$$

According to the expression (2) the MES of m phases can be considered formed by s multiphase systems of m_{ph} phases, where the angle shift is 2π/ m. it is possible to assume $s=s_1$ and$m_{ph}= s2\times\ldots\times s_k$. For example, a 15-phase MES, where $m=15$ is the product of three and five (m=3×5). Thus, the 15-phase MES illustrated in Fig.2 (f)can be seen as formed either by three five-phase systems shifted by 2π/15 or by five three-phase systems shifted by 2π/15. Also the nine-phase MES in Fig.2 (e) can be seen formed by three three-phase systems shifted by 2π/9.Hence, a MES with non-prime odd number of phases m, as expressed by (2) is modifiable. This modification depends on how the MES is viewed. If the MES is viewedas being formed by sMESs of m_{ph} phases. Thus, by rotating the (s-

Table. I
NOMENCLATURE OF MULTIPHASESYSTEMS.

Phase number m	Greek Prefix	French nomenclature	English nomenclature
1	mono	monophasé	one-phase
2	-	-	-
3	tri	triphasé	three-phase
4	tétra	tétraphasé	four-phase
5	penta	pentaphasé	five-phase
6	hexa	hexaphasé	six-phase
7	hepta	heptaphasé	seven-phase
8	octa	octaphasé	eight-phase
9	nona	nonaphasé	9-phase
10	déca	décaphasé	10-phase
11	undéca	undécaphasé	11-phase

1) systems of m_{ph} phases by π, this results in a multi-star system formed by *s* m_{ph}-phasesystems. Otherwise, if the MES is seen formed by m_{ph}*s*-phase systems, by rotating the (m_{ph}-1) the *s*-phase systems by π, this results in a multi-star system formed by m_{ph}*s*-phase systems. However, the total number of phases is still*m*, the number of phases of the original system.

It has been previously mentioned that a 15-phase system canbe seen as formed either by three five-phase MESs shifted by 2π/15 or by five three-phase MESs shifted by 2π/15, as depicted in Fig. 3 (a) (b), respectively. Therefore, by rotating two five-phase MESs in Fig.3 (a) by π, which corresponds to the inversion of the corresponding winding terminals, a triple-star five-phase MES is obtained as shown in Fig.3 (c). The 15-phase MESFig. 3 (b) can be transformed into MES of five star three-phase system as shown in Fig.3 (d), this by rotating four three-phase systems of Fig.3 (b) by π.

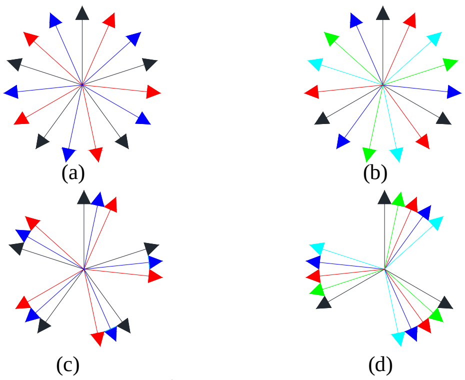

Fig.3 Modification possibility of MES with odd non-prime number of phases (a) 15-phase system formed by three five-phase systems (b) 15-phase system formed by five three-phase systems (c) Triple -star five-phase system (d) Five-star three-phase system.

B. Multiphase System with Even Number of Phases

In this case, the number of MES phases *m* can be expressed by (3), four-phase, six-phase eight-phase and twelve-phase MESs are shown in Fig. 4 (a) (b) (c) (d), respectively. Where m_{ph} in (3) is an integer. The even number *m* of phases can be halved [21], [22] and becomes m_{ph} phases. Such a system can be considered formed by two m_{ph}-phase MSEs shifted by π. Depending on the nature of m_{ph}, there are two cases: the first is when m_{ph} is odd, and the second is when m_{ph} is even. The usefulness of this writing will be seen later. Practically, reduction of the number phases is performed by reconnecting the terminals of the windings [22], [23]. In the case of transformers and machines, for example a three-phase transformer where the secondary is with midpoints, this secondary is a six-phase system shown in Fig.4 (b). Therefore, applying the concept of the number of phase reduction, the six-phase system of transformer secondary Fig.4 (b) can be reduced to three-phase Fig.1 (d) by reversing the terminals and connecting them in series.

$$m=2.m_{ph} \quad (3)$$

C. Reduced Multiphase System

The concept of phase number reduction came from multiphase electrical machines [21-23], it is the winding of the machine that enables the reduction of the number of phases, without rewinding.This is achieved through the modification of the connections of coil groups [21]. In practice, the windings of conventional three-phase electrical machines are originally six-phase windings [21-22] that have been reduced to three-phase.This reduction in the number of phases achieved by appropriately reconnecting the groups of coils. Additionally, this modification increases the winding factor from 0.85 to 0.96. Furthermore, reducing the number of phases from 6 to 3, maintains the same spatial harmonics content as the original 6-phase winding. It should be noted that this phase number modification is only possible for certain windings with an even initial phase number m and a phase shift of 2π/m [24].

Since the even number of phases *m* is expressed by (3), two cases can be distinguished based on the nature of the number m_{ph}: the first where m_{ph} is even and the second m_{ph} is odd. Moreover, when m_{ph} is an odd prime number, this represents a

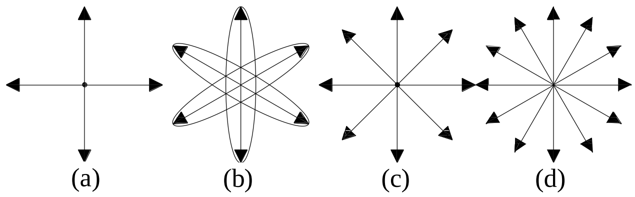

Fig.4 Phasor diagrams of multiphase systems with even number of phases (a) four-phase (b) six-phase (c) eight-phase (d) twelve-phase.

special case.

D. Reduced Multiphase System with m_{ph} Odd Number

In this case, the m-phase MES is formed by two m_{ph}-phase MESs shifted by π. Geometrically, the phase number reduction consists of rotating one of the two m_{ph}-phase systems by π. In practice, the reduction consists of inverting one of the two m_{ph}-phase windings, and putting them either in series or in parallel. Thus, the phase number m of MES is halved and becomes m_{ph}, and the angle shift between two adjacent phases becomes $2\pi/m_{ph}$.

Therefore, an electrical machine winding with a reduced number of phases at m_{ph} has the identical harmonic content and winding factor as the winding of $2 \times m_{ph}$ phases. For example a three-phase winding is actually 6-phase reduced, a five-phase is a reduced 10-phase winding and a seven-phase winding is a 14-phase winding reduced.

E. Reduced Multiphase System with m_{ph}Even Number

In this case, the number of phases m is even represented by (3), in addition m_{ph} in (3) is also even expressed by (4). Therefore, all the vectors representing the phases are located in the same semicircle [24]. Moreover, if the number m'_{ph} in (4) is odd, the adjacent phases are shifted by $(\pi/2)/m'_{ph}$. The reduction is achieved by inverting the vectors in the third and fourth quadrants of the original MES phasor diagram [24]. Consequently, the reduced MES is formed by m'_{ph} two-phase systems [24]. The Figure 5 (a) shows the reduced 12-phase SEP (12=2× 2×3), m'_{ph} =3, the reduced MES is formed by three two-phase MES shifted by π/6 Fig.5 (a).
In the general case when the number m_{ph} is an even multiple of an odd number, there exists an odd number m'_{ph} such that m_{ph} can be expressed as (5), where *k* in equation (5) is an integer with $k \geq 1$. Consequently, the reduced MES consists of $2^{k-1} \times m'_{ph}$ two-phase systems, shifted by $\pi/(2^k m'_{ph})$.

In a particular case where the number of phases *m* is expressed by (6) with $k \geqslant 2$, the reduced MES is formed by *(k-2)* two-phase systems, phase shifted by $\pi/2^{k-1}$.For example, reducing a 4-phase system yields a two-phase system as shown in Fig.5(b), reducing an 8-phase system yields two two-phase systems shown in Fig.5(c), and reducing a 16-phase system yields four two-phase systems illustrated in Fig.5(d).

$$m_{ph}=2.m'_{ph} \quad \text{where } m'_{ph} \text{ is odd number} \quad (4)$$

$$m_{ph}=2^k.m'_{ph} \quad (5)$$

$$m=2^k \quad (6)$$

Where$m'_{ph}$is an odd number

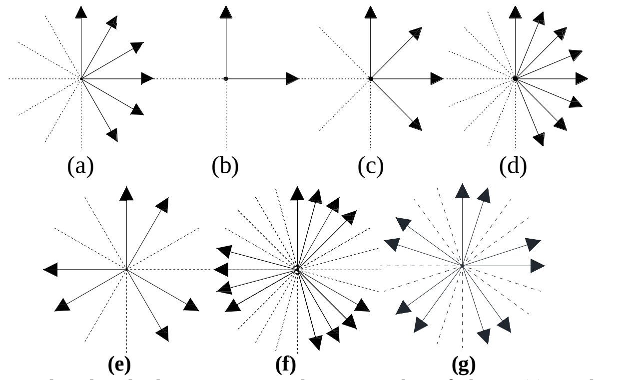

Fig.5 Reduced multiphase systems with even number of phases (a) 12-phase reduced to three two-phase(b) 4-phase reduced to 2-phase system (c) 8-phase reduced to two 2-phase (d) 16 –phase reduced to four two-phase (e) 12-phase reduced to double star three-phase (f) 24-phase reduced tofour three-phase system (g) 20-phase system reduced to double star five-phase system.

F. Multi-Star Multiphase System

If m_{ph} is expressed by (4), where m'_{ph} is odd, an additional phase reduction is possible beyond the previously mentioned phase number reduction. In this case, the MES is considered to consist of twom_{ph}-phase systems shifted by π/m_{ph}.Hence, the reduction of each m_{ph}-phase system results in a reduced system consisting of two m'_{ph}-phase systems shifted by $\pi/(2 m'_{ph})$.This configuration is known as a double star system. Therefore, m-phase MES with m is an even number of phases, as presented in (3), when the number m_{ph} in (3) is expressed by (4).In this case, the m-phase systemcan be reduced and transformed into a double star system consisted of two m'_{ph}-phase systems shifted by $\pi/(2 m'_{ph})$.In general case whenm_{ph} is written as (5), the m-phase system can be reduced and transformed into a multi-star system formed by $2^k m'_{ph}$-phase systems shifted by $\pi/(2^k m'_{ph})$.

The Figure 4 (d) shows a 12-phase MES (12=2×2×3), m'_{ph}=3, hence, it is possible to obtain a double star MES formed by two stars of three-phase shifted by $\pi/6$ Fig.5 (e). This system called asymmetric three-phase system, and its application in asynchronous machines is widely discussed in the literature. Therefore, the number of phases in such machine is actually a 12 phases, the corresponding winding is reduced by reconnecting the coil groups. This winding is generally used in motors supplied by two three-phase inverters their three-phase voltages are shifted by $\pi/6$. The reduction in the number of phases from 12 to two shifted three-phase, allows the use of conventional three-phase inverters. In addition, this winding has the same performance (high winding factor and reduced harmonic content) as a 12-phase winding. A 24-phase system can be reduced and transformed into four star three-phase system as shown in Fig.5 (f). Similarly,a 20-phase system can be reduced and transformed into double star system formed by two five-phase systems Fig.5 (g).

G. Reduction of Multi-Star Systems

A multi-star system, where the star represents a symmetric multiphase system of odd number of phases m'_{ph}. In multi-star systems, the vectors in the phasor diagram are divided into groups. Thus, by representing each group of vectors by their resultant vector, a MES of m'_{ph} phases is obtained. Consequently, the number of phases in the multi-star system can be reduced to match the phase number of a single star.

Furthermore, m-phase system$m$with number is an odd non-prime, its number of phases can be reduced. This by transforming the m-phase system into multi-star system, and represent each group of victors by their resultant as mentioned previously. The case of nine-phase transformed into three-phase triple star and reduced to three-phase is presented in Fig.6.Similarly, a 15-phase system can be transformed into a five-phase three-star system and reduced to five-phase system, as illustrated in Fig. 6.

H. Particularity of Multiphase System with a Prime Number of Phases

Multiphase systems with number of phases $m$that prime numbers are not modifiable and cannot be reduced. For example, a six-phase transformer secondary shown by the phasor diagram Fig.4 (b) and a three-phase double-star machine represented by the phasor diagram Fig. 5 (e), these systems can be reduced by reconnecting the winding terminals [22] and become three-phase systems. However, the three-phase secondary of a transformer or a three-phase machine cannot be modified or reduced [21].

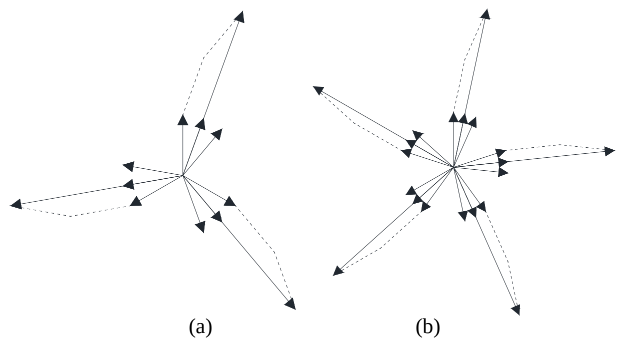

Fig.6 Reduction of multi-star systems (a) Reduction triple- star three-phase to three-phase (b) Reduction triple- star five-phase to

Therefore, an m-phase system (with m prime number) represents a basis for n-phase systems (n multiple of m) and for multi-star of m-phase systems. Thus, the study of m-phase system facilitates the study of n-phase systems (n multiple of m) and for multi-star m-phase systems, where the number of phases is high.

In addition, multiphase systems (m prime number) are advantageous in terms of harmonic content.

III. MULTIPHASE SYSTEM CONNECTIONS

Phase connections are primarily for multiphase systems with multiphase windings, multiphase such as machines and multiphase transformers. The windings of the phases in a m-phase machine or transformer have 2×m terminals. Consequently, several connections of the windings of the m phases are possible. Each connection is characterized by the voltage resulting across a phase winding terminals. Depending on the parity of the phase number, two cases are distinguished: the first when$m$ is odd and the second when$m$ is even. Nevertheless, the star and polygon couplings independent of the parity of the number of phases are obvious connections.

In a star connection, thecharacteristic voltage is the phase voltage V_{ph} of the multiphase system. In contrast, a polygon connection is characterized by the voltage between two adjacent phases. The equation (7) expresses the voltage between adjacent phases U_{ad} as a function of the number of phases$m$ and the phase voltage V_{ph}.

If the number of phases m is odd, the number of possible connections is $(m+1)/2$. By subtracting the two obvious connections star and polygon, the result is (m-3)/2 connections between non-adjacent phase windings.

The five-phase and seven-phase systems, which have prime numbers of phases, are illustrated in Fig. 7 and Fig. 8, respectively. Each connection, except for the star connections, is depicted as a single regular polygon, as shown in Fig. 7 (b) (c), Fig. 8 (b) (c) (d). The connection in Fig.7 (c) is called pentacle connection which is a regular pentagram characterized by the voltage between non-adjacent phases. The connections in Fig. 8 (c) and (d) are both regular heptagrams. Therefore, in the case of an *m*-phase winding where *m* is a prime number, the possible connections are star and polygon connections, in addition to ((m+1)/2)-2 regular polygram connections.

The connections of a nine-phase system, shown in Fig. 9, include star Fig. 9 (a), nonagon Fig. 9 (b), and two regular Fig. 9 (c) Fig. 9 (d). In this case, the number of phases is a non-prime odd number and can be expressed as (2). Hence, a particular connection is formed by three triangles shifted by 2π/9, as shown in Fig. 9 (e).

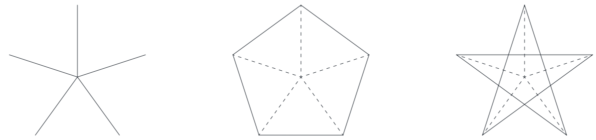

(a) (b) (c)

Fig.7 Connections of five-phase system (a) star connection (b) Pentagon connection (c) Pentacle connection

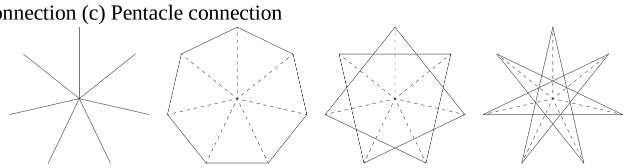

(a) (b) (c) (d)

Fig.8 Connections of seven-phase system (a) star connection (b) Heptagon connection (c) and (d) Tow regular Pentagram connections

In m-phase windings with an odd non-prime number of phases, as expressed by equation (2) where m_{ph} and *s* are prime numbers, the connections include two particular connections. Each connections consists of distinct polygons: the first consisting of *s*polygonswith m_{ph} sides,shifted from each other by 2π/m, and the second consisting of m_{ph} polygons with *s* sides, shifted from each other by 2π/m. The connections are more complicated when m_{ph} and/or *s* are odd non-prime numbers.

Regarding the connections of systems with an even number of phases, the systems in question are those with four or more phases. This is because systems with two phases have only one possible connection. In four-phase systems, there are two connections: the star connection and the square connection. In systems m-phase with *m*>4, the connections include: star and polygon configuration, polygram connections, and arrangements consisting of multiple shifted polygons.

Table. II

RATIO OF PHASE-TO-PHASE VOLTAGES OF ADJACENT AND NON-ADJACENT PHASES TO PHASE VOLTAGE

Ratio U_k/V_{ph}	Nombre de phases m							
	m=5	m=6	m=7	m=8	m=9	m=10	m=11	m=12
Adjacent Phases	1.17	1	0.87	0.76	0.68	0.61	0.56	0.52
Non adjacent Phases	1.9	1.73	1.56	1.41	1.28	1.17	1.08	1
	-		1.95	1.85	1.73	1.61	1.51	1.41
	-	-	-	-	1.97	1.9	1.82	1.73
	-	-	-	-	-	-	1.98	1.93

When the number of phases *m* is even, the number of possible connections is m/2. Therefore, the number of non-adjacent voltages is (m/2-2), the possible connections of 8-phase and 10-phase systems are shown in Fig.10 and Fig.11 respectively.

Since each connection is characterized by a voltage, the number of possible voltages corresponds to the total number of connections. These voltages include phase voltage, voltage between adjacent phases, and the voltages between non-adjacent phases. U_{ad}

The generalized formula giving the voltages between adjacent and non-adjacent phasesU_k is expressed by (8), the voltages between non-adjacent phases are obtained from (8) when *k>1*.

The Table. II gives the U_k/V_{ph} ratio in different cases where

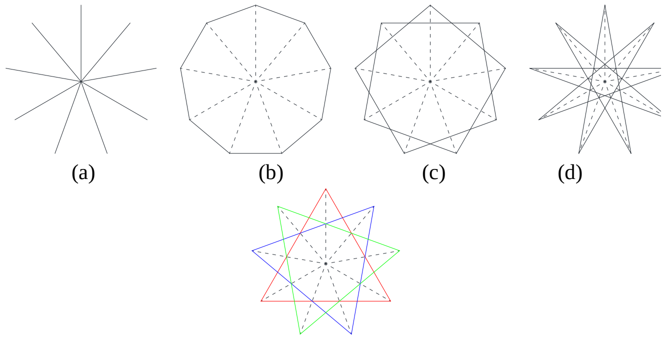

(a) (b) (c) (d)

(e)

Fig.9 Connections of nine-phase (a) star connection (b) Nonagon connection (c) and (d) Tow regular nonagram connections (e) connection formed by three separated trianglesshifted by 2π/9.

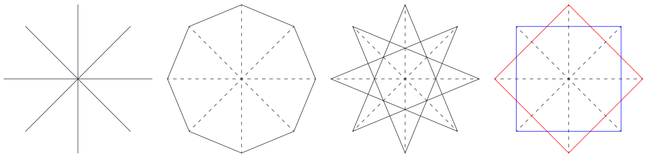

(a) (b) (c) (d)

Fig.10 Connections of eight-phase system(a) star connection (b) Octagon connection (c) regular octagram connection(d) Connection is formed two square shifted by π/2.

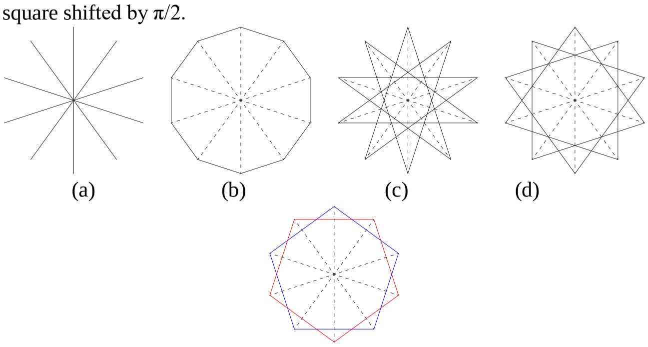

(a) (b) (c) (d)

(e)

Fig.11 Connections of 10-phase system (a) star connection (b) decagon connection (c) (d) Two regular decagram connections (e)connection formed by two separated pentagons shifted by 2π/10.

$1\leq k\leq m$,is evident that as the number of phases increases, the voltage U_{ad} between adjacent phases given by (7) decreases, resulting in a reduced ratio U_{ad}/V_{ph}. For instance, in a five-phase system, the ratio is 1.17, whereas it drops to 0.87 in a seven-phase system and further decreases to 0.52 in a twelve-phase system. In contrast, the voltages between non-adjacent phases U_k (*k>1*) increase with the number of phases.For example, in the five-phase system, the ratio is 1.9, compared to 1.93 in the 12-phase system.

$$U_{ad} = 2.V_{ph}.\sin\left(\frac{\pi}{m}\right) \tag{7}$$

$$U_k = 2.V_{ph}.\sin\left(\frac{k\pi}{m}\right),\begin{cases} m: odd..k = 1,...,(m-1)/2 \\ m: even..k = 1,...,m/2-1 \end{cases}, \tag{8}$$

IV. METHOD OF SYMMETRICAL COMPONENTS

The method of Symmetrical Components SC is considered the most suitable method for the analysis of multiphase systems, was presented for the first time by C. L. FORTESCUE 28 Jun 1918 at the 34th annual convention of the American Institute of the Electrical Engineers in Atlantic City (NJ, USA), where he introduced his paper [19]. The method of symmetric components had its origin in the mathematical analysis of induction machines operating under unbalanced conditions

[22]. The purpose of this method as indicated by C. L. FORTESCUE in [19] is to study multiphase systems (multiphase machine, multiphase network, etc.) under unbalanced conditions. In his article [19], C. L. FORTESCUE refers to this method by several names: symmetrical co-ordinates, sequence components. Currently, this method is known as "the method of Symmetric Components".

In 1913, Fortescue conducted a mathematical study of the behavior of asynchronous motors under unbalanced conditions. What caught the author's attention the most in the results obtained was their symmetry [19]. The solution always

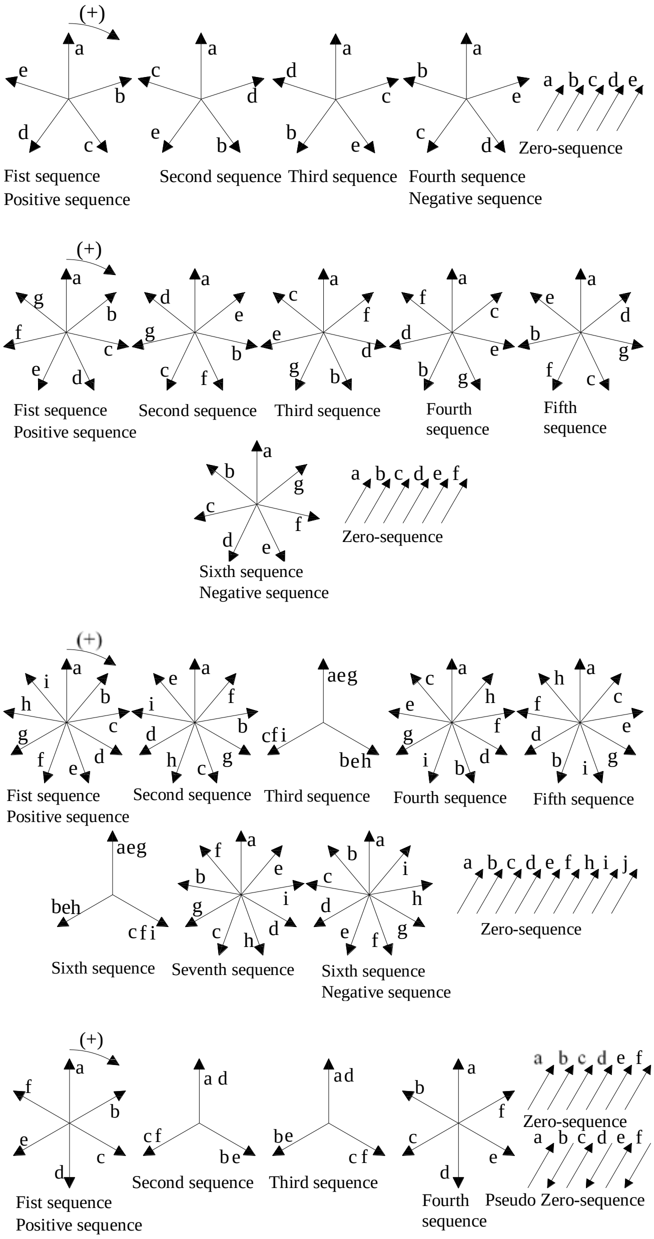

Fig.12 Symmetrical components of five-phase, six-phase, seven-phase and nine-phase systems.

reduced to the sum of two or more symmetric solutions [19]. This then leads the author to ask whether there are general principles by which the solution of unbalanced multiphase systems can be reduced to the solution of two or more balanced multiphase systems [26-27].

The great advances in the application of fundamental laws to electrical circuits are due to the development of mathematical tools. It is the same for the SC, since the original formulation of the SC presented in [19] was written in the form of an equation system containing many equations representing the phases of a MES. This method has been rooted mathematically, reformulating it in matrix form. What makes SC an object of algebra [27], where algebraic concepts such as the concept of passage from one space to another using passage matrices; the passage matrix is known in the literature by transformation matrix. Additionally, the algebraic formulation made SC easy to understand and use. This has made it the main method for calculating MESs, in particular three-phase systems which are the most used in machinery and transmission and distribution networks. Furthermore, the algebraic formulation allowed to derive the ubiquitous Clarke and Park transformations from the Fortescue symmetric component transformation [27].

Since the publication of [19] at the beginning of the 20th century, numerous research articles have explored the applications of SC in the study and modeling of both synchronous and asynchronous three-phase machines, as well as three-phase networks [27-30]. Furthermore, multiphase systems with a number of phases m are discussed [21-24], in which two cases are distinguished: the first when*m* is odd and the second when*m* is even.

The transformation of the *m* quantities of *m*-phases MES,where *m* is an odd number, into symmetrical components SC is expressed by (9). The transformation of the quantities of an *m*- phase, where *m* is an odd number, into symmetric components SC, is expressed by (10). The transformation matrices in the case where*m* odd and *m* is even are represented byC_s and C_{s2}, as shown in equations (11) and (12), respectively. The quantities X_k ($k=1.2\ldots m$) in (9) and (10) are the phase quantities which can be currents, voltages…

$$\begin{bmatrix} X_{cs0} \\ X_{cs1} \\ X_{cs2} \\ X_{cs3} \\ \vdots \\ X_{cs(m-1)} \end{bmatrix} = \frac{1}{m} \begin{bmatrix} 1 & 1 & 1 & 1 & \cdots & 1 \\ 1 & a & a^2 & a^3 & \cdots & a^{(m-1)} \\ 1 & a^2 & a^4 & a^6 & \cdots & a^{2(m-1)} \\ 1 & a^3 & a^6 & a^9 & \cdots & a^{3(m-1)} \\ \vdots & \vdots & \vdots & \vdots & \cdots & \vdots \\ a & a^{(m-1)} & a^{2(m-1)} & a^{3(m-1)} & \cdots & a^{(m-1)(m-1)} \end{bmatrix} \begin{bmatrix} X_1 \\ X_2 \\ X_3 \\ X_4 \\ \vdots \\ X_m \end{bmatrix} \quad (9)$$

etc.

Where $a=e^{j2\pi/m}$, and the phase quantities are expressed by vector X, while the symmetrical components are expressed by the vector X_{cs}.

When*m*is odd, the quantities X_{cs0} and X_{csk} ($k=1, 2\ldots (m-1)$) are the symmetrical components of the m-phase system. The componentX_{cs0} is called the zero sequence component. The components X_{cs1} and $X_{cs(m-1)}$ are the positive sequence components and the negative sequence component respectively.

In the case of an even number of phases, the symmetric components of the system are X_{cs00}, X_{cs0} and X_{csk} ($k=1, 2\ldots (m-2)$). The components X_{cs0}, X_{cs1} and $X_{cs(m-1)}$ are the zero sequence, positive and negative sequences. The component$X_{cs00}$is referred to as the pseudo-zero component. This pseudo-zero component does not exist in systems with an odd number of phases [29]. On the other hand, systems with an even number of phases contain the pseudo-zero component [27].

Each symmetrical component, with the exception of the zero-sequence and pseudo-zero sequence components, represents a symmetrical multiphase system of different phase succession [19], [30]. In the case of five-phase system, the succession of phases**abcde** corresponding to the positive sequence component while the succession of phases**edcba**is corresponding to the negative sequence component. The phase succession **acebd** is corresponding to the second sequence component, and the succession**adbec** is corresponding to third sequence component, this succession of phases is the inverse of that corresponding to the second sequence component.

The symmetrical components of five-phase system, where the number of phases is prime,represent four symmetrical five-phase systems and one zero-sequence as shown in Fig. 12 (a). Likewise, thesymmetric components of a seven-phase system, with prime number of phases,represent six symmetrical seven-phase systems and one zero-sequence component, as shown in Fig. 12 (b).In the case of the nine-phase system, where the number of phases is an odd non-prime number, the symmetrical components represent one zero-sequence component, five nine-phase symmetrical systems, and two particular components each representing three-phase system, as shown in Fig.12 (c).The figure 12 (d)illustrates the representation of the six components of a six-phase system, including two six-phase systems, two three-phase systems, one zero-sequence component and one pseudo-zero-sequence component.

Hence, it is possible to generalize that in the case of an m-phase system with a prime number of phases, the m symmetrical components represent (m-1) m-phase symmetrical systems and one zero-sequence system. In the case of an odd non-prime number of phases, the symmetrical components represent one zero-sequence component, at least two m-phase symmetrical systems, and several symmetrical systems with a phase number smaller than m. In the case of an even number of phases, the symmetrical components represent two m-phase systems, zero-sequence and pseudo-zero components, and (m-4) systems with a smaller number of phases than m.

The matrices C_s and C_{s2}defined in equations (11) and (12) respectively,are the transformation matrices. The matrixC_s is transformation matrix when m is odd, and C_{s2} is the transformation matrix when m case is even.Both matrices C_s and C_{s2} are $m\times m$ square matrices. Algebraically, these matrices are called change-of- basis matrices, these matrices allow to express the quantities of phases by symmetrical components.

$$\begin{bmatrix} X_{cs0} \\ X_{cs00} \\ X_{cs1} \\ X_{cs2} \\ \vdots \\ X_{cs(m-2)} \end{bmatrix} = \frac{1}{m}\begin{bmatrix} 1 & 1 & 1 & 1 & \cdots & 1 \\ 1 & -1 & 1 & -1 & \cdots & -1 \\ 1 & a^2 & a^4 & a^6 & \cdots & a^{2(m-1)} \\ 1 & a^3 & a^6 & a^9 & \cdots & a^{3(m-1)} \\ \vdots & \vdots & \vdots & \vdots & \cdots & \vdots \\ a & a^{(m-1)} & a^{2(m-1)} & a^{3(m-1)} & \cdots & a^{(m-1)(m-1)} \end{bmatrix}\begin{bmatrix} X_1 \\ X_2 \\ X_3 \\ X_4 \\ \vdots \\ X_m \end{bmatrix} \quad (10)$$

$$C_s = \frac{1}{m}\begin{bmatrix} 1 & 1 & 1 & 1 & \cdots & 1 \\ 1 & a & a^2 & a^3 & \cdots & a^{(m-1)} \\ 1 & a^2 & a^4 & a^6 & \cdots & a^{2(m-1)} \\ 1 & a^3 & a^6 & a^9 & \cdots & a^{3(m-1)} \\ \vdots & \vdots & \vdots & \vdots & \cdots & \vdots \\ a & a^{(m-1)} & a^{2(m-1)} & a^{3(m-1)} & \cdots & a^{(m-1)(m-1)} \end{bmatrix} \quad (11)$$

$$C_{s2} = \frac{1}{m}\begin{bmatrix} 1 & 1 & 1 & 1 & \cdots & 1 \\ 1 & -1 & 1 & -1 & \cdots & -1 \\ 1 & a^2 & a^4 & a^6 & \cdots & a^{2(m-1)} \\ 1 & a^3 & a^6 & a^9 & \cdots & a^{3(m-1)} \\ \vdots & \vdots & \vdots & \vdots & \cdots & \vdots \\ a & a^{(m-1)} & a^{2(m-1)} & a^{3(m-1)} & \cdots & a^{(m-1)(m-1)} \end{bmatrix} \quad (12)$$

The computation of the inverse matrices of C_s or C_{s2} is simple by applying (14) [29]. The matrix $C_s^{-1}$the inverse of C_s is given by (15).

$$C_s^{-1}=m\times C_s^{*T} \quad (14)$$

Furthermore, the transformation matrices can be rewritten to obtain unitary transformation matrices, the case of the matrix C_{su} expressed by (16). The unitary form offers the advantage that the power and torque in a machine, or power in a transformer, resulting from the transformed voltages and currents using a unitary matrix, are invariant [29-30].

$$C_s^{-1} = \begin{bmatrix} 1 & 1 & 1 & 1 & \cdots & 1 \\ 1 & a^{-1} & a^{-2} & a^{-3} & \cdots & a^{-(m-1)} \\ 1 & a^{-2} & a^{-4} & a^{-6} & \cdots & a^{-2(m-1)} \\ 1 & a^3 & a^6 & a^9 & \cdots & a^{3(m-1)} \\ \vdots & \vdots & \vdots & \vdots & \cdots & \vdots \\ 1 & a^{-(m-1)} & a^{-2(m-1)} & a^{-3(m-1)} & \cdots & a^{-(m-1)(m-1)} \end{bmatrix} \quad (15)$$

$$C_{su} = \frac{1}{\sqrt{m}}\begin{bmatrix} 1 & 1 & 1 & 1 & \cdots & 1 \\ 1 & a & a^2 & a^3 & \cdots & a^{(m-1)} \\ 1 & a^2 & a^4 & a^6 & \cdots & a^{2(m-1)} \\ 1 & a^3 & a^6 & a^9 & \cdots & a^{3(m-1)} \\ \vdots & \vdots & \vdots & \vdots & \cdots & \vdots \\ 1 & a^{(m-1)} & a^{2(m-1)} & a^{3(m-1)} & \cdots & a^{(m-1)(m-1)} \end{bmatrix} \quad (16)$$

A. Symmetric Components in Steady state

The subject of SC study focuses on the MES in steady state, where the MES quantities often assumed to be sinusoidal, and are represented by their amplitudes and phase shifts. In general, MESs are represented as complex numbers, regardless of whether they are balanced or unbalanced, as expressed by (17). This calculation method is still employed for determining short-circuit currents in networks and estimating imbalances in MESs, particularly in networks [26-27]. Its continued use is due to its simplicity and its capacity to facilitate the understanding of MES operation in unbalanced conditions.

Moreover, this writing (17) of sinusoidal quantity is easy to represent by the phasor diagrams previously mentioned.

In the equation (17) X_k and ϕ_k are the amplitude and the phase

$$X = \begin{bmatrix} X_1.e^{j\phi_1} \\ X_2.e^{j\phi_2} \\ X_3.e^{j\phi_3} \\ \vdots \\ X_m.e^{j\phi_m} \end{bmatrix} \quad (17)$$

shift respectively, the index $k =1, 2\ldots m$.

In a symmetrical (balanced) MES the amplitudes are equal, and the phase shift angles are written in this form: $k2\pi/m$, where $k =0,1, 2,\ldots (m-1)$. So, the quantities of a symmetric MES are expressed by (18).

$$X = \begin{bmatrix} X \\ X.e^{j\frac{2\pi}{m}} \\ X.e^{j\frac{4\pi}{m}} \\ \vdots \\ X.e^{j\frac{(m-1)2\pi}{m}} \end{bmatrix} \quad (18)$$

The symmetric components, in steady state, of a multiphase system of phase quantities represented by (17), are calculated using one of the two transformations (9) or (10), depending on the parity of the number of phases. Therefore, the SCs, in the case odd m $X_{cs1},\ldots, X_{cs(m-1)}$, represent (m-1) symmetric multiphase systems, and the one zero sequence component which is vector characterized by its calculated amplitude and phase shift, generally the zero sequence component is represented by m vectors in parallel. In the case even m, the SCs $X_{cs1}\ldots, X_{cs(m-2)}$, represent (m-2) symmetric multiphase systems, one zero-sequence component and one pseudo-zero sequence component. The X_{cs1} component is called the positive component or positive sequence (in both cases m odd and even), this represents a symmetrical multiphase system where the sequence of vectors is counterclockwise. In the odd m case, the component $X_{cs(m-1)}$ is called the inverse component or inverse sequence. It represents a symmetrical multiphase

$$X=\begin{bmatrix}\sum_{\nu=0}^{+\infty}X_{(2\upsilon+1)}\\ \sum_{\nu=0}^{+\infty}X_{(2\upsilon+1)}e^{(2\nu+1)\frac{2\pi}{m}}\\ \sum_{\nu=0}^{+\infty}X_{(2\upsilon+1)}e^{(2\nu+1)\frac{4\pi}{m}}\\ \vdots\\ \sum_{\nu=0}^{+\infty}X_{(2\upsilon+1)}e^{(2\nu+1)\frac{(m-1)2\pi}{m}}\end{bmatrix}\qquad(21)$$

Table.III

Harmonic rank	Sequence
vm	Zero sequence
2vm+1	Direct Sequence (contains the Fundamental sequence)
2vm-1	Sequence *(m-1)* called Inverse Sequence
(2v+1) m+2	Sequence 2
(2v+1) m+4	Sequence 3
:	:
(2v+1) m+2(k-1)	Sequence k
:	:
(2v+1) m+2[(m-1)/2-1]	Sequence *(m-1)/2*
(2v+1) m-2[(m-1)/2-1]	Sequence (m+1)/2, is the inverse of the Sequence (m-1)/2
:	:
(2v+1) m-2(k-1)	Sequence (m-k) is the inverse of Sequence k
:	:
(2v+1) m-2	Sequence (m-2) is the inverse of Sequence 2
$1\leq k\leq$ (m-1), and $v\geq 0$	

system where the sequence of vectors is clockwise. In the even case m the inverse sequence is $X_{cs(m-2)}$. The sequence of vectors of a symmetric multiphase system which represents a symmetric component, is said to be direct or inverse according to the clockwise direction.This depends on the transformation matrix C_s, particularly depends on the operator *a*, if $a=e^{j2/m\pi}$, the forward sequence is characterized by clockwise, and the reverse sequence is characterized by counterclockwise. In contarst, if $a=e^{-j\pi 2/m}$, the forward sequence is characterized by counterclockwise, and the forward sequence is characterized by clockwise.

B. Applications of Symmetrical Components to the Analysis of Harmonics

Usually, the waveforms of the quantities of MESs such voltages, currents, and fluxes, are not purely sinusoidal, leading to the appearance of harmonics. The quantities of the MESs are alternating quantities [26-27], and are generally considered symmetrical with respect to the time axis, which translates mathematically to being represented by odd functions. Consequently, the Fourier series expansion of these functions contains only terms of odd rank.

A function f: $\mathbb{R}\rightarrow\mathbb{R}$, is said to be odd function if f satisfies condition (18).

$$f(-x)=-f(x),\ x\in\mathbb{R}\qquad(18)$$

The development of the odd function *f*in a Fourier series is presented in equation (19).

$$f(x)=\sum_{\nu=1}^{+\infty}E_{(2\upsilon+1)}\cos\left((2\nu+1)x+\phi_{\upsilon}\right),\nu\in\mathrm{N}\qquad(19)$$

Hence, the most common harmonics (of currents and voltages) in three-phase systems are odd-order harmonics. This can be generalized in the case of MESs, where representation (20) of the phase quantities of MESs is more general, because in practice even a filtered signal it remains contains a certain amount of harmonics.

Using equation (19), the phase quantity of an MES can be expressed as shown in equation (20).

$$X_k=\sum_{\nu=1}^{+\infty}X_{(2\upsilon+1)}e^{(2\nu+1)\frac{k2\pi}{m}},0\leq k\leq(m-1),(k,\nu)\in\mathrm{N}\qquad(20)$$

As a result, thequantities of the phases of *m*-phase system are given by (21), *m* assumed to be odd.

For an odd number of phases, the SCs of the MES represented by (21) are determined using the transformation (9). Thus, the transformation of the MES (21) into symmetric components is expressed by (22).

The transformation (22) of MES (21) into SC results in symmetrical components having specified harmonic orders. Thus, the transformation (22) creates a classification of the existing harmonics in each symmetrical component. The classes of the harmonics of the symmetrical components are listedin Table.III.

$$\begin{bmatrix}X_{cs0}\\X_{cs1}\\X_{cs2}\\X_{cs3}\\\vdots\\X_{cs(m-1)}\end{bmatrix}=\frac{1}{m}\begin{bmatrix}1&1&1&1&\cdots&1\\1&a&a^2&a^3&\cdots&a^{(m-1)}\\1&a^2&a^4&a^6&\cdots&a^{2(m-1)}\\1&a^3&a^6&a^9&\cdots&a^{3(m-1)}\\\vdots&\vdots&\vdots&\vdots&\cdots&\vdots\\a&a^{(m-1)}&a^{2(m-1)}&a^{3(m-1)}&\cdots&a^{(m-1)(m-1)}\end{bmatrix}\begin{bmatrix}\sum_{\nu=0}^{+\infty}X_{(2\upsilon+1)}\\ \sum_{\nu=0}^{+\infty}X_{(2\upsilon+1)}e^{(2\nu+1)\frac{2\pi}{m}}\\ \sum_{\nu=0}^{+\infty}X_{(2\upsilon+1)}e^{(2\nu+1)\frac{4\pi}{m}}\\ \vdots\\ \sum_{\nu=0}^{+\infty}X_{(2\upsilon+1)}e^{(2\nu+1)\frac{(m-1)2\pi}{m}}\end{bmatrix}\qquad(22)$$

The classes of harmonics of the five-phase, six-phase, seven-phase and nine-phase systems are given in Table.III, and the symmetrical multiphase which represent the sequences $X_{cs1}\ldots X_{cs(m-1)}$ and the associated harmonics are presented in Fig. 8.

C. Instantaneous Symmetric Components

Mathematically, it is possible to apply the transformation into symmetrical components on the instantaneous quantities of phases, this by using the transformation matrices C_s, C_{s2} or C_{su}. This results in instantaneous transformed quantities known as instantaneous symmetrical components (ISC) [32-33]. The ISC concept has been introduced in [30], as referenced in [29].

The ISC transformation can be expressed by (23) if the number of phases is odd, by (24) if the number of phases is even, and by equation (25) for the unitary ISC transformation.

$$\begin{bmatrix}x_{sc0}(t)\\x_{sc1}(t)\\x_{sc2}(t)\\\vdots\\x_{sc(m-1)}(t)\end{bmatrix}=\frac{1}{m}\begin{bmatrix}1&1&1&1&\cdots&1\\1&a&a^2&a^3&\cdots&a^{(m-1)}\\1&a^2&a^4&a^6&\cdots&a^{2(m-1)}\\1&a^3&a^6&a^9&\cdots&a^{3(m-1)}\\\vdots&\vdots&\vdots&\vdots&\cdots&\vdots\\a&a^{(m-1)}&a^{2(m-1)}&a^{3(m-1)}&\cdots&a^{(m-1)(m-1)}\end{bmatrix}\begin{bmatrix}x_1(t)\\x_2(t)\\x_3(t)\\\vdots\\x_m(t)\end{bmatrix}\qquad(23)$$

$$\begin{bmatrix}x_{cs0}(t)\\x_{cs00}(t)\\x_{cs1}(t)\\x_{cs2}(t)\\\vdots\\x_{cs(m-2)}(t)\end{bmatrix}=\frac{1}{m}\begin{bmatrix}1&1&1&1&\cdots&1\\1&-1&1&-1&\cdots&-1\\1&a^2&a^4&a^6&\cdots&a^{2(m-1)}\\1&a^3&a^6&a^9&\cdots&a^{3(m-1)}\\\vdots&\vdots&\vdots&\vdots&\cdots&\vdots\\a&a^{(m-1)}&a^{2(m-1)}&a^{3(m-1)}&\cdots&a^{(m-1)(m-1)}\end{bmatrix}\begin{bmatrix}x_1(t)\\x_2(t)\\x_3(t)\\\vdots\\x_m(t)\end{bmatrix}\qquad(24)$$

The instantaneous quantities of the phases are presented in equation (26). The ISC are presented in equation (27) for an odd number of phases and in equation (28) for an even number of phases.

Since the phase quantities—currents, voltages, fluxes, etc.—are real values, the zero-sequence component is real. In contrast, the other components are complex quantities that vary as a function of time.

$$x(t)=\begin{bmatrix} x_1(t)\\ x_2(t)\\ x_3(t)\\ \vdots\\ x_m(t)\end{bmatrix} \tag{26}$$

$$x_{sc}(t)=\begin{bmatrix} x_{sc1}(t)\\ x_{sc2}(t)\\ x_{sc3}(t)\\ \vdots\\ x_{scm}(t)\end{bmatrix} \tag{27}$$

$$x_{sc}(t)=\begin{bmatrix} x_{cs0}(t)\\ x_{cs00}(t)\\ x_{cs1}(t)\\ x_{cs2}(t)\\ \vdots\\ x_{cs(m-2)}(t)\end{bmatrix} \tag{28}$$

The transformation presented in equation (20), which involves Fourier series development, allows representing each phase quantity by its harmonic series. This can be utilized in ISC transformation. The Fourier series development of a phase quantity is expressed in equation (29). Therefore, the phase quantities can be represented by equation (30).

$$x_k(t)=\sum_{\nu=1}^{+\infty} X_\upsilon \cos\left(\nu.\omega.t+\frac{(k-1)2.\pi}{m}+\phi_{k.\upsilon}\right) \tag{29}$$

$$x(t)=\begin{bmatrix} \sum_{\nu=0}^{+\infty} X_{(2\nu+1)}\cos\left((2\nu+1).\omega.t+\phi_{k.(2\nu+1)}\right)\\ \sum_{\nu=0}^{+\infty} X_{(2\nu+1)}\cos\left((2\nu+1).\omega.t+\frac{2.\pi}{m}+\phi_{k.(2\nu+1)}\right)\\ \sum_{\nu=0}^{+\infty} X_{(2\nu+1)}\cos\left((2\nu+1).\omega.t+\frac{4.\pi}{m}+\phi_{k.(2\nu+1)}\right)\\ \vdots\\ \sum_{\nu=0}^{+\infty} X_{(2\nu+1)}\cos\left((2\nu+1).\omega.t+\frac{(m-1)2.\pi}{m}+\phi_{k.(2\nu+1)}\right)\end{bmatrix} \tag{30}$$

V. Conclusion

This paper discusses the differences between multiphase systems, resulting from phase numbers characteristics. The most important conclusion is that MES is modifiable if its number of phases is factorizable. Where the number of phases can be reduced or the MES can be transformed into multi-star MES. In addition, the possible phase connections are presented, and the impact of the factorizability of the number of phases on these connections is discussed. The variation in voltages between adjacent phases is analyzed as a function of the number of phases. It is observed that this voltage decreases and approaches values lower than the phase voltage. In contrast, the voltages between non-adjacent phases increase with the number of phases and approach twice the phase voltage. The application of the symmetrical components method to multiphase systems (MPSs) is also examined, particularly in terms of how the number of phases affects the symmetrical components. For instance, the emergence of pseudo zero-sequence components in systems with an even number.

$$\begin{bmatrix} x_{sc0}(t)\\ x_{sc1}(t)\\ x_{sc2}(t)\\ \vdots\\ x_{sc(m-1)}(t)\end{bmatrix}=\frac{1}{\sqrt{m}}\begin{bmatrix} 1 & 1 & 1 & 1 & \cdots & 1\\ 1 & a & a^2 & a^3 & \cdots & a^{(m-1)}\\ 1 & a^2 & a^4 & a^6 & \cdots & a^{2(m-1)}\\ 1 & a^3 & a^6 & a^9 & \cdots & a^{3(m-1)}\\ \vdots & \vdots & \vdots & \vdots & \cdots & \vdots\\ 1 & a^{(m-1)} & a^{2(m-1)} & a^{3(m-1)} & \cdots & a^{(m-1)(m-1)}\end{bmatrix}\begin{bmatrix} x_1(t)\\ x_2(t)\\ x_3(t)\\ \vdots\\ x_m(t)\end{bmatrix} \tag{25}$$

References

[1] https://www.iea.org/reports/industry.

[2] Al-Ammari R, Iqbal A, Khandakar A, Rahman S, Padmanaban S. Systematic Implementation of Multi-Phase Power Supply (Three to Six) Conversion System. Electronics. 2019; 8(1):109.

[3] T. L. Landers, R. J. Richeda, E. Krizanskas, J. R. Stewart and R. A. Brown, "High phase order economics: constructing a new transmission line," in *IEEE Transactions on Power Delivery*, vol. 13, no. 4, pp. 1521-1526, Oct. 1998, doi: 10.1109/61.714849.

[4] S.N. Tiwari, G.K. Singh, A.S. Bin Saroor, Multiphase power transmission research—A survey, *Electric Power Systems Research, Volume 24, Issue 3, 1992, Pages 207-215, ISSN 0378-7796.*

[5] T.S. Kishore, S.K. Singal, Optimal economic planning of power transmission lines: A review, Renewable and Sustainable Energy Reviews,Volume 39, 2014,Pages 949-974, ISSN 1364-0321.

[6] A. Barzkar and M. Ghassemi, "Electric Power Systems in More and All Electric Aircraft: A Review," in *IEEE Access*, vol. 8, pp. 169314-169332, 2020, doi: 10.1109/ACCESS.2020.3024168.

[7] XiaokangPeng, Zicheng Liu, Dong Jiang, A review of multiphase energy conversion in wind power generation, Renewable and Sustainable Energy Reviews, Volume 147, 2021, 111172, ISSN 1364-0321,

[8] M. A. Khlifi and M. B. Slimene, "Efficiency of a Six-Phase Induction Generator Employing a Static Excitation Controller to Generate AC Power for Wind Energy," in *IEEE Access*, vol. 11, pp. 28791-28799, 2023, doi: 10.1109/ACCESS.2023.3260775.

[9] Yao G, Pang S, Ying T, Benbouzid M, Ait-Ahmed M, Benkhoris MF. VPSO-SVM-Based Open-Circuit Faults Diagnosis of Five-Phase Marine Current Generator Sets. *Energies.* 2020; 13(22):6004. https://doi.org/10.3390/en13226004.

[10] Chinmaya, K. A., & Singh, G. K. (2018). Performance evaluation of multiphase induction generator in stand-alone and grid-connected wind energy conversion system. *IET Renewable Power Generation*, *12*(7), 823-831.

[11] Y. Liu, S. Niu and W. N. Fu, "A Novel Multiphase Brushless Power-Split Transmission System for Wind Power Generation," in *IEEE Transactions on Magnetics*, vol. 52, no. 2, pp. 1-7, Feb. 2016, Art no. 8100907, doi: 10.1109/TMAG.2015.2496181.

[12] O. Beik and A. S. Al-Adsani, "Parallel Nine-Phase Generator Control in a Medium-Voltage DC Wind System," in *IEEE Transactions on Industrial Electronics*, vol. 67, no. 10, pp. 8112-8122, Oct. 2020, doi: 10.1109/TIE.2019.2947811.

[13] F. Mekri, S. Ben Elghali and M. E. H. Benbouzid, "Fault-Tolerant Control Performance Comparison of Three- and Five-Phase PMSG for Marine Current Turbine Applications," in *IEEE Transactions on Sustainable Energy*, vol. 4, no. 2, pp. 425-433, April 2013, doi: 10.1109/TSTE.2012.2227126.

[14] A. Cavagnino, Z. Li, A. Tenconi and S. Vaschetto, "Integrated Generator for More Electric Engine: Design and Testing of a Scaled-Size Prototype," in *IEEE Transactions on Industry Applications*, vol. 49, no. 5, pp. 2034-2043, Sept.-Oct. 2013, doi: 10.1109/TIA.2013.2259785.

[15] M. S. Abdel-Majeed*et al.*, "Postfault Operation of Onboard Integrated Battery Charger via a Nine-Phase EV-Drive Train," in *IEEE Transactions on Industrial Electronics*, vol. 68, no. 7, pp. 5626-5637, July 2021, doi: 10.1109/TIE.2020.3000125.

[16] V. Madonna, P. Giangrande and M. Galea, "Electrical Power Generation in Aircraft: Review, Challenges, and Opportunities," in *IEEE Transactions on Transportation Electrification*, vol. 4, no. 3, pp. 646-659, Sept. 2018, doi: 10.1109/TTE.2018.2834142

[17] K. Ni *et al.*, "Electrical and Electronic Technologies in More-Electric Aircraft: A Review," in *IEEE Access*, vol. 7, pp. 76145-76166, 2019, doi: 10.1109/ACCESS.2019.2921622.

[18] *https://www.eti.kit.edu/english/1390.php*.

[19] C. L. Fortescue, "Method of Symmetrical Co-Ordinates Applied to the Solution of Polyphase Networks," in *Transactions of the American Institute of Electrical Engineers*, vol. XXXVII, no. 2, pp. 1027-1140, July 1918, doi: 10.1109/T-AIEE.1918.4765570.

[20] Édouard Lefranc, Jean Poinsard et Georges Auclerc, *Électricité – Courant alternatif. Électrostatique - Isolants - Tubes électroniques - Courants alternatifs - Machines - Redresseurs*, Paris, Les Éditions Foucher, 1957, p. 128-130.

[21] JuhaPyrhonen, TapaniJokinen, Valeria Hrabovcova,"Windings of Electrical Machines," in Design of Rotating Electrical Machines, John Wiley & Sons, 2009.

[22] *E. A. Klingshirn, "High Phase Order Induction Motors - Part I-Description and Theoretical Considerations," in IEEE Transactions on Power Apparatus and Systems, vol. PAS-102, no. 1, pp. 47-53, Jan. 1983, doi: 10.1109/TPAS.1983.317996.*

[23] *E. A. Klingshirn, "High Phase Order Induction Motors - Part II. Experimental Results," in IEEE Power Engineering Review, vol. PER-3, no. 1, pp. 27-28, Jan. 1983, doi: 10.1109/MPER.1983.5519569.*

[24] Levi, E.; Jones, M.; Vukosavic, S.N.: 'Even-phase multi-motor vector controlled drive with single inverter supply and series connection of stator windings', IEE Proceedings - Electric Power Applications, 2003, 150, (5), p. 580-590, DOI: 10.1049/ip-epa:20030424.

[25] *E. Levi, M. Jones, S. N. Vukosavic and H. A. Toliyat, "A novel concept of a multiphase, multimotor vector controlled drive system supplied from a single voltage source inverter," in IEEE Transactions on Power Electronics, vol. 19, no. 2, pp. 320-335, March 2004, doi: 10.1109/TPEL.2003.823241.*

[26] *F. Della Torre, S. Leva and A. P. Morando, "Symmetrical Components and Space-Vector Transformations for Four-Phase Networks," in IEEE Transactions on Power Delivery, vol. 23, no. 4, pp. 2191-2200, Oct. 2008, doi: 10.1109/TPWRD.2008.923158.*

[27] *Chicco, Gianfranco, and Andrea Mazza. 2019. "100 Years of Symmetrical Components" Energies 12, no. 3: 450. https://doi.org/10.3390/en12030450.*

[28] IRAVANI, M. R. et KARIMI-GHARTEMANI, M. Online estimation of steady state and instantaneous symmetrical components. *IEE Proceedings-Generation, Transmission and Distribution*, 2003, vol. 150, no 5, p. 616-622.

[29] M. Karimi-Ghartemani and H. Karimi, "Processing of Symmetrical Components in Time-Domain," in *IEEE Transactions on Power Systems*, vol. 22, no. 2, pp. 572-579, May 2007, doi: 10.1109/TPWRS.2007.894860.

[30] *Lyon, W.V. Transient Analysis of Alternating-Current Machinery; John Wiley: New York, NY, USA, 1954.*

Abdelhakim Khelafi received the B.Sc, M.Sc. and PhD degree in electrical engineering from Ecole Nationale Polytechnique (ENP), Algiers, Algeria. His research interests include multiphase machine modeling, multiphase machine design, and multiphase drives.

Abdelmalek Djebli received the B.Sc, M.Sc. and PhD degree in electrical engineering from Ecole Nationale Polytechnique (ENP), Algiers, Algeria. His research interests include multiphase machine modeling, multiphase machine design, and multiphase drives.

Omar Touhami was born in Algeria. He received the Engineer, Magister and Doctorate degrees in Electrical Engineering in 1981, 1986 and 1994 respectively from Ecole Nationale Polytechnique (ENP), Algiers, Algeria. He is currently a professor in Electrical Engineering Department at National Polytechnic School of Algiers. Its field of interest is Domain of research Electrical machines and Variable speed drives.

Rachid Ibtiouen received the Ph.D. degree in electrical engineering from Ecole Nationale Polytechnique (ENP), Algiers, Algeria, and the Institut National Polytechnique de Lorraine, Nancy, France, in 1993. He was with the Groupe de Recherche en Électrotechnique et Électronique de Nancy, Nancy, from 1988 to 1993. From 2005 to 2013, he was the Director of the Laboratoire de Recherche en Electrotechnique with ENP. He is currently a Professor and the Associate Director of research with ENP. His current research interests include the modeling of electric systems and drives, and, in particular, electrical machines. Dr. Ibtiouen was an Expert Member of the Committee of Evaluation of the University Projects of Research with the Comité National d'Evaluation et de Programmation de la Recherche Universitaire, Ministry of the Algerian Higher Education, from 1993 to 2011.

Fractional order control of Wind Energy Conversion System based on DFIG

Samir Metatla, Ali Nesba, and Youcef Soufi

Abstract -- The paper deals with the elaboration of a robust and efficient decoupled active and reactive powers control algorithm of double-fed induction generator (DFIG) using fractional order control based on proportional and integral controllers. First, the models of wind turbine and electrical generator are established as well as a decoupled active and reactive powers control of DFIG. Second, the used fractional order controllers are designed using an analytical design method based on frequency domain specifications, namely phase margin, robustness to gain variations and gain limitation at the crossover frequency. Third, to evaluate the fractional order controller control performances, simulation results are presented and discussed for all the operating region of the WECS. Then, simulation results are presented and interpreted considering a variable wind speed in order to reach all the operating regions of the WECS. Finally, a conclusion is given in the light of the obtained results.

Key words: Fractional order control– WECS–DFIG– analytic design method.

NOMENCLATURE

CRONE	Commande Robuste d'Ordre Non Entier.
DFIG	Doubly Fed Induction Generator.
FOC	Field Oriented Cotrol
FOPI	Fractional Order Proportional and Integral controller
PID	Proportional, Integral and Derivative controller
TID	Tilt Integral and Derivative controller
WECS	Wind Eergy Conversion System.

I. INTRODUCTION

Non-integer order or fractional order control is a generalizedform of classical integer order control theory. Although the notion of non-integer differentiation is not new, its origins go back 300 years, its interest was only recognized at the end of the 20th century when many applications were developed using this concept [1]. Indeed, Bode [2] was the first to propose an ideal transfer function whose phase is flat and independent of the gain and the cutoff frequency. This function was then a reference for the most well-known fractional order control techniques.

In the field of process control, the notion of fractional control was given by the publication of the first works on fractional order control by S. Manabe in 1961 [3] then M. Ichise, et al in 1971 [4] . In 1991, Alain Oustaloup proposed the robust control of non-integer order "CRONE" [5] involving a regulator whose transfer function is of non-integer order to take advantage of the advantageous properties of fractional order systems, and ensure the control robustness in a given frequency range. Since this initiative, several fractional order controls have emerged such as controls based on non-integer observers [6], control by sliding mode of fractional order [7] control by PID controller of fractional order [8] and control by TID regulator. The first objective targeted by the use of fractional order controllers in process control is the introduction of additional degrees of freedom, namely the differentiation order of the transfer functions, which gives more adjustment flexibility. The second objective is the robustness of the command vis-à-vis the uncertainty of the process parameters thanks to the constancy of the phase around the resonance frequency of the process that can be satisfied by a good parameterization of the order controllers fractional [5,9,10].

Manuscript received October 13, 2022; revised November 3, 2024.

S. Metatla, and Y. Soufi are with LABGET Research Laboratory, Electrical engineering department, University Larbi Tebessi – Tebessa, Algeria, (e-mail: metatla.samir@gmail.com, y_soufi@yahoo.fr)
A. Nesba is with LSIC Research Laboratory Ecole Normale Supérieure de Kouba Algiers, Algeria, (e-mail: ali.nesba@gmail.com)

Digital Object Identifier (DOI): 10.53907/enpesj.v4i2.141

The work that is the subject of this paper focuses on the establishment of a robust and efficient fractional order control by involving proportional and integral type regulators of non-integer order (FOPI) of the form $(PI)^{\alpha}$ in order to ensure the control of a variable speed wind turbine based on double-fed induction generator (DFIG). The sizing of the fractional regulators used is ensured by an analytical method calling on a mathematical development based on the performance and robustness criteria in the frequency domain, namely the phase margin, the robustness to gain variations and the limitation of the gain to the frequency of the cutoff [9]. Simulation results will be presented and discussed in order to evaluate the performance of the proposed fractional control.

II. FRACTIONAL ORDER CONTROL

The main interest of fractional order control is to improve the performance of control systems and to give more tuning flexibility by using the concepts of non-integer differentiation. Indeed, fractional order regulators offer more tuning flexibility thanks to the additional degree of freedom, namely the order of the differentiation.

$$C(s) = (PI)^{\alpha} = \left(k_p + \frac{k_i}{s}\right)^{\alpha} \tag{1}$$

Such ask_p: Is the proportional gain, k_i: The integral gain and α the integration order.

The ideal power curve ofa variable speed WECS can be described by Fig. 1. As we can see, it ischaracterized by fourdifferentoperating regions with distinct generation objectives. In the first region wind speed is not sufficient to drive the WECS,so the wind turbine remains out of operation. For winds with moderate speed that exceed the cut in wind speed $v_{cut\ in}$, the aerodynamic power is then sufficient to start the aerodynamic conversion process which characterize the second operating region of the WECS. In the second operating region, the main objective is the extraction of maximum power from the wind. However, for wind speed that exceeds the rated value (region III),theconvertedaerodynamic power reachesthe WECS rated power. The pitch control system should act on blade pitch angle so that the generated power remains equal to its rated value in order to avoid mechanical and electrical overloads. In the last region (region IV), wind speedexceeds itslimit value$v_{cut\ off}$, wind turbine should be stopped to avoid WECS destruction.

In order to protect the WECS from excessive rotational speeds, the second operating region is often subdivided into two different subregions with distinctcontrol objectives. In fact, forrotational speed lower than the rotorrated speed value, the control objective is the maximum power point tracking. In this case the optimal aerodynamic conversion efficiency is achieved which characterize the first subregion. However, in the second subregion, the control system should limit the wind turbine speed to its rated valuedue to mechanical and acoustic constraints [11].

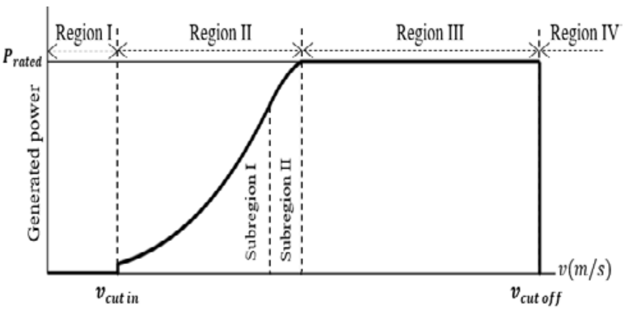

Fig. 1: Wind turbine ideal power curve

III. WIND ENERGY CONVERSION SYSTEM MODELING AND CONTROL

A wind energy conversion system (WECS) is often composed of three essential parts. A wind turbine, an electrical generator and a control and management. in fact, WECS modeling consists of modeling each of its components.

A. Wind turbine modeling

The main interest of the wind turbines is theconversion of aerodynamicpower into mechanical power. The aerodynamic conversion theory is widely developed and discussed in the literature [12,13]. The aerodynamic conversion process of a variable speed wind turbine can be described by the following bloc diagram [11].

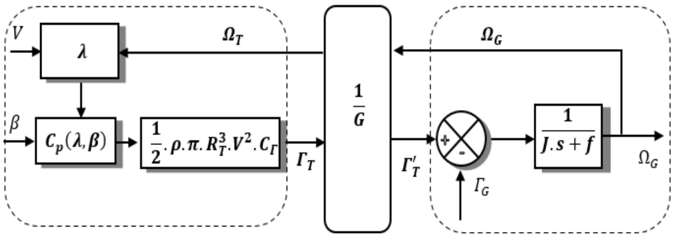

Fig. 2: Wind turbine model block diagram

Where:

$\boldsymbol{\lambda} = \frac{\boldsymbol{R_T} . \boldsymbol{\Omega_T}}{\boldsymbol{V}}$ is the tip speed ratio, $\boldsymbol{R_T}$ and $\boldsymbol{\Omega_T}$ are turbine radius and speed respectively.

The power coefficient of the wind turbine is given by:

$$C_p(\lambda,\beta) = C_1.\left(C_2.\frac{1}{\Lambda} - C_3.\beta - C_4\right)e^{\frac{-C_5}{\Lambda}} + C_6.\lambda \qquad (2)$$

Whereβ is the blade pitch angle and $C_1, \ldots,\ C_6$ are parameters which dependon the aerodynamic of the wind turbine.

The wind turbine aerodynamic torque is given by:

$$\Gamma_T = \frac{1}{2}.\rho.\pi.R_T^3.V^2.\frac{C_p(\lambda,\beta)}{\lambda} \qquad (3)$$

Where ρ is the air density and V is the wind speed.

Γ_G is the generator torque,G is the gearbox ratio, f, J and$\Gamma_T' = \frac{\Gamma_T}{G}$are the friction coefficient, inertia and theaerodynamic torque,of the wind turbine referred to high speed shaft respectively.

B. DFIG modeling and control

DFIG modeling and control is widely discussed in the literature [11,14-16]. The mathematical model ofDFIGreferred to an arbitrary rotating reference frame can be expressed by the following equations:

$$\begin{cases} V_{ds} = R_s I_{ds} + \frac{d}{dt}\varphi_{ds} - \omega_s.\varphi_{qs} \\ V_{qs} = R_s I_{qs} + \frac{d}{dt}\varphi_{qs} + \omega_s.\varphi_{ds} \\ V_{dr} = R_r I_{dr} + \frac{d}{dt}\varphi_{dr} - (\omega_s - \omega).\varphi_{qr} \\ V_{qr} = R_r I_{qr} + \frac{d}{dt}\varphi_{qr} + (\omega_s - \omega).\varphi_{dr} \end{cases} \qquad (4)$$

Where$I_{ds}, I_{qs}, V_{ds}, V_{qs}, \varphi_{ds}, \varphi_{qs}$ are the stator current, voltage and flux along the d and q axis, $I_{dr}, I_{qr}, V_{dr}, V_{qr}, \varphi_{dr}, \varphi_{qr}$ are the rotor current, voltage and flux along the d and q axisrespectively andR_s, R_r are the stator and rotor winding resistances; ω_s and ω are the synchronous and rotor speeds.

The stator and rotor flux equations are given by:

$$\begin{cases} \varphi_{ds} = L_s I_{ds} + M.I_{dr} \\ \varphi_{qs} = L_s I_{qs} + M.I_{qr} \\ \varphi_{dr} = L_r I_{dr} + M.I_{ds} \\ \varphi_{qr} = L_r I_{qr} + M.I_{qs} \end{cases} \qquad (5)$$

With L_s, L_r and M are the stator inductance, the stator inductance and the mutual inductance respectively.

The objective of DFIG control is to achieve decoupled power control. By applying a field-oriented control strategy (FOC) to the DFIG model described by equations (4) and (5), we can derive the DFIG model depicted in the block diagram in Fig.3 below [17, 18].

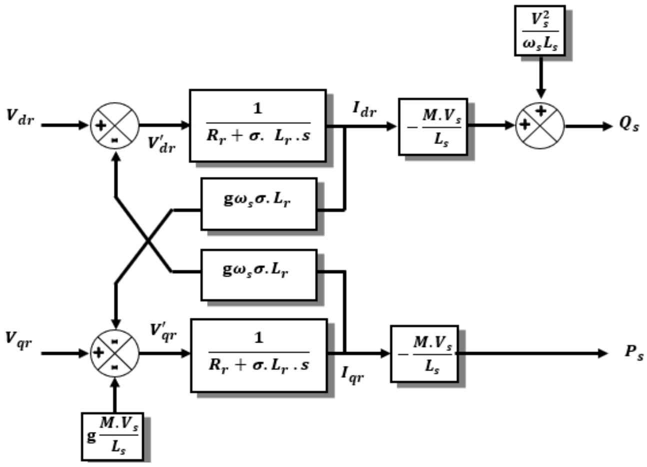

Fig. 3: DFIG model block diagram

Taking into account the DFIG block diagram shown in Fig. 3, decoupled equations for active and reactive powers can be derived to establish separate control of active and reactive powers for the DFIG. Assuming that cross-coupling terms between the d and q axes are fully compensated, active and reactive powers can be expressed as functions of the direct and quadrature rotor voltages, respectively.

$$\begin{cases} P_s = \left(-\dfrac{M.V_s}{R_r L_s}\right)\dfrac{1}{\left(1+\sigma.\frac{L_r}{R_r}.s\right)}.V'_{qr} \\ Q_s - \dfrac{V_s^2}{\omega_s.L_s} = \left(-\dfrac{M.V_s}{R_r L_s}\right)\dfrac{1}{\left(1+\sigma.\frac{L_r}{R_r}.s\right)}.V'_{dr} \end{cases} \quad (6)$$

By setting: $T = \frac{L_r}{R_r}$and $k = -\frac{M.V_s}{R_r L_s}$, we can write:

$$\begin{cases} P_s = \dfrac{k}{1+\sigma.T.s}.V'_{qr} \\ Q_s - \dfrac{V_s^2}{\omega_s.L_s} = \dfrac{k}{1+\sigma.T.s}.V'_{dr} \end{cases} \quad (7)$$

Then we can deduce the DFIG model for decoupled active and reactive powers control as presented below.

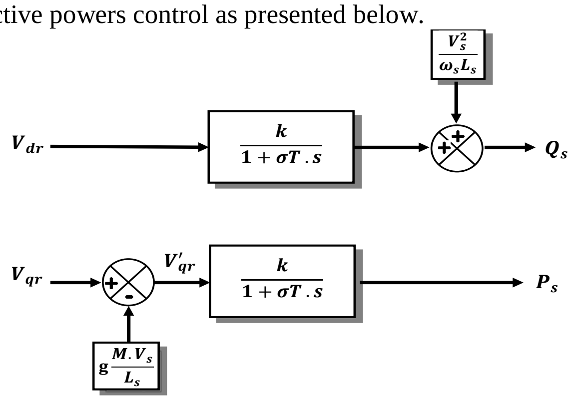

Fig. 4: DFIG model block diagram for decoupled powers control

With: $\sigma = \left(1-\frac{M^2}{L_s.L_r}\right)$the dispersion coefficient, $T = \frac{L_r}{R_r}$ the rotor time constant and $k = -\frac{MV_s}{R_r.L_s}$ a constant depends on DFIG parameters.

The decoupled control loop of active and reactive powers can be presented by the block diagram presented in Fig. 5.

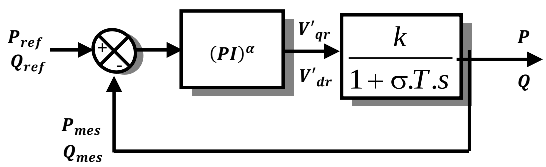

Fig. 5: Control loop of active and reactive powers decoupledcontrol

IV. FRACTIONAL ORDER CONTROLLER DESIGN

In industrial process control systems, controller design is a crucial step. Tuning the parameters of these controllers is critical for ensuring robustness, stability, and performance of the entire process. The non-integer controllers used in this study are designed based on frequency domain specifications using an analytic design method. The design specifications include phase margin, robustness to gain variation, and gain margin [11].

A. Phase margin ϕ_m

Phase margin is an importantperformance and robustness criteria and can affects thesystem damping [14, 19, 20]. The phase margin is given by:

$$arg[plant + controller]_{\omega_c} = \phi_m - \pi \quad (8)$$

Where ω_c is the crossover frequency.

By applying the phase margin specification on the decoupled active and reactive powers control loop in Fig. 5 we find:

$$arg[C(s).P(s)]_{\omega_c} = \phi_m - \pi$$

Introducing transfer fuctions expressions we can write.

$$arg\left[\left(k_p + \frac{k_i}{s}\right)^\alpha.\left(\frac{k}{1+\sigma T.s}\right)\right] = \phi_m - \pi$$

Replacing Laplace operator s by $j\omega_c$ at crossover frequency we can write.

$$-\alpha\, arctan\left(\frac{k_i}{k_p.\omega_c}\right) - arctan(\sigma T.\omega_c) = \phi_m - \pi \quad (9)$$

Equation (9) can be simplified by setting $A = (\pi - \phi_m - arctan\sigma T.\omega c$ as:

$$k_i = k_p.\omega_c\, tan\left(\frac{A}{\alpha}\right) \quad (10)$$

B. Robustness to gain variation

The use ofrobustness to gain variation specification can ensures a flat phase around ω_c which gives more statbility and mor robustness against internal perturbations like parameters variation [11,14,19,20,21]. Robustness to gain variation cretaria is defined by:

$$\left.\frac{d(arg[C(s).P(s)])}{d\omega}\right|_{\omega_c} = 0 \quad (11)$$

By applying on decoupled powers control loop we can find.

$$\alpha.\frac{k_i/(k_p.\omega_c^2)}{1+\left(k_i/k_p.\omega_c\right)^2} - \frac{\sigma.T}{1+(\sigma T.\omega_c)^2} = 0 \quad (12)$$

In order to simplify (10) we set $B = \frac{\sigma.T}{1+(\sigma T.\omega_c)^2}$, so (12) can takes the forme:

$$\alpha.\frac{k_i/\left(k_p.\omega_c^2\right)}{1+\left(k_i/k_p.\omega_c\right)^2} = B \tag{13}$$

C. Gain limitation at crossover frequency

This specification reflects the stability margin of the controled system. It is an important creteria for non-integerorder controllers design [11, 19,20,22].

$$|C(j\omega).P(j\omega)|_{\omega_c} = 1 \tag{14}$$

Which gives.

$$\left(k_p\right)^2 + \left(\frac{k_i}{\omega_c}\right)^2 = \left[\frac{\sigma.T}{k.B}\right]^{\frac{1}{\alpha}} \tag{15}$$

The substitution of (10) in (15) and (10) in (13) leads to the following equations.

$$k_p = \left[\frac{\left[\frac{\sigma.T}{k.B}\right]^{\frac{1}{\alpha}}}{1+tan^2\left(\frac{A}{\alpha}\right)}\right]^{\frac{1}{2}} \tag{16}$$

$$\frac{\alpha}{\omega_c}.\frac{tan\left(\frac{A}{\alpha}\right)}{1+tan^2\left(\frac{A}{\alpha}\right)} = B \tag{17}$$

Using trigonometric relations, (17) can takes the following form:

$$\frac{\alpha}{\omega_c}.\frac{1}{2}sin\left(2.\frac{A}{\alpha}\right) = B \tag{18}$$

Therefore, (18) may be written as:

$$\frac{sin\left(2.\frac{A}{\alpha}\right)}{2.\frac{A}{\alpha}} = \frac{B.\omega_c}{A} \tag{19}$$

Then we can express (19) as:

$$\text{sinc}\left(2.\frac{A}{\alpha}\right) = \frac{B.\omega_c}{A} \tag{20}$$

Where sinc is cardinal sine function.

Indeed, the used FOPI controller design strategy can be resumed by (10), (16) and (20) equations. In fact, fractional order integration α can be fined from (20), then we can deduceproportional gaink_p from (16) and integration gaink_i from (10).

Taking into account the mathematical study detailed in the above sections, the control system block diagram of the considered WECS can be presented by Fig. 6. In the considred WECS we use speed limitation and pitch control systems as we can see in Figure bellow.

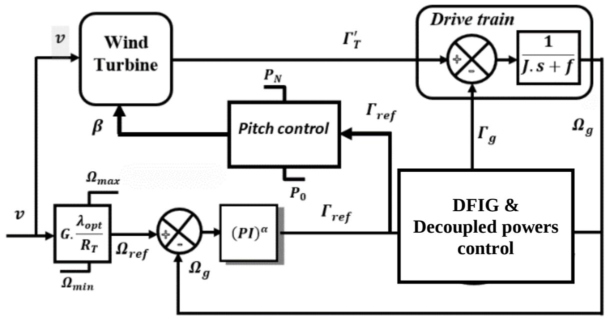

Fig. 6: Proposed fractional order control block diagram

V. SIMULATION AND DISCUSSION

Simulation results presented in this section are obtained by applying the proposed fractional order control presented in Fig. 6 on a WECS with parameters given in the table below.

TABLE I. WECSPARAMETERS

Parameter	*symbol*	*Value*
Rated power	P_n	**300 kW**
Rated stator voltage	V_n	**690 V**
Stator resistance	R_s	**54 mΩ**
Rotor resistance	R_r	**46 mΩ**
Stator inductance	L_s	**12.9 mH**
Rotor inductance	L_r	**12.7 mH**
Magnetizing inductance	M	**12.5 mH**
Nominal stator frequency	f	**50 Hz**
Number of pole pairs	P	**2**
Blade radius	R_T	**28 m**
Number of turbine blades	///	**3**
Total inertia	J	**42.9 kg.m²**
Gearbox ratio	G	**1 : 30**

Fractional order controllers used are tuned using the proposed analytical design method.

TABLE II. FRACTIONAL ORDER CONTROLLER PARAMETERS

Parameter	*symbol*	*Powers controllers*	*Speed controller*
Proportional gain	K_p	**786.3**	**73**
Integration gain	K_i	**1844**	**144**
Integration order	α	**0.588**	**0.88**

All the operating regions are covered considering a wind profile with a variable wind speed between 6 m/s and 17 m/s.

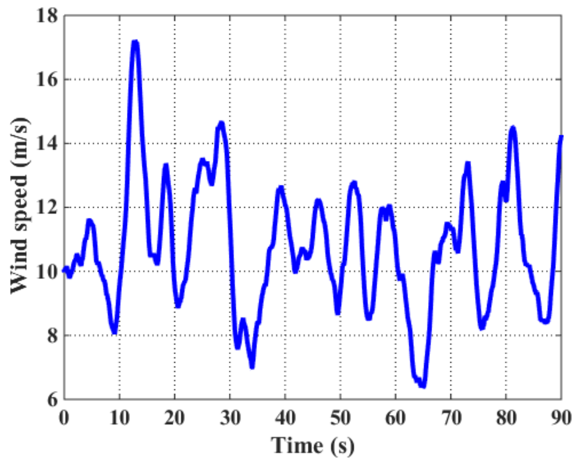

Fig. 7: Wind speed profile

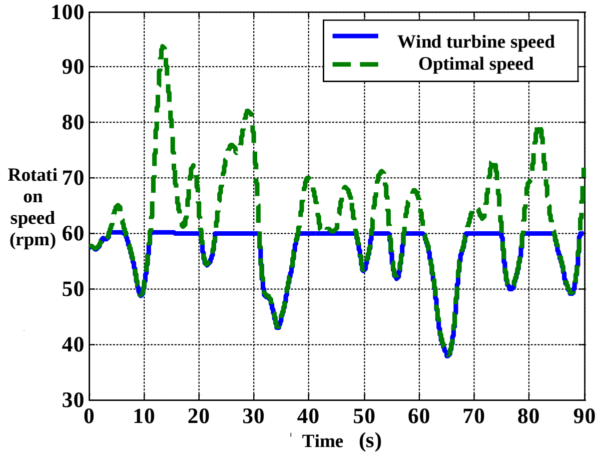

Fig. 8: Wind turbine speed

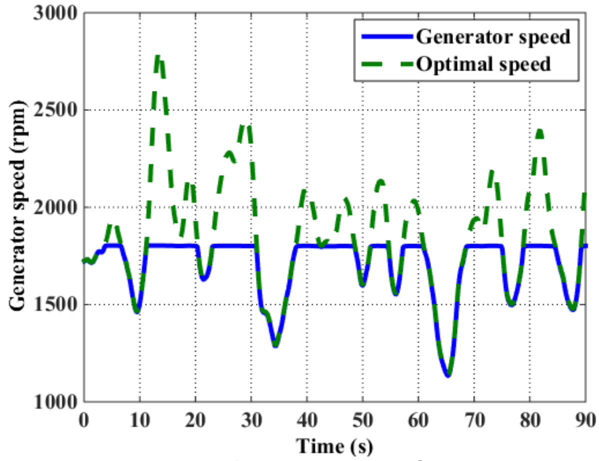

Fig. 9: Generator speed

Figures 8 and 9 show that for wind speeds below 11m/s, the rotational speed of the wind turbine and generator speed follow the reference speed very well. We therefore note that control objectives in subregion I of the second operating region is the maximum power point tracking which is confirmed by the result presented on Fig. 10. However, for wind speeds greater than 11m/s, rotation speed of the wind turbine as well as the rotation speed of the electric generator are limited to 60 rpm and 1800 rpm respectively thanks to the speed limitation system. Speed limitation in the second subregion of region II is very important due to mechanical and acoustic constraints.

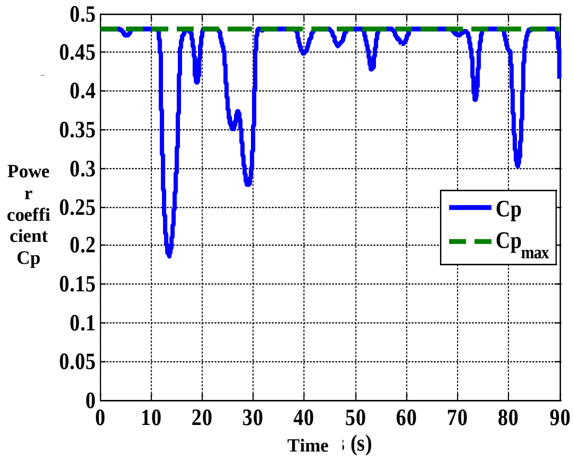

Fig. 10 : Power coefficient

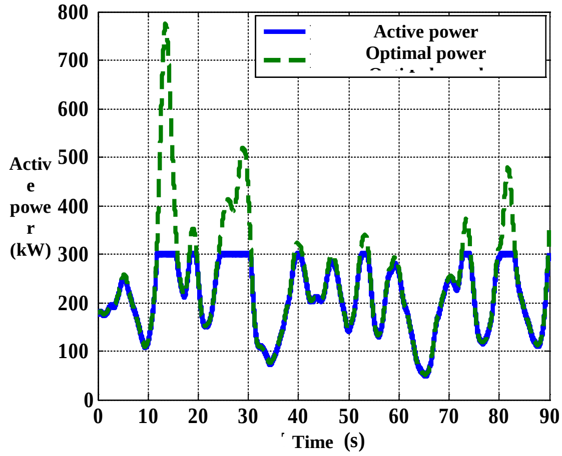

Fig. 11 : Active power variation

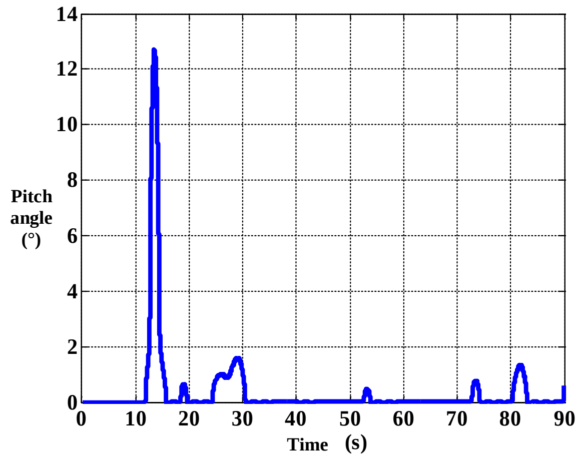

Fig. 12: Pitch angle

For wind speed that exceeds12m/s, the nominal power of the wind turbine is reached as we can see on Fig. 11. Therefore, the control objective will be to protect the wind turbine against overloads by adjusting turbine blades pitch angle in order to limit the converted power to the nominal power of the wind turbine which can be seen in Fig. 11 and Fig.12. In the light of the presented simulation results we can deduce an improved performance of the controlled system using the proposed non-integer order control.

In order to give a good view of the performance of the proposed fractional order control, we have introduced results presented in Fig. 13 on which we can distinguish easily operation regions of the wind turbine. Indeed, on Fig. 13 we can easily distinguish the operating region II, for wind speed lower than 11 m/s, where the control objective is the maximum power extraction which is affirmed by the follow-up of the active power to its reference curve. However, for wind speed higher than 11 m/s the control objective is no longer the maximum power extraction but rather the speed limitation which is confirmed by result presented on Fig. 14. Moreover, when wind speed reaches 12,5 m/s, the wind turbine is then at its nominal power, hence the operating objective becomes the protection of the wind turbine by limiting the extracted power to its nominal value using the pitch angle control system as presented in Fig. 13.

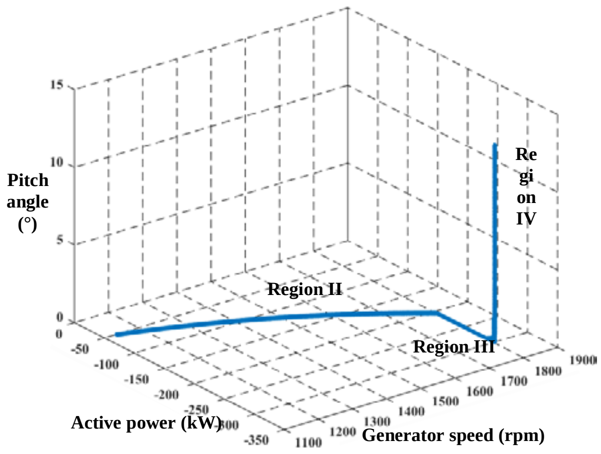

Fig. 13: Operating characteristics of WECS (P, Ω_g, β).

Finaly, performances of the WECS using the proposed fractional order control can be resumed by the results presented on Fig.13 on which all operation regions can be easily distinguished. In fact, the first region characterized by maximum power extraction which spreads out from 50 kW up to 200 kW on the power axis. Then region II in which the rotation speed is limited to 1800 rpm for mechanical and acoustic reasons and finally the third region where the converted power is limited by action on the blade pitch angle to protect the wind turbine from destruction.

VI. CONCLUSION

In present work, afractional order control is proposed. The used FOPI controllers are designed based on three specifications in frequency domain using a proposed analytic method. The WECS performance using the proposed non-integer control are presented with model simulation in Matlab. Indeed, the interest targets have been achieved as we ca see on the obtained results, which show a good performance of the considered WECS. The results also show effectiveness in the operation of the WECS in three regions of operation with satisfaction regarding references tracking and convergence. In fact, simulation results are very attractive and ensuring stability, quality and efficiency of WECS. Finaly, from the simulation results presented in this paper, it can be concluded that the proposed non-integer control has improved performances of the studied WECS.

ACKNOWLEDGEMENT

Part of this work has been performed with the Late Professor Said *Mekhtoub.*

REFERENCES

[1]. B. Ross, "*Fractional calculus and its applications*" Lecture Notes in Mathematics, volume 457, West Haven, Springer, 1974.

[2]. H. W. Bode, « *Network Analysis and Feedback Amplifier Design* », New York, D. Van Nostrand, 1945.

[3]. S. Manabe, « *The non-integer integral and its application to control systems* », The Journal of the Institute of Electrical Engineers of Japan, Volume 80, Issue 860, 1960, pp. 589-597.

[4]. M. Ichise, Y.Nagayanagi, T.Kojima, « *An analog simulation of non-integer order transfer functions for analysis of electrode processes* », Journal of electroanalytical chemistry and interfacial electrochemistry, Volume 33, Issue 2, December 1971, pp. 253-265. DOI : 10.1016/S0022-0728(71)80115-8

[5]. A. Oustaloup, « *La commande CRONE : Commande robuste d'ordre non entier* », Paris, Edition Hermès, 1991.

[6]. D. Matignon, B. d'Andrea-Novel, « *Observer-based controllers for fractional differential systems* » Proceedings of the 36th IEEE Conference on Decision and Control, 1997, pp. 4967-4972 vol.5. DOI: 10.1109/CDC.1997.649835

[7]. N. Bouarroudj, D. Boukhetala, F. Boudjema « *Sliding-Mode Controller Based on Fractional Order Calculus For a Class of Nonlinear Systems* », International Journal of Electrical and Computer Engineering (IJECE), Vol. 6, No. 5, October 2016, pp. 2239 – 2250. DOI: http://doi.org/10.11591/ijece.v6i5.pp2239-2250

[8]. I. Podlubny, « *Fractional order systems and PIλDμ Controllers* », IEEE Transactions on automatic control, Vol. 44, No. 1, January 1999, pp. 208-214. DOI: 10.1109/9.739144

[9]. S. Metatla, S. Mekhtoub, A. Nesba, I. Colak, M. Ouadah, « *Analytical design of fractional order proportional-integral controller for enhanced power control of Doubly-Fed Induction Generator* », Rev. Roum. Sci. Techn.–Électrotechn. et Énerg. Vol. 65, No.1-2, 2020, pp. 109–115.

[10]. H. Mahvash, S. A. Taher, M. Rahimi, M. Shahidehpour, « *DFIG performance improvement in grid connected mode by using fractional order [PI] controller* », International journal of electrical power & energy systems, Volume 96, March 2018, pp. 398-411. DOI:https://doi.org/10.1016/j.ijepes.2017.10.008

[11]. S. Metatla, A. Nesba, Y. Soufi, S. Mekhtoub, "*Performance improvement of variable speed wind turbine based on fractional order control*", 5th International Conference on Power Electronics and their Applications (ICPEA), 2022, pp. 1-8.

[12]. F. D. Bianchi, H. De Battista and R. J. Mantz, "*Wind Turbine Control Systems, Principles, Modelling and Gain Scheduling Design*", Springer, Germany, 2007.

[13]. S.M. Muyeen, Mohd. Hasan Ali, T. Rion, M. Toshiaki, T. Junji, T. Yuichi, S. Atsushi, S. Eiichi, "*Comparative study on transient stability analysis of wind turbine generator system using different drive train models*". Renew. Power. Gener. IET. Volume. 1, No.2, 2007, pp.131–141. DOI: 10.1049/iet-rpg:20060030

[14]. H. Mahvash, S. A. Taher, M. Rahimi"*Enhancement of DFIG performance at high wind speed using fractional order PI controller in pitch compensation loop*"Electrical Power and Energy Systems, Volume 104, pp259-268. DOI:https://doi.org/10.1016/j.ijepes.2018.07.009

[15]. L. Xu and C. Phillip, "*Direct active and reactive power control of DFIG for wind energy generation*," IEEE Transa. Energy Conver, Volume 21, No. 3, 2006, pp. 750-758. DOI: 10.1109/TEC.2006.875472

[16]. Hamane. B, Doumbia. M. L, Bouhamida. A. M, Benghanem. M, "*Direct active and reactive power control of DFIG based WECS using PI and sliding mode controllers*", 40th Annu. Conf. of the IEEE IES, Dallas 2014, pp. 2050-2055. DOI: 10.1109/IECON.2014.7048784

[17]. F. Mazouz, S. Belkacem, Y. Harbouche, R. Abdessemed and S. Ouchen, "*Active and reactive power control of a DFIG for variable speed wind energy conversion*," 6th Int. Conf. Syst, 2017, pp. 27-32 DOI: 10.1109/ICoSC.2017.7958642

[18]. S. Metatla, S. Mekhtoub, Ali. Nesba, Y. Soufi and M. Ouadah, "*An Optimized Fractional Order PI Controller to Improve DFIG Active and Reactive Powers Control,*" *12th Int. Symp. Adv. Top. Electr. Eng (ATEE)*, 2021, pp. 1-6. DOI: 10.1109/ATEE52255.2021.9425298

[19]. A. Monje, Blas M. Vinagre, Vicente Feliu, YangQuan Chen, "*Tuning and auto-tuning of fractional order controllers for industry applications*", Cont. Eng. Pract, Vol. 16, No. 7, 2008, pp. 798-812, DOI:https://doi.org/10.1016/j.conengprac.2007.08.006

[20]. D. Saptarshi, S. Suman, D. Shantanu, G. Amitava, "*On the selection of tuning methodology of FOPID controllers for the control of higher order processes,*" ISA Transactions, Vol. 50, Issue 3, 2011, pp.376-388, DOI:https://doi.org/10.1016/j.isatra.2011.02.003

[21]. C. Y. Wang, Y. Luo, Y. Q. Chen. "*An analytical design of fractional order proportional integral and [proportional integral] controllers for robust velocity servo*", 14th IEEE Conference on Ind. Electron. & Appl. 2009. pp 3448–3453. DOI: 10.1109/ICIEA.2009.5138847

[22]. RD. Keyser, CI. Muresan, CM. Ionescu. "*A novel auto-tuning method for fractional order PI/PD controllers*", ISA Transactions, 62, 3, May 2016. pp 268–275. DOI:https://doi.org/10.1016/j.isatra.2016.01.021

Samir Metatla received his PhD degree in electrical engineering from Ecole Nationale Polytechnique (ENP), Algiers in 2023. He is currently assistant Professor at University Larbi Tebessi – Tebessa. His research interests include Energy Conversion, Electrical Power Engineering, Power Converters, and Power Electronics.

Integral Sliding Mode Control with Dual-Hormone for an Artificial Pancreas

Saoussane Mahour, Mohamed Tadjine, and Messaoud Chakir

Abstract−Low concentration of glucose, "hypoglycemia" is the most critical complication for type 1 diabetes patients, may lead to coma or death. For this purpose, a dual-hormonal control of glycaemia is required, using insulin to recover the period of hyperglycemia and glucagon to treat hypoglycemia. In this study, an extended mathematical model of blood glucose is presented, taking into account the dynamics of the glucagon hormone. An Integral Sliding Mode Control ISMC was developed using a hysteresis switch between two hormones, "insulin and glucagon".The numerical simulation results show that the proposed controllers have many advantages, such as robustness to parameter variance, change in the initial condition, and external disturbance.

***Keywords*− Integral sliding mode control, dual hormone, artificial pancreas, lyapunov stability.**

NOMENCLATURE

AP	Artificial Pancreas
BGL	Blood Glucose Level
ISMC	Integral Sliding Mode Control
PID	Proportional-Integral-Derivative
TIDM	Type 1 Diabetes Mellitus

I. INTRODUCTION

Diabetes is a chronic metabolic illness caused by a lack production or deficient action of insulin (concentration of glycemia above 180 mg/dl) .Type 1 diabetes is the one of this disease, the human body's does not aptitude to secret the insulin by the beta cells of pancreas, which causes several risks to these patients' health [1] .The symptoms of this diabetes includes urination, thirst ,losing weight ,hunger increased appetite and feeling tired [2].Control blood glucose decreases the risk of long-term diabetes-related complications, such as kidney disease, heart disease, blindness, and peripheral vascular and nerve damage [1]. The two methods of treatment for type 1 diabetes patients are multiple daily injections or continuous subcutaneous infusion via a portable pump. In recent years, the development of a novel device to build automated insulin delivery systems and to manage the blood glucose, known as the artificial pancreas[3]. however, intensive insulin treatment, including the artificial pancreas, can raise the risk of hypoglycemia with potentially severe complications, including coma or death [4]. Moreover, a closed-loop system retaining the dual hormone insulin infusion and glucagon has confirmed its efficacy in avoiding and treating hypoglycemia[5], [6] ; bihormonal systems would better emulate the endocrine pancreas function [7]. Several authors[5], [8], [9]have stated that a bihormonal closed-loop algorithm could provide asafe blood glucose regulation and significantly reduce the risk and time spent in hypoglycemic episodes [10] compared to usual insulin therapy. However, the dual-hormone systems have shown better results during exercise studies [10]. Besides, recent studies[11] have demonstrated that adding glucagon delivery to the closed-loop system with automatic exercise detection reduces hypoglycemia after aerobic exercise. To maintain the BGL in the normal range, approximately between 70-120 mg/dl for a healthy human and deal with hypoglycemia and hyperglycemia conditions, several control strategies have been designed and tested for the artificial pancreas: neural control[12], H∞ control[13], PID control[14], model predictive control[15], sliding control[16]. Among these controllers, Sliding Mode Control has received much attention in biomedical studies due to its unique features such as strong robustness, fast convergence rate, and simplicity[17], [18]. Sliding mode control is an efficient approach to dealing with the model uncertainties, nonlinearities, and bounded external disturbance[4]. The control technique has a number of advantages when compared with other nonlinear controllers. It has been implemented on photo-voltaic system [19] Leukemia therapy [20] and blood glucose regulation[4], [16].

This study aims to develop a control algorithm that maintains the blood glucose concentration in subjects with T1DM in a safe range using an integral sliding mode control and adopting a dual hormone strategy by adding glucagon administration to insulin delivery. Numerical simulations illustrate the contribution of glucagon to achieving control goals, with no hypoglycemic or hyperglycemic events observed. The remainder of this paper is organized as follows: Section 2 describes the nonlinear model of the insulin-glucose-glucagon system and synthesizes the dual hormone controller applying to the integral slide mode method; section 3 discusses the obtained results; Section 4 concludes the paper.

II. MATERIALS AND METHODS

Mathematical model

Many researchers have studied the glucose-insulin-glucagon endocrine and metabolic regulatory system. Therefore, different models for the glucoregulatory system are available [21], [22], [23] with different structures and degrees of complexity. The model developed by Ben Abbes et al (2013) [24]and extended by Mahour et al. (2022) [25]was chosen for this study to represent the diabetic patient (virtual subject).

Manuscript received July 17, 2024; revised December 10, 2024.

S.MAHOUR, M. TADJINE and M.CHAKIR are with Process Control Laboratory at EcoleNationalePolytechnique, Algiers, Algeria. (e-mail: saoussane.mahour@g.enp.edu.dz, mohamed.tadjine@g.enp.edu.dz, messaoud.chakir@g.enp.edu.dz)

Digital Object Identifier (DOI): 10.53907/enpesj.v4i2.280

The mathematical description of the system is given as follows:

$$\dot{x_1}(t) = -P_1 x_1(t) - P_2 x_1(t) e^{S_1 i_2(t)} + K_{gr} m_4(t) + P_3 g_6(t) \quad (1)$$

$$\dot{i_2}(t) = -W_{in2}\big(i_2(t) - i_3(t)\big) \quad (2)$$

$$\dot{i_3}(t) = -W_{in1}\big(i_3(t) - U_{ins}(t)\big) \quad (3)$$

$$\dot{m_4}(t) = -W_{r2}\big(m_4(t) - m_5(t)\big) \quad (4)$$

$$\dot{m_5}(t) = -W_{r1}\left(m_5(t) - U_{rep}(t)\right) \quad (5)$$

$$\dot{g_6}(t) = -W_{g2}\big(g_6(t) - g_7(t)\big) \quad (6)$$

$$\dot{g_7}(t) = -W_{g1}\left(g_7(t) - U_g(t)\right) \quad (7)$$

$$y(t) = x_1(t) \quad (8)$$

x_1 : Glycemia concentration,
i_2, i_3 :Insulin concentration in distant compartments,
m_4, m_5: Quantity of ingested carbohydrate.
g_6, g_7 :Glucagon concentration in distant compartments,
P_1: Constant expressing the decline of glucose affected by glucose uptake by cells, independent of the insulin blood concentration,
P_2: Gain in the double action of the pair insulin– glucose on glucose
P_3: Glucagon action on glucose production,
S_1: Gain in the action of insulin on glucose.
K_{gr} **:** Carbohydrates action on glucose production.
U_{ins} ,U_{rep} , U_g:Injected insulin; ingested carbohydrates and injected glucagon,
W_{in1}, W_{in2}**:** Values related with the distribution of insulin,
W_{r1}, W_{r2}: Constants related with the distribution of carbohydrates,
W_{g1}, W_{g2}: Constants related with glucagon diffusion,

Controller design

Consider system described by (1)-(8) is presented as follows form:

$$\dot{x}(t) = f\big(t, x(t)\big) + g_1(t)u_1(t) + g_2(t)u_2(t); \quad (9)$$

Where x(t) is a measurable states, $u_1$and u_2 are the control inputs, f (x, t) and g(x, t) are unknown nonlinear time-variant functions.

Reference trajectory of $x(t)$ is a known bounded x_r=1g/l. This value was chosen so that the blood glucose level of the patient with T1DM would remain within safe limits by the medical community: 80 and 100 mg /dL .The dual hormone control has two-control actions: u_1 is represented by the injection of insulin in the bloodstream, and u_2 is represented by the amount of glucagon administered in the bloodstream. A simple switching logic with hysteresis is applied to choose which hormone is active at each moment. In the algorithm, when the blood glucose is under 0.8 g/l, the glucagon controller is switched on so that the glucose concentration increases to the desired value of 1 g/l; then, the blood glucose exits the safe range. The insulin controller is switched on, and the glucagon controller is deactivated.

Integral sliding mode Controller design

Control problem of blood glucose concentration in diabetes patients requires the tracking of the normal glucose level. For the first state of the system to track their reference value, we define the error and integral of error as follows:

$$e(t) = x_1(t) - x_r(t)\,; \quad (10)$$

$$e_I(t) = \int e(t)dt; \quad (11)$$

Now, consider a third order sliding surface that incorporate the tracking error:

$$S(t) = \ddot{e}(t) + \beta_1 \dot{e}(t) + \beta_2 e(t) + \alpha\, e_I(t); \quad (12)$$

$$S(t) = \ddot{x}_1(t) + \beta_1 \dot{x}_1(t) + \beta_2\big(x_1(t) - x_r(t)\big) + \alpha \int (x_1(t) - x_r(t))dt\,; \quad (13)$$

Differentiation of (13) with respect to time can be calculated by

$$\dot{S}(t) = \dddot{x}_1(t) + \beta_1\, \ddot{x}_1(t) + \beta_2\, \dot{x}_1(t) + \alpha\, x_1(\mathrm{t}); \quad (14)$$

The overall control law for blood glucose regulation of patient can be written as:

$$U_1 = \frac{1}{\varphi_1}\Big(g_1 + \beta_1\Big(-P_1\dot{x}_1(t) - \mathit{P2x1teS1i1t{-}P2S1x1ti1teS1i1t{+}Kgrm1t{+}P3g1t{+}\beta2{-}P1x1t{-}P2x1teS1I1t{+}Kgrm1t{+}P3g1t{+}\alpha\,(x1t{-}\,xr\,t){+}ksigns}\,; \quad (15)$$

$$U_2 = \frac{1}{\varphi_2}\Big(g_2 + \beta_1\big(-P_1\dot{x}_1(t) - P_2\dot{x}_1(t)e^{S_1 i_1(t)} - P_2 S_1 x_1(t) i_1(t) e^{S_1 i_1(t)} + K_{gr}\dot{m}_1(t) + P_3\dot{g}_1(t)\big) + \beta_2\big(-P_1 G x_1(t) - P_2 x_1(t)e^{S_1 i_1(t)} + K_{gr} m_1(t) + P_3 g_1(t)\big) + \alpha\,(x_1(t) - x_r(t)) + k\,sign(s)\Big); \quad (16)$$

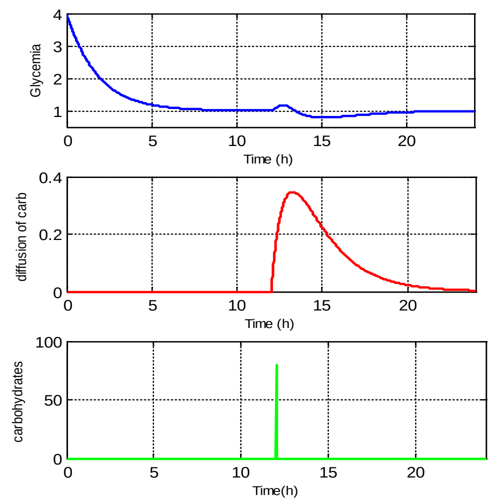

Fig.1: Concentration of blood glucose with hyperglycemia and external disturbance

III. Results and Discussion

In this section, we analyzed the behavior of proposed nonlinear controller under critical conditions, such as hypoglycemia (low blood glucose concentration) and hyperglycemia (high blood glucose concentration). Table .1 lists the value of the parameters have been used of the simulation in MATLAB.

The simulation in fig.1 shows a virtual patient confronted with hyperglycemia and external disturbance. Initially, the blood glucose concentration is around 4 g/l and the patient consumes 80 g of carbohydrates at 12:00 p.m . The blood sugar levels remain within the acceptable range of 0.9 to 1.20 g/L, avoiding critical periods of hyperglycemia or hypoglycemia. The blood sugar converges towards the target value of 1 g/L. The external disturbance does not impact the system's response, demonstrating the controller's robustness to such changes

The integral action integrated with the sliding mode technique results in a significant reduction in steady-state error.

Fig.2the control inputs Uins and Ug (insulin and glucagon injections) in the case of ISMC. This method exhibits unwanted chattering and fluctuations in the control inputs curve. It can be seen that the level of insulin administered into the body is at its maximum after the intake of carbohydrates, reaching a value of 13 U/min. To compensate for the high quantity of insulin and to avoid a hypoglycemic episode, the controller injects the glucagon. This approach ensures a safer management of blood glucose levels by preventing both hyperglycemia and hypoglycemia.

Table 1.

Parameters used during the simulation.

Parameter	Value	Units
P_1	0.003	min-1
P_2	0.0008	min-1
P_3	0.04	min-1
S_1	60	pmol/min
Kgr	0.04	mg/(dl/min)
Wg_1	0.2	min-1
Wg_2	0.02	min-1
Win_2	0.009	min-1
Win_1	0.006	min-1
Wr_2	0.02	min-1
Wr_1	0.008	min-1

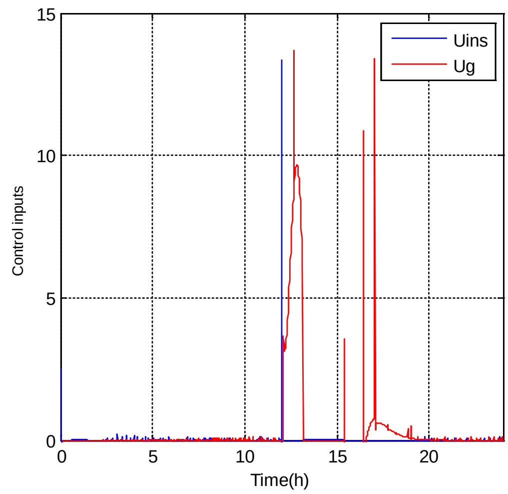

Fig 2: Control input (insulin and glucagon injected)

The effect of different initial conditions was simulated to check the robustness of the ISMC controller. Fig.3 presents the results obtained. Three different simulation scenarios were assumed. In the first scenario, the blood sugar level is initial X01= 0.3g/l; in the second scenario, it is X01= 0.4 g/l; and in the third scenario, it is X03=0.5 g/l. It can be noted that the blood glucose curves follow the same shape and converge to the desired value with the lowest error in beginning.

Fig.4 displays the control inputs by the controller for various initial conditions during a hypoglycemia episode. It is clear that the amount of administered glucagon varies based on the patient's initial conditions.

Fig.5 presents the tracking error in the presence of hypoglycemia with different initial conditions. Initially, the error is at maximum, indicating a significant difference between the real glucose level and the reference value. The error reduces to zero after injecting glucagon into the different patients using ISMC.

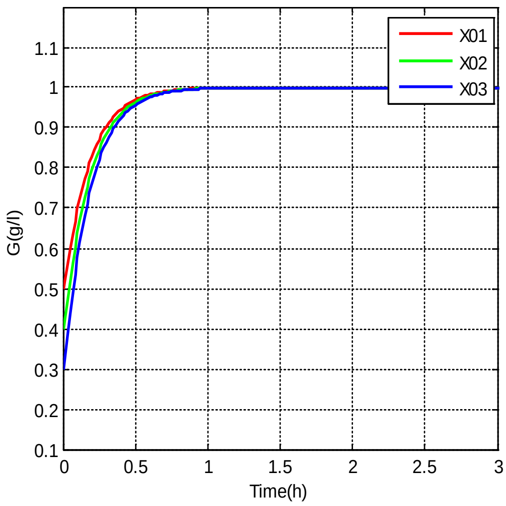

Fig.3: Concentration of blood glucose with different initial conditions.

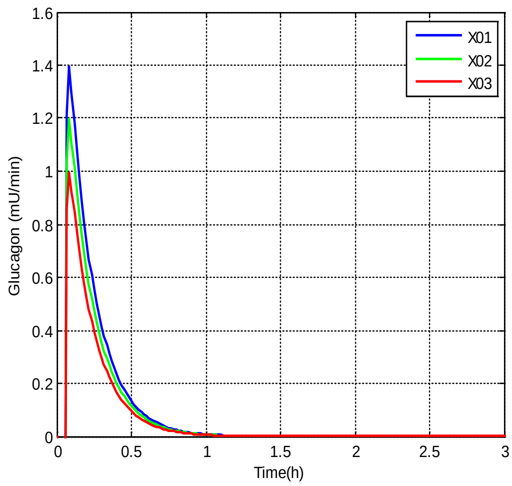

Fig.4: Control inputs by the ISMC

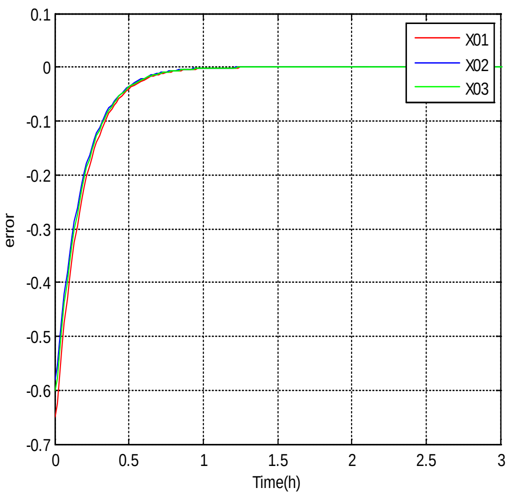

Fig.5: Tracking error under different initial conditions

Fig.6 shows the level of sugar in blood of three different patients with hypoglycemia, and Table.2 summarizes the parameters. It can be noted that all three patients' blood glucose levels were stabilized to reference value, validating the rejection of parameter uncertainty and robustness to parameter variations by the controller ISMC.

Fig.7 illustrates the control inputs (injected glucagon) of the three different patients using ISMC. It can be noted that the amount of administered glucagon is different for different patients depending on the parameters of patients in beginning.

Table 2.

Parameters used for three different patients.

Parameters	**Patient 1**	**Patient 2**	**Patient 3**
P_1	0.004	0.003	0.002
P_2	0.0009	0.0008	0.0007
P_3	0.05	0.04	0.03
S_1	70	60	50

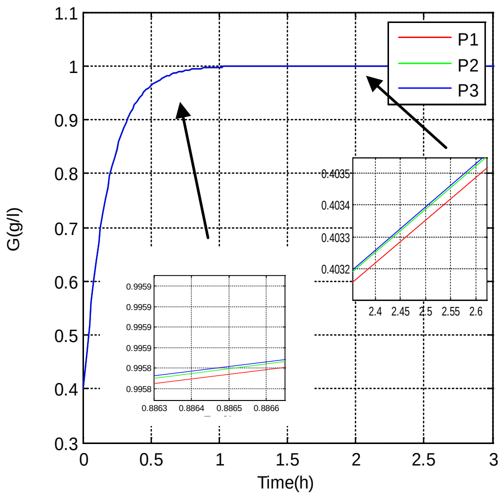

Fig.6: Concentration of blood glucose for three different conditions

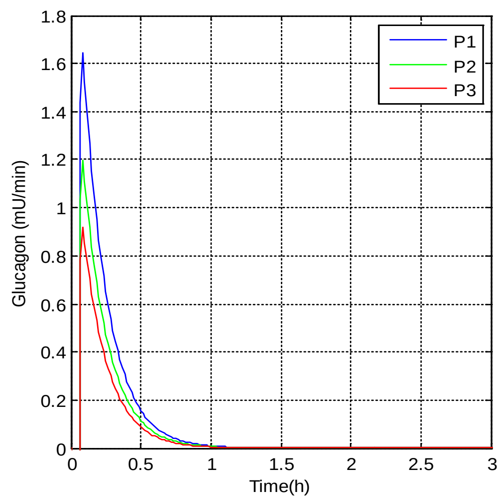

Fig.7: Control inputs for three different conditions

IV. CONCLUSION

Over the past few decades, the design of a robust controller has been an appropriate choice for the closed-loop of an artificial pancreas. This paper proposed the integral sliding mode with bihormonal control (ISMC) to regulate blood glucose. The dual hormone can potentially reduce insulininduced hypoglycemia's effects and provide additional blood glucose safety. The ISMC was also submitted to test the robustness property. Satisfactory results were observed from the simulation. In addition, the robustness of the proposed controller to parameter variations of different diabetic patients, external disturbances, and changes in the initial condition was confirmed

REFERENCES

[1] M. Dansa, V. H. P. Rodrigues, et T. R. Oliveira, « Blood glucose regulation in patients with type 1 diabetes by means of output-feedback sliding mode control », in *Control Applications for Biomedical Engineering Systems*, Elsevier, 2020, p. 25-54. doi: 10.1016/B978-0-12-817461-6.00002-0.

[2] M. Farman *et al.*, « A control of glucose level in insulin therapies for the development of artificial pancreas by AtanganaBaleanu derivative », *Alex. Eng. J.*, vol. 59, n° 4, p. 2639-2648, août 2020, doi: 10.1016/j.aej.2020.04.027.

[3] D. Majdpour*et al.*, « Fully Automated Artificial Pancreas for Adults With Type 1 Diabetes Using Multiple Hormones: Exploratory Experiments », *Can. J. Diabetes*, vol. 45, n° 8, p. 734-742, déc. 2021, doi: 10.1016/j.jcjd.2021.02.002.

[4] Sh. Asadiet V. Nekoukar, « Adaptive fuzzy integral sliding mode control of blood glucose level in patients with type 1 diabetes: In silico studies », *Math. Biosci.*, vol. 305, p. 122-132, nov. 2018, doi: 10.1016/j.mbs.2018.09.006.

[5] J. R. Castle *et al.*, « Novel Use of Glucagon in a Closed-Loop System for Prevention of Hypoglycemia in Type 1 Diabetes », *Diabetes Care*, vol. 33, n° 6, p. 1282-1287, juin 2010, doi: 10.2337/dc09-2254.

[6] F. H. El-Khatib, S. J. Russell, D. M. Nathan, R. G. Sutherlin, et E. R. Damiano, « A Bihormonal Closed-Loop Artificial Pancreas for Type 1 Diabetes », *Sci. Transl. Med.*, vol. 2, n° 27, avr. 2010, doi: 10.1126/scitranslmed.3000619.

[7] F. H. El-Khatib, J. Jiang, et E. R. Damiano, « A Feasibility Study of Bihormonal Closed-Loop Blood Glucose Control Using Dual Subcutaneous Infusion of Insulin and Glucagon in Ambulatory Diabetic Swine », *J. Diabetes Sci. Technol.*, vol. 3, n° 4, p. 789-803, juill. 2009, doi: 10.1177/193229680900300428.

[8] M. Reiter, F. Reiterer, et L. Del Re, « Bihormonal glucose control using a continuous insulin pump and a glucagon-pen », in *2016 European Control Conference (ECC)*, Aalborg, Denmark: IEEE, juin 2016, p. 2435-2440. doi: 10.1109/ECC.2016.7810655.

[9] S. J. Russell, F. H. El-Khatib, D. M. Nathan, K. L. Magyar, J. Jiang, et E. R. Damiano, « Blood Glucose Control in Type 1 Diabetes With a Bihormonal Bionic Endocrine Pancreas », Diabetes Care, vol. 35, no 11, p. 2148-2155, nov. 2012, doi: 10.2337/dc12-0071.

[10] N. Taleb et al., « Efficacy of single-hormone and dual-hormone artificial pancreas during continuous and interval exercise in adult patients with type 1 diabetes: randomised controlled crossover trial », Diabetologia, vol. 59, no 12, p. 2561-2571, déc. 2016, doi: 10.1007/s00125-016-4107-0.

[11] J. R. Castle et al., « Randomized Outpatient Trial of Single- and Dual-Hormone Closed-Loop Systems That Adapt to Exercise Using Wearable Sensors », Diabetes Care, vol. 41, no 7, p. 1471-1477, juill. 2018, doi: 10.2337/dc18-0228.

[12] B. S. Leon, A. Y. Alanis, E. N. Sanchez, F. Ornelas-Tellez, et E. Ruiz-Velazquez, « Inverse optimal neural control of blood glucose level for type 1 diabetes mellitus patients », J. Frankl. Inst., vol. 349, no 5, p. 1851-1870, juin 2012, doi: 10.1016/j.jfranklin.2012.02.011.

[13] F. Chee, A. V. Savkin, T. L. Fernando, et S. Nahavandi, « OptimalH^∞Insulin Injection Control for Blood Glucose Regulation in Diabetic Patients », IEEE Trans. Biomed. Eng., vol. 52, no 10, p. 1625-1631, oct. 2005, doi: 10.1109/TBME.2005.855727.

[14] H. M. Paiva, W. S. Keller, et L. G. R. Da Cunha, « Blood-Glucose Regulation Using Fractional-Order PID Control », J. Control Autom. Electr. Syst., vol. 31, no 1, p. 1-9, févr. 2020, doi: 10.1007/s40313-019-00552-0.

[15] T. B. Aradóttir et al., « Model predictive control for dose guidance in long acting insulin treatment of type 2 diabetes », IFAC J. Syst. Control, vol. 9, p. 100067, sept. 2019, doi: 10.1016/j.ifacsc.2019.100067.

[16] A. Abu-Rmileh, W. Garcia-Gabin, et D. Zambrano, « A robust sliding mode controller with internal model for closed-loop artificial pancreas », Med. Biol. Eng. Comput., vol. 48, no 12, p. 1191-1201, déc. 2010, doi: 10.1007/s11517-010-0665-3.

[17] M.-C. Pai, « Discrete-time output feedback quasi-sliding mode control for robust tracking and model following of uncertain systems », J. Frankl. Inst., vol. 351, no 5, p. 2623-2639, mai 2014, doi: 10.1016/j.jfranklin.2014.01.005.

[18] Y. Niuet D. W. C. Ho, « Design of Sliding Mode Control Subject to Packet Losses », IEEE Trans. Autom. Control, vol. 55, no 11, p. 2623-2628, nov. 2010, doi: 10.1109/TAC.2010.2069350.

[19] R. Pradhan et B. Subudhi, « Double Integral Sliding Mode MPPT Control of a Photovoltaic System », IEEE Trans. Control Syst. Technol., vol. 24, no 1, p. 285-292, janv. 2016, doi: 10.1109/TCST.2015.2420674.

[20] Y. Islam, I. Ahmad, M. Zubair, et K. Shahzad, « Double Integral sliding mode control of Leukemia Therapy », Biomed. Signal Process. Control, vol. 61, p. 102046, août 2020, doi: 10.1016/j.bspc.2020.102046.

[21] W. Boutayeb, M. E. N. Lamlili, A. Boutayeb, et M. Derouich, « Mathematical Modelling and Simulation of <i>β</i>-Cell Mass, Insulin and Glucose Dynamics: Effect of Genetic Predisposition to Diabetes », J. Biomed. Sci. Eng., vol. 07, no 06, p. 330-342, 2014, doi: 10.4236/jbise.2014.76035.

[22] C.-L. Chen et H.-W. Tsai, « Modeling the physiological glucose–insulin system on normal and diabetic subjects », Comput. Methods Programs Biomed., vol. 97, no 2, p. 130-140, févr. 2010, doi: 10.1016/j.cmpb.2009.06.005.

[23] P. S. Shabestari, S. Panahi, B. Hatef, S. Jafari, et J. C. Sprott, « A new chaotic model for glucose-insulin regulatory system », Chaos Solitons Fractals, vol. 112, p. 44-51, juill. 2018, doi: 10.1016/j.chaos.2018.04.029.

[24] I. B. Abbes, P.-Y. Richard, M.-A. Lefebvre, I. Guilhem, et J.-Y. Poirier, « A Closed-Loop Artificial Pancreas Using a Proportional Integral Derivative with Double Phase Lead Controller Based on a New Nonlinear Model of Glucose Metabolism », J. Diabetes Sci. Technol., vol. 7, no 3, p. 699-707, mai 2013, doi: 10.1177/193229681300700315.

[25] M. Saoussane, T. Mohammed, et C. Mesaoud, « Adaptive controller based an extended model of glucose-insulin-glucagon system for type 1 diabetes », Int. J. Model. Simul., vol. 43, no 3, p. 282-293, mai 2023, doi: 10.1080/02286203.2022.2068214.

Saoussane Mahour received Engineering and Master degree in Control Engineering in 2015 from Ecole Nationale Polytechnqiue (ENP) of Algiers, Algeria. She is actually a PhD student in Automatic Control in the same school. Her current research interests are control in biological system, Non Linear and Robust Control.

Mohamed Tadjine received her PhD degree in Control and Manufacturing Management from 'Institut National Polytechnique de Grenoble' (INPG), (France) in 1994. In 1997, he joined the Ecole Nationale Polytechnique where he is currently Professor in Control Engineering Department. His main research areas are: Non Linear and Robust Control, Observer Design, Fault Detection and Fault Tolerant Control, Application in healthcare and biological systems.

Messaoud Chakir received his PhD degree in Automatic & Control in 2017 from the Ecole Nationale Polytechnique. He is a lecturer-researcher interested in the main research areas of: Robotics, Fault Detection and Fault Tolerant Control, Optimal Control, Application in healthcare and biological systems.

Axisymmetric Heat Conduction in a Cracked Layer Subjected to Prescribed Temperatures

Zakaria Baka and Belkacem Kebli

Abstract—This paper presents an analysis of an axisymmetric heat conduction problem in a layer with circular heat sources on its external surfaces, maintaining constant temperatures. Additionally, the layer contains a circular crack along its middle plane, either internally or externally, leading to a mixed boundary value problem. In this study, dual integral equations are derived using Hankel's transform technique. In contrast to the conventional approach that relies on Fredholm's equations, these dual integral equations are directly reduced to an infinite set of simultaneous equations. The investigation subsequently provides closed-form expressions involving special functions for the thermal fields and heat flux intensity factor. Moreover, the solution for the case of a half-space medium is obtained as a limiting case of this study. The accuracy and validity of the present approach are also confirmed through comparison with numerical simulations. Sets of plots are provided to analyze the influence of the crack, surface radius of the applied temperatures, and the layer thickness on various physical quantities.

***Keywords*—Heat conduction, Cracked layer, Mixed boundary value problem, Dual integral equations, Heat flux intensity factor.**

NOMENCLATURE

a	Radius of the heated or cooled area, m.
a_n	Series coefficients.
A, B, C	Unknown functions.
A_{mn}	Matrix elements of the algebraic system.
b	Radius of the penny-shaped crack, m.
b_m	Vector elements of the right-hand side of the algebraic system.
E, K	Complete elliptic integrals of the second and first kinds.
h	Half thickness of the layer, m.
J_ν	Bessel function of the first kind of order ν.
k	Thermal conductivity, $\mathrm{W/(m\,K)}$.
K_T, K'_T	Heat flux intensity factors, $\mathrm{W/m^{3/2}}$.
q_r, q_z	Heat fluxes in the r- and z-directions, $\mathrm{W/m^2}$.
r, z	Radial and axial coordinates, m.
si	Sine integral function.
T	Temperature, K.
T_0	Constant temperature, K.
T_n, U_n	Chebyshev's polynomials of the first and second kinds of degree n.

Greek symbols

α_n	Series coefficients.
δ	Dirac delta function.
$\delta_{\ell m}$	Kronecker delta.
ρ, ζ	Dimensionless radial and axial coordinates.

Manuscript received September 25, 2023; revised December 17, 2024.

Z. Baka and B. Kebli are affiliated with the Laboratory of Green and Mechanical Development (LGMD), Department of Mechanical Engineering, Ecole Nationale Polytechnique (ENP), El-Harrach, 16200 Algiers, ALGERIA (e-mails: zakaria.baka@g.enp.edu.dz, belkacem.kebli@g.enp.edu.dz).

Digital Object Identifier (DOI): 10.53907/enpesj.v4i2.242

I. INTRODUCTION

The study of heat conduction phenomena in solids has significant practical importance in various engineering disciplines, including electronic equipment cooling, aerospace technology, and the nuclear industry. Moreover, the obtained solutions are crucial for determining thermal displacements and stresses in related thermoelastic problems. Several pertinent literature sources, such as [1–3], offer comprehensive insights into the mathematical modeling of heat conduction, providing valuable resources for further exploration of the subject matter. Over the past decades, mixed boundary value problems, where different conditions are applied to distinct regions of the same boundary, have garnered considerable attention in the field of heat conduction. The presence of singularities in these problems often complicates the derivation of solutions using traditional methods, posing significant challenges to researchers. Several researchers have made notable contributions to addressing these challenges. For instance, Dhaliwal [4, 5] investigated heat conduction problems in a slab and effectively reduced the resulting equations to Fredholm equations. He then obtained the solution by employing the successive approximation method. Beck [6] examined the case of a half-space body exposed to a uniform heat flux over a circular area and derived an exact series expression for temperatures. Mehta and Bose [7] studied the steady-state temperature field in a layer subjected to a constant flux over a circular area, presenting a series solution expressed in terms of the Gauss hypergeometric function. The steady-state heat conduction problem in a semi-infinite medium under radiation conditions is addressed by Gladwell et al. [8]. They transformed the cases into integro-differential equations and further simplified them into a set of simultaneous equations. Additionally, many authors have focused on studying thermal constriction resistance [9–13]. Cracked solids present specific challenges, prompting various investigations aimed at enhancing our understanding of heat conduction phenomena and the impact of cracks on the thermal behavior of solids. The majority of these studies have been conducted within the context of thermoelasticity [14–18]. Notably, Sih [19] was first determined that the temperature gradient or heat flux in the vicinity of the crack tip follows an inverse square-root singularity. Building upon this pioneering work, subsequent researchers have further explored this singularity behavior, employing diverse analytical and numerical methods [20–25]. With the progress of computer technology, numerical methods have experienced significant advancements. However, challenges related to mesh optimization, computation time, and accuracy persist. On the other hand, despite the difficulties involved in constructing mathematical models in theoretical research, analytical techniques continue to be extensively employed. These techniques provide valuable alternatives for investigating solutions in several fields, including heat conduction in cracked solids, and offer distinct advantages compared to numerical approaches. In this context, we aim to investigate the steady-state heat conduction in a cracked layer subjected to circular heat sources with constant temperatures. We consider two types of circular cracks, namely internal and external cracks. The two problems are reduced to a mixed boundary value problem, which we address by employing the Hankel transform technique. This enables us to derive dual integral equations. Using the Gegenbauer addition formula and several integral relations, we simplify these equations into an infinite set of simultaneous equations. Our analysis yields explicit expressions for temperature, heat fluxes, and the flux intensity factor. Additionally, we derive the solution for a semi-infinite medium without cracks as a limiting case. We also validate our results through a finite element simulation using ANSYS software. Selected results are presented graphically, providing insights into the behavior and characteristics of the heat conduction process in solids when cracks are present.

II. Formulation of the Problem

As Fig. 1 shows, the physical domain of interest is a layer with a thickness of $2h$, subjected to prescribed temperatures and containing either a penny-shaped crack or an external crack. The penny-shaped crack is assumed to be thermally insulated, whereas the external crack surfaces are maintained at the reference temperature, $T = 0$. An axisymmetric cylindrical coordinate system $(r,\, z)$ is adopted, such that the penny-shaped crack lies in the circular region $r \leq b$, positioned at a depth h from the external surface of the layer. In contrast, the external crack is situated in the opposite region ($r \geq b,\ z = h$). With regards to the thermal properties, the solid is considered homogeneous and isotropic, with a thermal conductivity denoted as k.

In the first case involving the presence of a penny-shaped crack within the layer, as depicted in Fig. 1(a), the temperatures within a circular region of radius a on both the lower and upper surfaces of the layer are assumed to remain constant at T_0 and $-T_0$, respectively. Conversely, in the second case, involving an external crack, the disc-shaped heat sources are both imposing an identical constant temperature T_0, as shown in Fig. 1(b). Additionally, the remaining surfaces in both cases are kept at the reference temperature ($T = 0$).

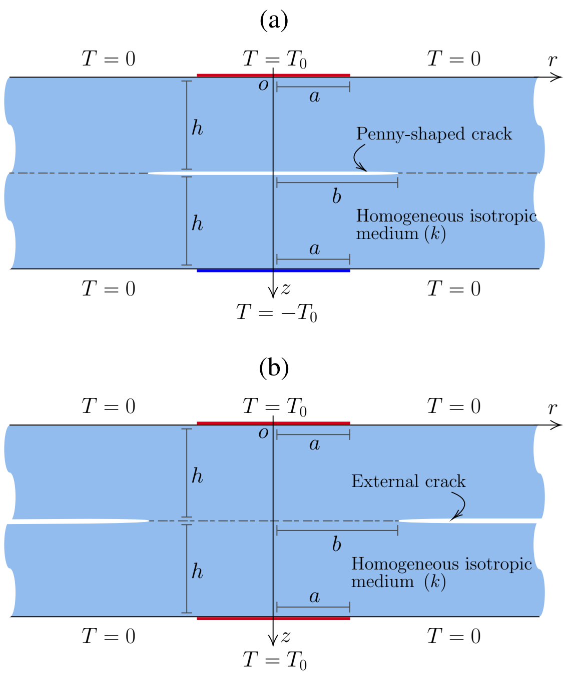

Fig. 1: A layer medium containing (a) an insulated penny-shaped crack; (b) an external crack.

Under the assumption of steady-state thermal loading, and with no heat generation assumed in the medium, the governing equation describing the temperature change T for the considered problems is given as

$$\nabla^2 T(r,z) = 0, \qquad \nabla^2 \equiv \frac{\partial^2}{\partial r^2} + \frac{1}{r}\frac{\partial}{\partial r} + \frac{\partial^2}{\partial z^2}, \tag{1}$$

where ∇^2 represents Laplace's operator expressed in the axisymmetric cylindrical coordinate system.

Since the first problem exhibits anti-symmetry and the second displays symmetry with respect to the plane $z = 0$, we can focus our investigation on the analysis of the half-layer $0 \leq z \leq h$ of the medium. Thus, both problems can be simplified into the single mixed boundary value problem depicted in Fig. 2.

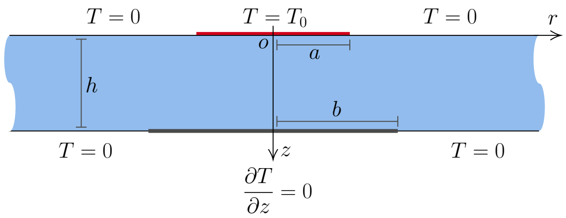

Fig. 2: Geometry of the considered mixed boundary value problem.

This heat conduction problem is governed by (1), which is subject to the following boundary conditions

$$T(r,0) = \begin{cases} T_0, & r \leq a, \\ 0, & r > a, \end{cases} \tag{2a}$$

$$\frac{\partial T}{\partial z}(r,h) = 0, \qquad r < b, \tag{2b}$$

$$T(r,h) = 0, \qquad r \geq b. \tag{2c}$$

Furthermore, the regularity conditions require the thermal fields to approach zero as r tends toward infinity ($r \to \infty$).

III. Analytical solution

This section presents the solution methodology for the mixed boundary value problem illustrated in Fig. 2. The proposed solution scheme involves the derivation of integral dual equations, which are subsequently reduced to an infinite system of algebraic equations. Explicit analytical expressions for the thermal fields and heat flux intensity factor can then be derived based on the solution of the algebraic equations.

A. Derivation of the dual integral equations

To effectively solve the considered problem, it is convenient to use the Hankel integral transform technique, which is particularly well-suited for problems with axisymmetric cylindrical configurations. Specifically, the direct and inverse zeroth-order Hankel transforms of a given function, denoted by f, with respect to the radial variable r, are defined by [26, Eqs. (7.2.8) and (7.2.10)]

$$f_H(\xi) = \int_0^\infty r\, f(r)\, J_0(\xi\, r)\, \mathrm{d}r, \tag{3a}$$

$$f(r) = \int_0^\infty \xi\, f_H(\xi)\, J_0(r\, \xi)\, \mathrm{d}\xi, \tag{3b}$$

respectively, where J_0 stands for the zeroth-order Bessel function of the first kind, and ξ represents the transformed variable. Accordingly, by applying the Hankel transform to the Laplace equation (1), yields

$$\frac{\partial^2 T_H}{\partial z^2}(\xi, z) - \xi^2\, T_H(\xi, z) = 0, \tag{4}$$

which is a second-order ordinary differential equation within T_H represents the Hankel transform counterpart of the temperature T. Considering the boundary condition at infinity, the general solution of (4) can be expressed in the following form

$$T_H(\xi, z) = \frac{\cosh(z\,\xi)\, A(\xi) + \sinh(z\,\xi)\, B(\xi)}{\xi}, \tag{5}$$

where A and B represent unknown functions in terms of ξ to be determined through the boundary conditions.

Applying the Hankel transform to the boundary condition (2a), gives

$$T_H(\xi, 0) = T_0 \int_0^a r\, J_0(\xi\, r)\, \mathrm{d}r. \tag{6}$$

Thus, using the expression for T_H given by (5) and the relation specified in [27, Eq. (5.56 2)], which states that $\int x\, J_0(x)\, \mathrm{d}x = x\, J_1(x)$, we find

$$A(\xi) = a\, T_0\, J_1(a\, \xi). \tag{7}$$

Substituting (7) in (5), one obtains

$$T_H(\xi, z) = \frac{\sinh(z\,\xi)\, B(\xi) + a\, T_0\, \cosh(z\,\xi)\, J_1(a\,\xi)}{\xi}. \tag{8}$$

Consequently, the number of unknown functions is reduced.

Thereafter, we can perform the Hankel inversion transform (3b) on (8), yielding the following expression for the temperature T

$$T = \int_0^\infty \left[\sinh(z\,\xi)\, B(\xi) + a\, T_0\, \cosh(z\,\xi)\, J_1(a\,\xi)\right] J_0(r\,\xi)\, \mathrm{d}\xi. \tag{9}$$

To simplify the notation used in this paper, we have not explicitly mentioned the dependence of the functions on the variables (r, z) throughout the text. Nevertheless, this dependence should be understood implicitly.

Continuing with the derivation, we can obtain the temperature gradient by differentiating (9) with respect to z, giving us the expression below

$$\frac{\partial T}{\partial z} = \int_0^\infty \xi \left[\cosh(z\,\xi) B(\xi) + a\, T_0 \sinh(z\,\xi) J_1(a\,\xi)\right] J_0(r\,\xi)\, \mathrm{d}\xi. \tag{10}$$

Inserting (10) and (9) into the respective boundary conditions (2b) and (2c), yields

$$\begin{aligned} &\int_0^\infty \xi \left[\cosh(h\,\xi)\, B(\xi) + a\, T_0\, \sinh(h\,\xi) \right. \\ &\qquad \left. \times J_1(a\,\xi)\right] J_0(r\,\xi)\, \mathrm{d}\xi = 0, \end{aligned} \qquad r < b, \tag{11a}$$

$$\begin{aligned} &\int_0^\infty \left[\sinh(h\,\xi)\, B(\xi) + a\, T_0\, \cosh(h\,\xi) \right. \\ &\qquad \left. \times J_1(a\,\xi)\right] J_0(r\,\xi)\, \mathrm{d}\xi = 0, \end{aligned} \qquad r \geq b. \tag{11b}$$

To simplify the latter integral equations, we introduce the function C as follows

$$C(\xi) = \sinh(h\,\xi)\, B(\xi) + a\, T_0\, \cosh(h\,\xi)\, J_1(a\,\xi). \tag{12}$$

Then, B can be expressed in terms of C as

$$B(\xi) = \operatorname{csch}(h\,\xi)\, C(\xi) - a\, T_0\, \coth(h\,\xi)\, J_1(a\,\xi), \tag{13}$$

where $\operatorname{csch}(h\,\xi) = 1/\sinh(h\,\xi)$. Replacing B in (11) with its expression given by (13), and after some algebraic manipulation, we finally get

$$\begin{aligned} &\int_0^\infty \xi \coth(h\,\xi)\, C(\xi)\, J_0(r\,\xi)\, \mathrm{d}\xi \\ &\quad = a\, T_0 \int_0^\infty \xi \operatorname{csch}(h\,\xi)\, J_0(r\,\xi)\, J_1(a\,\xi)\, \mathrm{d}\xi, \end{aligned} \qquad r < b, \tag{14a}$$

$$\int_0^\infty C(\xi)\, J_0(r\,\xi)\, \mathrm{d}\xi = 0, \qquad r \geq b. \tag{14b}$$

Equations (14a) and (14b) form dual integral equations for determining the unknown function C.

B. Solution of the dual integral equations

Our task turns to determine the unknown function C through the system of dual integral equations (14). To solve such kinds of integral equations with Bessel function kernels, several approaches can be employed, including those used by Sneddon [28, 29], Duffy [30], Sakamoto [31], Kebli and Madani [32]. Among these approaches, the one presented in [31] has the advantage of reducing the system of triple integral equations directly into the solution of an infinite system of algebraic equations. This approach, along with similar methods, have been increasingly utilized in recent studies to solve diverse mixed boundary value problems [33–37], indicating the broad range of applicability of such techniques.

Therefore, in this work, we adopt the solution approach outlined by Sakamoto [31] and use the following dual integral formula [37, Eq. (A4)]

$$\int_0^\infty N_n(\xi)\, J_0(r\,\xi)\, \mathrm{d}\xi = \begin{cases} \dfrac{4\sqrt{b^2 - r^2}}{\pi\, b^2\, r}\, U_{2\,n+1}(r/b), & r < b, \\ 0, & r > b, \end{cases} \tag{15}$$

where $n = 0, 1, 2, \ldots$, $N_n(\xi) = \xi\,[M_n(\xi) - M_{n+1}(\xi)]$ and $M_n(\xi) = J_{n+1/2}(b\,\xi/2)\,J_{-(n+1/2)}(b\,\xi/2)$. Additionally, U_n is the Chebyshev polynomials of the second kind of degree n. They are defined by the relation $U_n(x) = \sin[(n+1)\arccos x]/\sin[\arccos x]$ [27, Eq. (8.940 2)].

Accordingly, we express the function C as a series expansion involving Bessel functions in the following form

$$C(\xi) = a\,T_0 \sum_{n=0}^{\infty} a_n\,N_n(\xi), \tag{16}$$

where a_n are unknown coefficients to be determined later. By adopting this expression, we can readily deduce that (14b) is automatically satisfied, as indicated by (15). Then, inserting (16) into (14a), yields

$$\begin{aligned}\sum_{n=0}^{\infty} a_n \int_0^{\infty} \xi \coth(h\,\xi)\,N_n(\xi)\,J_0(r\,\xi)\,\mathrm{d}\xi \\ = \int_0^{\infty} \xi \,\mathrm{csch}(h\,\xi)\,J_0(r\,\xi)\,J_1(a\,\xi)\,\mathrm{d}\xi,\end{aligned} \qquad r < b. \tag{17}$$

In order to eliminate the radial variable r, we can utilize the Gegenbauer addition formula below [27, Eq. (8.531 3)]

$$J_0(r\,\xi) = \sum_{m=0}^{\infty} (2-\delta_{0m})\,X_m(\xi)\,\cos(m\,\phi), \qquad r < b, \tag{18}$$

where $X_m(\xi) = J_m^2(b\,\xi/2)$, $\phi = 2\arcsin(r/b)$ and $\delta_{\ell m}$ stands for the Kronecker delta, which is defined by $\delta_{\ell m} = \begin{cases} 1, & \ell = m, \\ 0, & \ell \neq m. \end{cases}$ By substituting (18) into (17), rearranging the terms, and interchanging the order of integration and summation, we get

$$\begin{aligned}\sum_{m=0}^{\infty}(2-\delta_{0m})\cos(m\,\phi)\sum_{n=0}^{\infty} a_n \int_0^{\infty} \xi\coth(h\,\xi) N_n(\xi) X_m(\xi)\,\mathrm{d}\xi \\ = \sum_{m=0}^{\infty}(2-\delta_{0m})\cos(m\,\phi)\int_0^{\infty} \xi\,\mathrm{csch}(h\,\xi)\,X_m(\xi)\,J_1(a\,\xi)\,\mathrm{d}\xi.\end{aligned} \tag{19}$$

Thereafter, by matching the coefficients of $\cos(m\,\phi)$ on both sides of (19), we obtain the following infinite set of simultaneous equations

$$\begin{aligned}\sum_{n=0}^{\infty} a_n \int_0^{\infty} \xi \coth(h\,\xi)\,N_n(\xi)\,X_m(\xi)\,\mathrm{d}\xi \\ = \int_0^{\infty} \xi\,\mathrm{csch}(h\,\xi)\,X_m(\xi)\,J_1(a\,\xi)\,\mathrm{d}\xi,\end{aligned} \tag{20}$$

where $m = 0, 1, 2, \ldots$

In order to get a symmetric coefficient matrix and accelerate the convergence of the previous algebraic system, we subtract the $(m+2)$th equations from the mth equations in (20). As a result, we arrive at an algebraic system for determining a_n, expressed in matrix form as follows

$$\sum_{n=0}^{\infty} A_{mn}\,a_n = b_m, \qquad m = 0, 1, 2, \ldots \tag{21}$$

where $A_{mn} = \int_0^{\infty} \coth(h\,\xi)\,N_n(\xi)\,Y_m(\xi)\,\mathrm{d}\xi$, $Y_m(\xi) = \xi\,[X_m(\xi) - X_{m+2}(\xi)]$ and $b_m = \int_0^{\infty} \mathrm{csch}(h\,\xi)\,Y_m(\xi)\,J_1(a\,\xi)\,\mathrm{d}\xi$.

Consequently, we have effectively reduced the heat conduction problems under consideration to solving an infinite set of simultaneous equations defined by (21). Notably, this system depends only on the geometric parameters a, b and h.

C. Temperature and heat flux expressions

We now proceed to derive the expressions for temperature and heat fluxes in terms of the series coefficients a_n. By considering (13) and (16), we can explicitly express the temperature field described by equation (9) as follows

$$\begin{aligned}T = a\,T_0 \Big\{ \int_0^{\infty} \mathrm{csch}(h\,\xi)\sinh((h-z)\,\xi) J_0(r\,\xi)\,J_1(a\,\xi)\,\mathrm{d}\xi \\ + \sum_{n=0}^{\infty} a_n \int_0^{\infty} \mathrm{csch}(h\,\xi)\,\sinh(z\,\xi)\,N_n(\xi)\,J_0(r\,\xi)\,\mathrm{d}\xi \Big\}.\end{aligned} \tag{22}$$

Furthermore, following the Fourier law of heat conduction, the heat flux in the r- and z-directions can be expressed as $q_r = -k\,\partial T/\partial r$ and $q_z = -k\,\partial T/\partial z$, respectively. Consequently, their expressions in terms of a_n can be obtained. Formally,

$$\begin{aligned}q_r = a\,k\,T_0 \Big\{ \int_0^{\infty} \xi\,\mathrm{csch}(h\,\xi)\,\sinh((h-z)\,\xi)\,J_1(a\,\xi) J_1(r\,\xi)\,\mathrm{d}\xi \\ + \sum_{n=0}^{\infty} a_n \int_0^{\infty} \xi\,\mathrm{csch}(h\,\xi)\,\sinh(z\,\xi)\,N_n(\xi)\,J_1(r\,\xi)\,\mathrm{d}\xi \Big\},\end{aligned} \tag{23a}$$

$$\begin{aligned}q_z = a\,k\,T_0 \Big\{ \int_0^{\infty} \xi\,\mathrm{csch}(h\,\xi)\cosh((h-z)\,\xi)\,J_0(r\,\xi) J_1(a\,\xi)\,\mathrm{d}\xi \\ - \sum_{n=0}^{\infty} a_n \int_0^{\infty} \xi\,\mathrm{csch}(h\,\xi)\cosh(z\,\xi)\,N_n(\xi)\,J_0(r\,\xi)\,\mathrm{d}\xi \Big\}.\end{aligned} \tag{23b}$$

The planes $z = 0$ and $z = h$ are of particular interest. When considering the case where $z = 0$, the previously mentioned heat flux expressions can be rewritten as

$$q_r(r, 0) = a\,k\,T_0 \int_0^{\infty} \xi\,J_1(a\,\xi)\,J_1(r\,\xi)\,\mathrm{d}\xi, \tag{24a}$$

$$\begin{aligned}q_z(r, 0) = a\,k\,T_0 \Big\{ \int_0^{\infty} \xi \coth(h\,\xi)\,J_0(r\,\xi)\,J_1(a\,\xi)\,\mathrm{d}\xi \\ - \sum_{n=0}^{\infty} a_n \int_0^{\infty} \xi\,\mathrm{csch}(h\,\xi)\,N_n(\xi)\,J_0(r\,\xi)\,\mathrm{d}\xi \Big\}.\end{aligned} \tag{24b}$$

From the identity given by [27, Eq. (6.512 8)], we have

$$\int_0^{\infty} \xi\,J_1(a\,\xi)\,J_1(r\,\xi)\,\mathrm{d}\xi = \delta(r-a)/a, \tag{25}$$

where δ denotes the Dirac delta function, defined by

$$\delta(x) = \begin{cases} \infty, & x = 0, \\ 0, & x \neq 0. \end{cases} \tag{26}$$

Here, it is worth mentioning that the Dirac delta function is frequently employed in problems involving concentrated loads or local sources [3, ch. 9].

By making use of (25) and (A.6), we can finally express the heat fluxes at the plane $z = 0$ as follows

$$q_r(r, 0) = k\,T_0\,\delta(r-a), \tag{27a}$$

$$\begin{aligned}q_z(r, 0) = a\,k\,T_0 \Big\{ \int_0^{\infty} \xi\,\big[\coth(h\,\xi) - 1\big]\,J_0(r\,\xi)\,J_1(a\,\xi)\,\mathrm{d}\xi \\ - \frac{1}{\pi\,a}\left[\frac{E\left(\frac{2\sqrt{a\,r}}{r+a}\right)}{r-a} - \frac{K\left(\frac{2\sqrt{a\,r}}{r+a}\right)}{r+a} \right] \\ - \sum_{n=0}^{\infty} a_n \int_0^{\infty} \xi\,\mathrm{csch}(h\,\xi)\,N_n(\xi)\,J_0(r\,\xi)\,\mathrm{d}\xi \Big\},\end{aligned} \tag{27b}$$

where K and E represent the complete elliptic integrals of the first and second kinds, respectively. They are given as [27, p. 396]

$$K(y) = \int_0^{\pi/2} \frac{\mathrm{d}x}{\sqrt{1-y^2\,\sin^2 x}}, \tag{28a}$$
$$E(y) = \int_0^{\pi/2} \sqrt{1-y^2\,\sin^2 x}\,\mathrm{d}x. \tag{28b}$$

Regarding the plane $z = h$, by setting $z = h$ in (22) and (23), we get

$$T(r,h) = a\,T_0 \sum_{n=0}^{\infty} a_n \int_0^{\infty} N_n(\xi)\,J_0(r\,\xi)\,\mathrm{d}\xi, \tag{29a}$$
$$q_r(r,h) = a\,k\,T_0 \sum_{n=0}^{\infty} a_n \int_0^{\infty} \xi\,N_n(\xi)\,J_1(r\,\xi)\,\mathrm{d}\xi, \tag{29b}$$
$$\begin{aligned} q_z(r,h) = {}& a\,k\,T_0 \left\{ \int_0^{\infty} \xi\,\mathrm{csch}(h\,\xi) J_0(r\,\xi) J_1(a\,\xi)\,\mathrm{d}\xi \right. \\ & \left. - \sum_{n=0}^{\infty} a_n \int_0^{\infty} \xi\,\coth(h\,\xi)\,N_n(\xi)\,J_0(r\,\xi)\,\mathrm{d}\xi \right\}. \end{aligned} \tag{29c}$$

With the help of (15), (29a) is further simplified to

$$T(r,h) = \frac{4\,a\,T_0\,\sqrt{b^2-r^2}\,H(b-r)}{\pi\,b^2\,r} \sum_{n=0}^{\infty} a_n\,U_{2\,n+1}(r/b), \tag{30}$$

wherein H denotes the Heaviside step function defined by $H(x) = \begin{cases} 0, & x \le 0, \\ 1, & x > 0. \end{cases}$

As for the heat fluxes, by virtue of (A.16) and (A.28), we obtain the following expressions

$$\begin{aligned} q_r(r,h) = {}& -\frac{4\,a\,k\,T_0\,H(b-r)}{\pi\,b^2\,r^2\,\sqrt{b^2-r^2}} \sum_{n=0}^{\infty} a_n \big\{ 2\,(n+1)\,b\,r\,U_{2\,n}(r/b) \\ & - \left[(2\,n+1)\,r^2 + b^2\right] U_{2\,n+1}(r/b) \big\}, \end{aligned} \tag{31a}$$
$$\begin{aligned} q_z(r,h) = {}& a\,k\,T_0\,H(r-b) \\ & \times \left\{ \int_0^{\infty} \xi\,\mathrm{csch}(h\,\xi)\,J_0(r\,\xi)\,J_1(a\,\xi)\,\mathrm{d}\xi - \sum_{n=0}^{\infty} a_n \right. \\ & \times \left[\int_0^{\infty} \left(\xi\,\coth(h\,\xi)\,N_n(\xi) + \frac{8\,(n+1)\cos(b\,\xi)}{\pi\,b^2} \right) \right. \\ & \left. \left. \times J_0(r\,\xi)\,\mathrm{d}\xi - \frac{8\,(n+1)}{\pi\,b^2\sqrt{r^2-b^2}} \right] \right\}. \end{aligned} \tag{31b}$$

In view of (31), it can be observed that q_r and q_z are proportional to the inverse square-roots $1/\sqrt{b-r}$ and $1/\sqrt{r-b}$, respectively. This indicates that the heat fluxes exhibit the usual square-root singularity in the vicinity of the crack tip b [19–22, 38].

D. *The special case of a semi-infinite medium ($h \to \infty$)*

As h approaches infinity, this limiting case corresponds to a half-space medium where a circular heat source imposes a uniform temperature, while the rest of the surface is kept at a reference temperature. In this case, the vector elements b_m on the right-hand side of the algebraic system (21) become zero, owing to the limit $\lim_{h\to\infty} \mathrm{csch}(h\,\xi) = 0$. As a result, the algebraic system reduces to the following form

$$\sum_{n=0}^{\infty} A_{mn}\,a_n = 0, \qquad m = 0, 1, 2, \ldots \tag{32}$$

leading to a trivial solution ($a_n = 0$). Additionally, we have $\lim_{h\to\infty} \sinh((h-z)\,\xi)\,\mathrm{csch}(h\,\xi) = \mathrm{e}^{-z\,\xi}$. This readily simplifies the expressions for the temperature and heat fluxes to

$$T = a\,T_0 \int_0^{\infty} \mathrm{e}^{-z\,\xi}\,J_0(r\,\xi)\,J_1(a\,\xi)\,\mathrm{d}\xi, \tag{33a}$$
$$q_r = a\,k\,T_0 \int_0^{\infty} \xi\,\mathrm{e}^{-z\,\xi}\,J_1(a\,\xi)\,J_1(r\,\xi)\,\mathrm{d}\xi, \tag{33b}$$
$$q_z = a\,k\,T_0 \int_0^{\infty} \xi\,\mathrm{e}^{-z\,\xi}\,J_0(r\,\xi)\,J_1(a\,\xi)\,\mathrm{d}\xi. \tag{33c}$$

These expressions are identical to the exact solution derived in Appendix B.

E. *Heat flux intensity factor*

As outlined in subsection II.C on page 33, the heat fluxes near the crack tip exhibit a square-root singularity. To quantify the strength of this singularity, a heat flux intensity factor is introduced in an analogous way to the stress intensity factor. The latter plays a crucial role in understanding mechanical and thermal stresses and crack behavior. The heat flux component perpendicular to the crack, in our case, q_z, is more directly related to crack tip behavior and the generation of thermal stresses. Therefore, the heat flux intensity factor, denoted as K_T, pertains to this component, and its definition is given by [38, Eq. (2.3)]

$$K_T = \lim_{r\to b^+} \sqrt{2\,(r-b)}\,q_z(r,h). \tag{34}$$

Upon substitution of the heat flux expression provided by (31b) into the aforementioned equation leads to

$$\begin{aligned} K_T = {}& a\,k\,T_0 \lim_{r\to b^+} \sqrt{2\,(r-b)} \left\{ \int_0^{\infty} \xi\,\mathrm{csch}(h\,\xi) J_0(r\,\xi) J_1(a\,\xi)\mathrm{d}\xi \right. \\ & - \sum_{n=0}^{\infty} a_n \left[\int_0^{\infty} \left(\xi\,\coth(h\,\xi)\,N_n(\xi) \right. \right. \\ & \left. \left. \left. + \frac{8\,(n+1)\cos(b\,\xi)}{\pi\,b^2} \right) J_0(r\,\xi)\,\mathrm{d}\xi - \frac{8\,(n+1)}{\pi\,b^2\sqrt{r^2-b^2}} \right] \right\}. \end{aligned} \tag{35}$$

Within this equation, only the last term is singular. Consequently, this equation readily reduces to

$$K_T = \frac{8\,a\,k\,T_0}{\pi\,b^2\,\sqrt{b}} \sum_{n=0}^{\infty} (n+1)\,a_n. \tag{36}$$

It is worth noting that the heat flux component parallel to the crack is usually not included in standard heat flux intensity factor calculations. Nevertheless, for the sake of completeness, we also derive the heat flux intensity factor related to this component.

Let us denote the heat flux intensity factor associated with q_r as K_T'. Following a similar form as in (34), we can express K_T' as

$$K_T' = \lim_{r\to b^-} \sqrt{2\,(b-r)}\,q_r(r,h). \tag{37}$$

Inserting (31a) into (37), yields

$$\begin{aligned} K_T' = {}& -\frac{4\sqrt{2}\,a\,k\,T_0}{\pi\,b^2} \lim_{r\to b^-} \sum_{n=0}^{\infty} \frac{a_n}{r^2\,\sqrt{r+b}} \big\{ 2\,(n+1)\,b\,r \\ & \times U_{2\,n}(r/b) - \left[(2\,n+1)\,r^2 + b^2\right] U_{2\,n+1}(r/b) \big\}. \end{aligned} \tag{38}$$

We then proceed with the evaluation of the limit using the trigonometric forms of the Chebyshev polynomials U_n and L'Hôpital's rule. We have

$$\lim_{r\to b^-} U_n(r/b) = \lim_{r\to b^-} \frac{\sin\left[(n+1)\arccos(r/b)\right]}{\sin\left[\arccos(r/b)\right]} \tag{39a}$$

$$= \lim_{r\to b^-} \frac{\dfrac{\mathrm{d}}{\mathrm{d}r}\sin\left[(n+1)\arccos(r/b)\right]}{\dfrac{\mathrm{d}}{\mathrm{d}r}\sin\left[\arccos(r/b)\right]}. \tag{39b}$$

Performing the differentiation of (39b) with respect to r, we get

$$\lim_{r\to b^-} U_n(r/b) = \lim_{r\to b^-} \frac{(n+1)\,b\,\cos\left[(n+1)\arccos(r/b)\right]}{r}. \tag{40}$$

Thus, $\lim_{r\to b^-} U_n(r/b) = n+1$. Accordingly, upon evaluating the limit in (38), we obtain

$$K_T' = \frac{8\,a\,k\,T_0}{\pi\,b^2\sqrt{b}} \sum_{n=0}^{\infty} (n+1)\,a_n. \tag{41}$$

Remarkably, it has been found that the expressions for heat flux intensity factors K_T and K_T' are identical ($K_T = K_T'$). Consequently, our focus in the following discussion will only be on K_T.

F. *Dimensionless expressions*

Dealing with dimensionless quantities is often convenient. We can achieve this by introducing a variable change $\eta = b\,\xi$. Additionally, the dimensionless parameters $\bar{a} = a/b$, $\bar{h} = h/b$, $\rho = r/b$ and $\zeta = z/b$ are also used. We then express the matrix elements A_{mn} and vector elements b_m as $A_{mn} = \bar{A}_{mn}/b^3$ and $\bar{b}_m = b_m/b^2$. Here, $\bar{A}_{mn}$ and $\bar{b}_m$ are given by

$$\bar{A}_{mn} = \int_0^\infty \coth(\bar{h}\,\eta)\,\bar{N}_n(\eta)\,\bar{Y}_m(\eta)\,\mathrm{d}\eta, \tag{42a}$$

$$\bar{b}_m = \int_0^\infty \operatorname{csch}(\bar{h}\,\eta)\,\bar{Y}_m(\eta)\,J_1(\bar{a}\,\eta)\,\mathrm{d}\eta, \tag{42b}$$

where $\bar{N}_n(\eta) = b\,N_n(\eta/b)$ and $\bar{Y}_m(\eta) = b\,Y_m(\eta/b)$.

Therefore, by considering $\alpha_n = a_n/b$, the algebraic system (21) can be transformed into the following dimensionless form

$$\sum_{n=0}^{\infty} \bar{A}_{mn}\,\alpha_n = \bar{b}_m, \qquad m = 0, 1, 2, \ldots \tag{43}$$

As for the dimensionless temperature, fluxes, and heat flux intensity factor, we define them as follows: $\bar{T} = T/T_0$, $\bar{q}_r = b\,q_r/(k\,T_0)$, $\bar{q}_z = b\,q_z/(k\,T_0)$, and $\bar{K}_T = \sqrt{b}\,K_T/(k\,T_0)$. By using these quantities and the previously introduced dimensionless parameters, we can transform the expressions (22), (23), (27), (30), (31) and (36) that represent the thermal fields and heat flux intensity factor into their dimensionless forms.

The dimensionless expressions for temperature are obtained as follows

$$\begin{aligned} &\bar{T}(\rho,\zeta) \\ &= \bar{a}\left\{\int_0^\infty \operatorname{csch}(\bar{h}\,\eta)\sinh((\bar{h}-\zeta)\,\eta)\,J_0(\rho\,\eta)\,J_1(\bar{a}\,\eta)\,\mathrm{d}\eta \right. \\ &\quad \left. + \sum_{n=0}^{\infty}\alpha_n \int_0^\infty \operatorname{csch}(\bar{h}\,\eta)\sinh(\zeta\,\eta)\,\bar{N}_n(\eta)\,J_0(\rho\,\eta)\,\mathrm{d}\eta\right\}, \end{aligned} \tag{44a}$$

$$\bar{T}(\rho,\bar{h}) = \frac{4\,\bar{a}\sqrt{1-\rho^2}\,H(1-\rho)}{\pi\,\rho}\sum_{n=0}^{\infty}\alpha_n\,U_{2\,n+1}(\rho). \tag{44b}$$

The dimensionless expressions for the heat flux in the radial direction can be expressed as

$$\begin{aligned} &\bar{q}_r(\rho,\zeta) \\ &= \bar{a}\left\{\int_0^\infty \eta\operatorname{csch}(\bar{h}\,\eta)\sinh((\bar{h}-\zeta)\,\eta)\,J_1(\bar{a}\,\eta)\,J_1(\rho\,\eta)\,\mathrm{d}\eta \right. \\ &\quad \left. + \sum_{n=0}^{\infty}\alpha_n \int_0^\infty \eta\operatorname{csch}(\bar{h}\,\eta)\sinh(\zeta\,\eta)\,\bar{N}_n(\eta)\,J_1(\rho\,\eta)\,\mathrm{d}\eta\right\}, \end{aligned} \tag{45a}$$

$$\bar{q}_r(\rho,0) = \delta(\rho-\bar{a}), \tag{45b}$$

$$\begin{aligned} \bar{q}_r(\rho,\bar{h}) = &-\frac{4\,\bar{a}\,H(1-\rho)}{\pi\,\rho^2\sqrt{1-\rho^2}}\sum_{n=0}^{\infty}\alpha_n\big\{2\,(n+1)\,\rho\,U_{2\,n}(\rho) \\ &-\left[(2\,n+1)\,\rho^2+1\right]U_{2\,n+1}(\rho)\big\}. \end{aligned} \tag{45c}$$

Regarding the heat flux in the axial direction, the dimensionless expressions are given by

$$\begin{aligned} &\bar{q}_z(\rho,\zeta) \\ &= \bar{a}\left\{\int_0^\infty \eta\operatorname{csch}(\bar{h}\,\eta)\cosh((\bar{h}-\zeta)\,\eta)\,J_0(\rho\,\eta)\,J_1(\bar{a}\,\eta)\,\mathrm{d}\eta \right. \\ &\quad \left. - \sum_{n=0}^{\infty}\alpha_n \int_0^\infty \eta\operatorname{csch}(\bar{h}\,\eta)\cosh(\zeta\,\eta)\,\bar{N}_n(\eta)\,J_0(\rho\,\eta)\,\mathrm{d}\eta\right\}, \end{aligned} \tag{46a}$$

$$\begin{aligned} \bar{q}_z(\rho,0) = \bar{a}&\left\{\int_0^\infty \eta\left[\coth(\bar{h}\,\eta)-1\right]J_0(\rho\,\eta)\,J_1(\bar{a}\,\eta)\,\mathrm{d}\eta \right. \\ &- \frac{1}{\pi\,\bar{a}}\left[\frac{E\left(\dfrac{2\sqrt{\bar{a}\,\rho}}{\rho+\bar{a}}\right)}{\rho-\bar{a}} - \frac{K\left(\dfrac{2\sqrt{\bar{a}\,\rho}}{\rho+\bar{a}}\right)}{\rho+\bar{a}}\right] \\ &\left. - \sum_{n=0}^{\infty}\alpha_n\int_0^\infty \eta\operatorname{csch}(\bar{h}\,\eta)\,\bar{N}_n(\eta)\,J_0(\rho\,\eta)\,\mathrm{d}\eta\right\}, \end{aligned} \tag{46b}$$

$$\begin{aligned} \bar{q}_z(\rho,\bar{h}) = {}&\bar{a}\,H(\rho-1) \\ &\times\left\{\int_0^\infty \eta\operatorname{csch}(\bar{h}\,\eta)\,J_0(\rho\,\eta)\,J_1(\bar{a}\,\eta)\,\mathrm{d}\eta - \sum_{n=0}^{\infty}\alpha_n\right. \\ &\times\left[\int_0^\infty\left(\eta\coth(\bar{h}\,\eta)\,\bar{N}_n(\eta) + \frac{8\,(n+1)\cos(\eta)}{\pi}\right)\right. \\ &\left.\left.\times J_0(\rho\,\eta)\,\mathrm{d}\eta - \frac{8\,(n+1)}{\pi\sqrt{\rho^2-1}}\right]\right\}. \end{aligned} \tag{46c}$$

Finally, the expression for the dimensionless heat flux intensity factor can be written as

$$\bar{K}_T = \frac{8\,\bar{a}}{\pi}\sum_{n=0}^{\infty}(n+1)\,\alpha_n. \tag{47}$$

IV. Numerical results and discussion

In the preceding section, we derived explicit expressions for the temperature, heat fluxes, and heat flux intensity factor, all of which are presented in dimensionless form in (44)-(47). In this section, we perform numerical calculations using these expressions to illustrate the thermal fields and analyze the influence of various parameters on these quantities. Furthermore, to validate the obtained results, a numerical simulation is conducted using finite element method (ANSYS software).

A. *Numerical scheme*

The thermal field variables and heat flux intensity factor are expressed in terms of the coefficients α_n, which are the solution of the algebraic system (43). Therefore, the calculation of these coefficients is crucial for further analysis of the involved physical quantities. To achieve this, we solve the algebraic system (43) using the truncation method [39, 40]. This approach involves selecting an appropriate finite number of equations from the system to solve, enabling us to obtain solutions for the coefficients α_n.

However, the analytical computation of the coefficient matrix elements $\bar{A}_{mn}$ and vector elements $\bar{b}_m$ poses a significant challenge due to their representation as infinite integrals (42a) and (42b), respectively. Therefore, we resort to numerical integration procedures. In this regard, we integrate $\bar{A}_{mn}$ in two steps: from 0 to a sufficiently large number, denoted as η_0, and from η_0 to infinity. Formally,

$$\bar{A}_{mn} = \int_0^{\eta_0} \coth(\bar{h}\,\eta)\,\bar{N}_n(\eta)\,\bar{Y}_m(\eta)\,\mathrm{d}\eta + A'_{mn}, \tag{48}$$

where A'_{mn} corresponds to the integral from η_0 to infinity. The evaluation of the first integral can be accomplished by utilizing an appropriate numerical method. The value of η_0 must be chosen sufficiently large to ensure that the term $\coth(\bar{h}\,\eta)$ approaches one. This allows us to approximate the improper integral A'_{mn} as

$$A'_{mn} \simeq \int_{\eta_0}^{\infty} \bar{N}_n(\eta)\,\bar{Y}_m(\eta)\,\mathrm{d}\eta. \tag{49}$$

Moreover, η_0 should also be sufficiently large to enable the effective use of the asymptotic expansion of Bessel functions. For example, a value of $\eta_0 = 5000$ may be used. Consequently, A'_{mn} can be evaluated through the expression

$$A'_{mn} \simeq \frac{128\,(-1)^m\,(m+1)\,(n+1)}{\pi^2}\left[\frac{\cos(\eta_0)^2}{\eta_0} + \mathrm{si}(2\,\eta_0)\right], \tag{50}$$

which is derived in Appendix A.C. In the above relation, si is the sine integral function defined by [27, Eq. (8.230 1)]

$$\mathrm{si}(x) = -\int_x^{\infty} \frac{\sin t}{t}\,\mathrm{d}t. \tag{51}$$

Regarding the infinite integral $\bar{b}_m$, it is worth noting that the term $\mathrm{csch}(\bar{h}\,\eta)$ rapidly decreases and approaches zero as η tends to infinity. Furthermore, based on the asymptotic expressions of Bessel's functions and $\bar{Y}_m(\eta)$ given by (A.18) and (A.21b), respectively, we can determine that $\bar{b}_m$ is a convergent integral. Consequently, we can evaluate it using an appropriate numerical method as

$$\bar{b}_m \simeq \int_0^{\eta_0} \mathrm{csch}(\bar{h}\,\eta)\,\bar{Y}_m(\eta)\,J_1(\bar{a}\,\eta)\,\mathrm{d}\eta. \tag{52}$$

By employing the aforementioned approximation scheme, we can effectively solve an appropriately truncated system of the algebraic system (43) with adequate accuracy. The first ten terms of α_n are presented in Tables I and II for various values of $\bar{a}$ and $\bar{h}$. One can observe that the coefficients exhibit rapid convergence. However, as $\bar{a}$ or $\bar{h}$ decrease, the convergence becomes slower. Nonetheless, extensive testing has shown that considering less than ten terms of the coefficients in the calculations is generally sufficient for generating convergent results in most practical cases, as shown in Table III.

Table. I

FIRST TENTH TERMS OF THE COEFFICIENTS α_n FOR VARIOUS VALUES OF $\bar{a}$ WITH $\bar{h} = 0.75$

	$\bar{h}=0.75$			
n	$\bar{a}=0.25$	$\bar{a}=0.5$	$\bar{a}=1$	$\bar{a}=2$
0	0.069516	0.133246	0.202032	0.142320
1	−0.022279	−0.033799	−0.017122	0.001066
2	0.006137	0.006334	−0.000630	−0.000118
3	−0.001516	−0.000792	0.000215	−0.000001
4	0.000343	0.000022	0.000005	0.000000
5	−0.000071	0.000020	−0.000004	0.000000
6	0.000013	−0.000006	0.000000	0.000000
7	−0.000002	0.000001	0.000000	0.000000
8	0.000000	0.000000	0.000000	0.000000
9	0.000000	0.000000	0.000000	0.000000

Table. II

FIRST TENTH TERMS OF THE COEFFICIENTS α_n FOR VARIOUS VALUES OF $\bar{h}$ WITH $\bar{a} = 1.5$

	$\bar{a}=1.5$			
n	$\bar{h}=0.25$	$\bar{h}=0.5$	$\bar{h}=1$	$\bar{h}=2$
0	0.324641	0.242438	0.134396	0.046306
1	0.034327	0.005770	−0.002950	−0.001347
2	0.000721	−0.000752	−0.000214	0.000015
3	−0.000479	−0.000058	0.000004	0.000001
4	−0.000037	−0.000002	0.000001	0.000000
5	0.000010	0.000000	0.000000	0.000000
6	0.000001	0.000000	0.000000	0.000000
7	0.000000	0.000000	0.000000	0.000000
8	0.000000	0.000000	0.000000	0.000000
9	0.000000	0.000000	0.000000	0.000000

Table. III

EXAMPLES OF NUMERICAL VALUES FOR DIMENSIONLESS THERMAL FIELDS AGAINST THE NUMBER OF TERMS USED IN THE CALCULATION.

$\bar{a}$	$\bar{h}$	ρ	ζ	m, n	$\bar{T}(\rho,\zeta)$	$\bar{q}_r(\rho,\zeta)$	$\bar{q}_z(\rho,\zeta)$
0.25	0.5	0.5	0.25	2	0.059183	0.267378	−0.078051
				4	0.063323	0.297678	−0.090873
				6	0.063718	0.299169	−0.091553
				8	0.063754	0.299283	−0.091693
				10	0.063753	0.299281	−0.091691
				15	0.063753	0.299281	−0.091691
0.5	1.5	1	0.75	2	0.044434	0.098666	0.028904
				4	0.044479	0.098762	0.028855
				6	0.044480	0.098763	0.028855
				8	0.044480	0.098763	0.028855
				10	0.044480	0.098763	0.028855
				15	0.044480	0.098763	0.028855
1	1.25	0.5	1	2	0.259398	0.219466	0.217509
				4	0.259694	0.220796	0.217074
				6	0.259692	0.220791	0.217074
				8	0.259692	0.220791	0.217074
				10	0.259692	0.220791	0.217074
				15	0.259692	0.220791	0.217074
2	0.75	1.5	0.25	2	0.631150	0.217688	1.395149
				4	0.631147	0.217675	1.395158
				6	0.631147	0.217675	1.395158
				8	0.631147	0.217675	1.395158
				10	0.631147	0.217675	1.395158
				15	0.631147	0.217675	1.395158

Once the coefficients α_n are determined, the thermal fields and heat flux intensity factor can be obtained from (44)-(47). It is important to note that the asymptotic expansions of Bessel's functions and $\bar{N}_n(\eta)$ (Eqs. A.18 and A.21a) provided in Appendix A, combined with the decreasing nature of the weight functions, guarantee the convergence of the integrals involved in the expressions for temperature and heat fluxes. Consequently, these integrals can be evaluated with a suitable level of accuracy using an appropriate numerical method.

B. Finite element modeling and comparison with the present results

For the sake of validating the solution obtained by the present method, we carry out a numerical simulation of the temperature field using ANSYS Workbench software. Figure 3 displays the finite element model along with the imposed boundary conditions. Here, we adopt the dimensionless forms of the coordinates, geometric parameters, temperature and heat fluxes, as established in subsection II.F. Due to the axisymmetric property of the problem, we only consider its projection onto the $(\rho,\,\zeta)$ plane.

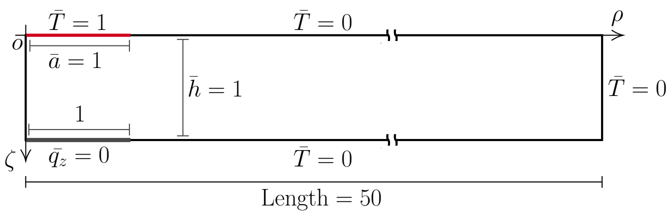

Fig. 3: Geometry and boundary conditions of the finite element model.

The geometric parameters are taken as $\bar{a}=\bar{h}=1$, while the length extends to 50. This specific length value is intentionally chosen to ensure that the computational results remain unaffected by this factor. Concerning boundary conditions, we impose the conditions prescribed in section II. Additionally, the temperatures on the boundary $\rho=50$ are set to zero, and the software automatically applies boundary conditions on the symmetry axis $\rho=0$.

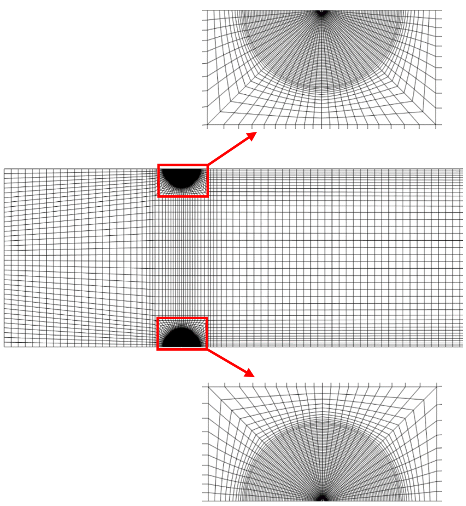

Fig. 4: Typical finite element mesh used for the analysis of heat conduction in a layer.

For the sake of discretization, the geometry is divided into quadrilateral elements, with a typical length of 0.04. Furthermore, triangular singular elements are used, and the mesh has been refined near points where $\rho=1$, $\zeta=0$ and $\zeta=1$ to accurately model temperature gradients and heat fluxes in these critical regions. A visual representation of a typical mesh used in the model is depicted in Fig. 4.

Figure 5 compares the radial distribution of the dimensionless temperature $\bar{T}$ at different ζ-plane ($\zeta=0.25$, 0.5, 0.75, and 1). As shown, the analytical and numerical results are in good agreement, thereby validating the present analysis.

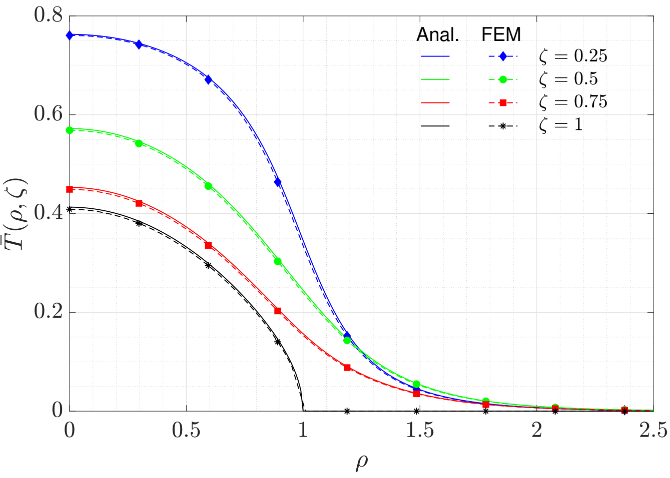

Fig. 5: Radial distribution of the dimensionless temperature $\bar{T}$ for various values of ζ with $\bar{a}=\bar{h}=1$, as obtained by the present analytical approach and the numerical simulation.

C. Thermal fields

The expressions (44)-(46) enable us to calculate the temperature and heat flux fields within the region $0\leq\zeta\leq\bar{h}$ of the medium. Furthermore, the symmetry characteristics with respect to the crack plane $\zeta=0$, which are inherent in the studied problems, require:

- For the first problem, which involves a penny-shaped crack as shown in Fig. 1(a), $\bar{T}$ and $\bar{q}_r$ should exhibit anti-symmetry, while $\bar{q}_z$ should be symmetric.
- In the case of an external crack, representing the second problem as depicted in Fig. 1(b), $\bar{T}$ and $\bar{q}_r$ should display symmetry, while $\bar{q}_z$ should exhibit anti-symmetry.

As a result, we can determine the thermal fields in the entire physical domain. Figures 6 and 7 show these fields around the crack region in both examined problems. The results are plotted for the case of $\bar{a}=2$ and $\bar{h}=1.5$.

In view of the symmetry characteristics of the studied problems, our discussion mainly focuses on the half-layer where $0\leq\zeta\leq\bar{h}$. From Figs. 6(a) and 7(a), it can be seen that the temperature is highest on the heated boundary area ($\bar{\zeta}=0$ and $0\leq\rho\leq\bar{a}$) and decreases as ρ or ζ increases. On the other hand, the temperature remains consistently at zero in the regions $\zeta=0$, $\rho>\bar{a}$ and $\zeta=\bar{h}$, $\rho>1$, in accordance with the boundary conditions (2a) and (2c).

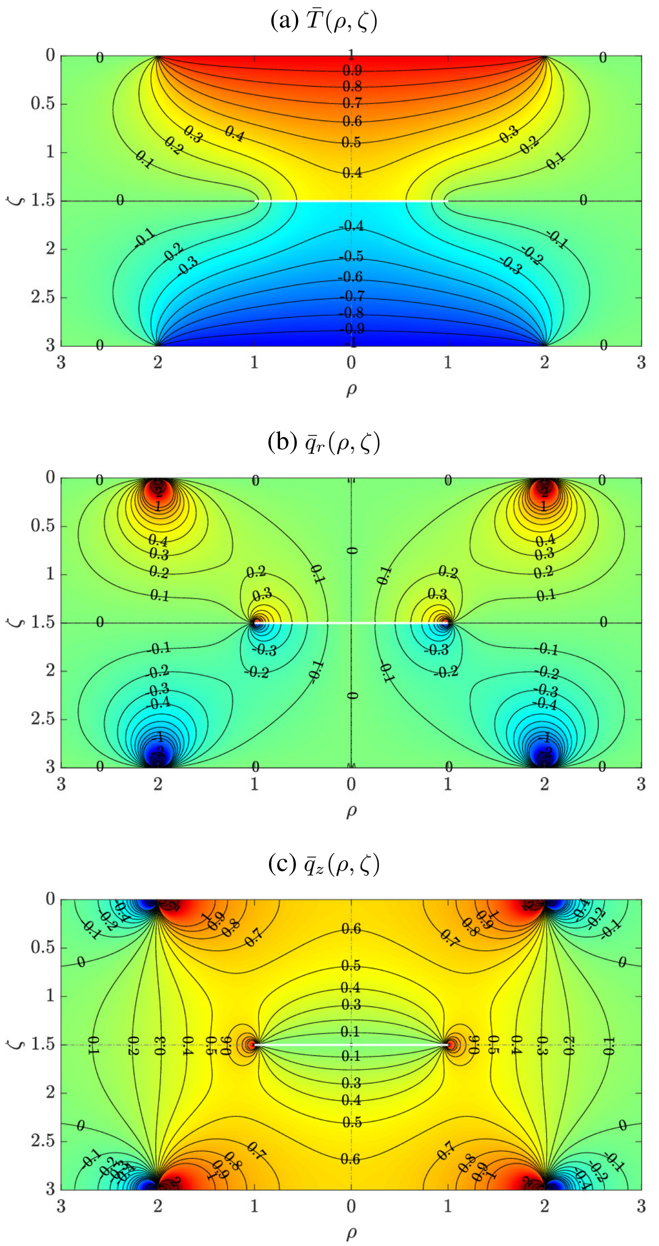

Fig. 6: Contour plots of the thermal fields around the crack region with $\bar{a} = 2$ and $\bar{h} = 1.5$ for the first problem (involving a penny-shaped crack). (a) $\bar{T}(\rho, \zeta)$; (b) $\bar{q}_r(\rho, \zeta)$; (c) $\bar{q}_z(\rho, \zeta)$.

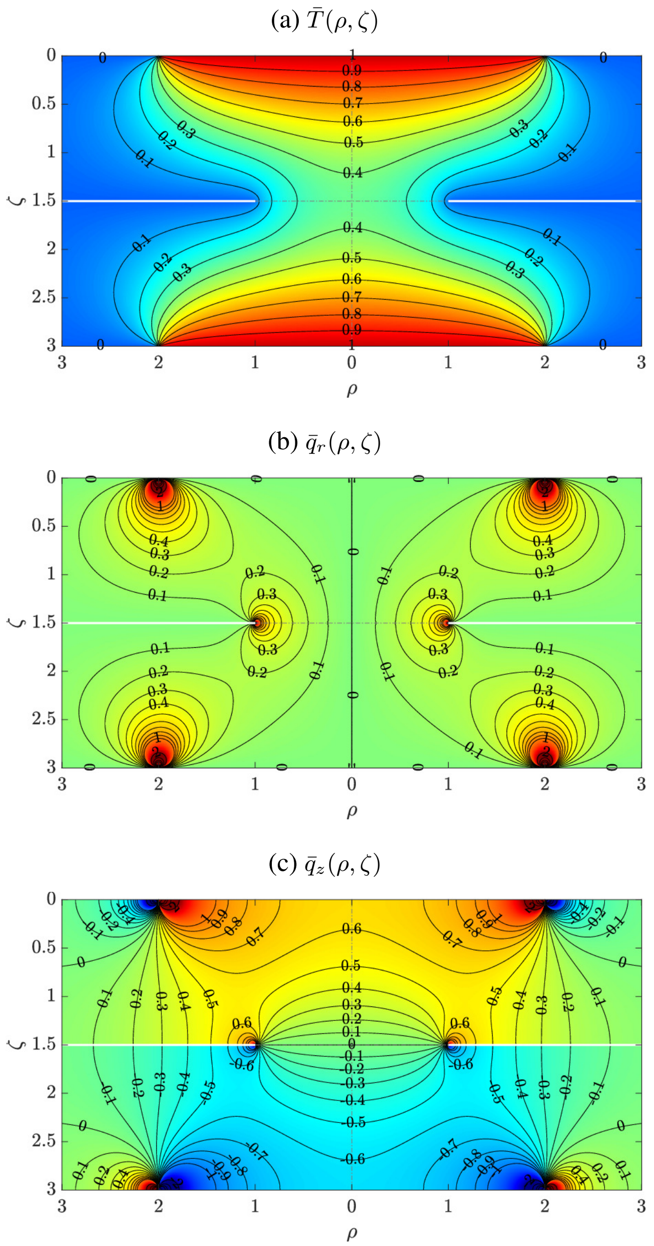

Fig. 7: Contour plots of the thermal fields around the crack region with $\bar{a} = 2$ and $\bar{h} = 1.5$ for the second problem (involving an external crack). (a) $\bar{T}(\rho, \zeta)$; (b) $\bar{q}_r(\rho, \zeta)$; (c) $\bar{q}_z(\rho, \zeta)$.

In the first problem, where the medium contains a penny-shaped crack, a temperature discontinuity is evident across the crack, as illustrated in Fig. 6(a). The temperature distributions on the lower and upper crack surfaces have equal magnitudes but opposite signs. This discontinuity reflects the heat transfer characteristics imposed by the boundary conditions and the nature of the crack. In contrast, in the second problem (the case of an external crack), the temperature in the region $\zeta = \bar{h}$, $\rho < 1$ remains continuous, as depicted in Fig. 7(a).

Figures 6(b), (c), 7(b) and (c) indicate that both heat fluxes are concentrated in the vicinity of the region $\zeta = 0$, $\rho = \bar{a}$ and near the crack tip ($\zeta = \bar{h}$, $\rho = 1$). They vary considerably around these areas and vanish as ρ becomes larger. Additionally, the heat flux in the radial direction vanishes in the median plane ($\zeta = \bar{h}$) for $\rho > 1$, as revealed in Figs. 6(b) and 7(b). These figures also show that $\bar{q}_r$ vanishes on the axis $\rho = 0$, which is consistent with the axisymmetric nature of the present problems.

Now, we investigate the effect of the dimensionless parameters $\bar{a}$ and $\bar{h}$ on the thermal fields along the crack plane. Considering the previously mentioned symmetry characteristics, we focus on the results related to the lower crack plane $\zeta = \bar{h}^-$. The variations of the dimensionless temperature $\bar{T}$ at this plane, as a function of the normalized radial coordinate ρ, are depicted in Figs. 8(a) and (b) for different values of $\bar{a}$ and $\bar{h}$, respectively.

It can be observed that, for a given $\bar{a}$ and $\bar{h}$, the temperature reaches its maximum value on the symmetry axis ($\rho = 0$) and decreases as ρ increases along the circular area of radius 1, until it vanishes at the crack tip ($\rho = 1$). On the remaining part of the crack plane ($\rho > 1$), the temperature remains consistently zero, conforming to the boundary condition (2c), which is also indicated in Figs. 6(a) and 7(a). Figure 8 also shows that, for a fixed value of $\bar{h}$, a significant temperature variation corresponds to a larger value of $\bar{a}$. Conversely, for a specific value of $\bar{a}$, notable temperature variation aligns with a smaller value of $\bar{h}$.

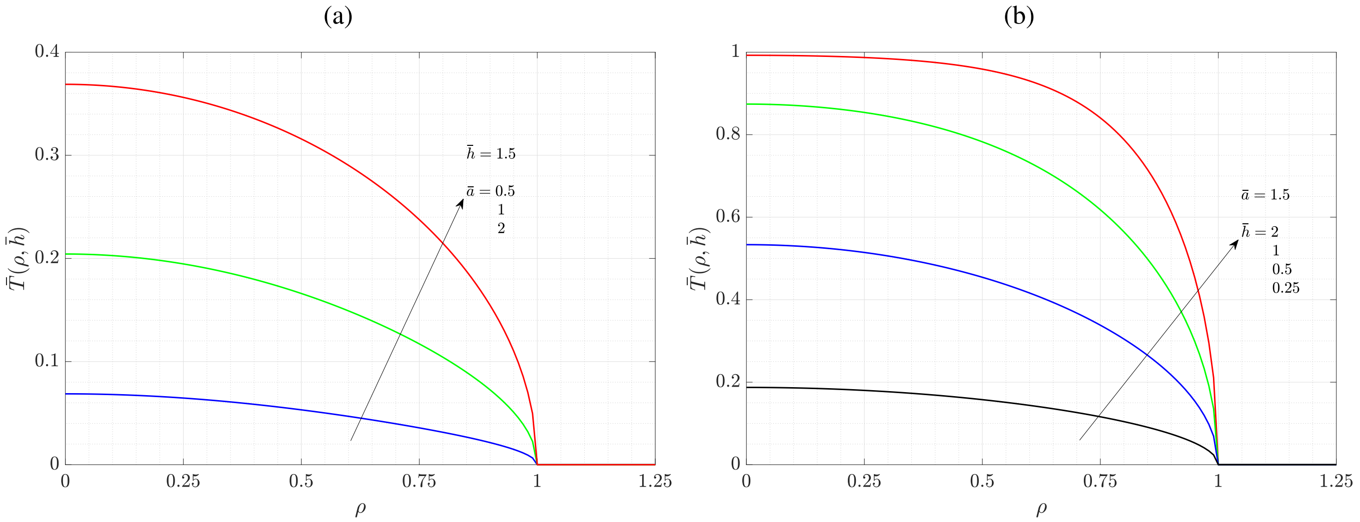

Fig. 8: Radial distribution of $\bar{T}$ on the lower crack plane ($\zeta = \bar{h}^-$) for: (a) various values of $\bar{a}$ with $\bar{h} = 1.5$; (b) different values of $\bar{h}$ with $\bar{a} = 1.5$.

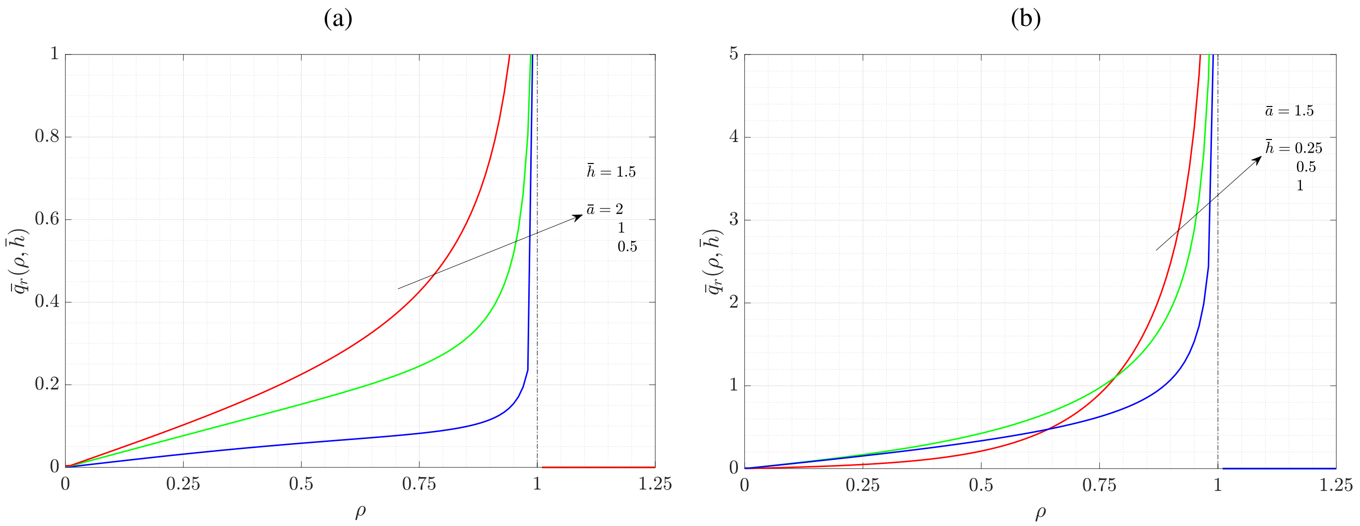

Fig. 9: Radial distribution of $\bar{q}_r$ on the lower crack plane ($\zeta = \bar{h}^-$) for: (a) various values of $\bar{a}$ with $\bar{h} = 1.5$; (b) different values of $\bar{h}$ with $\bar{a} = 1.5$.

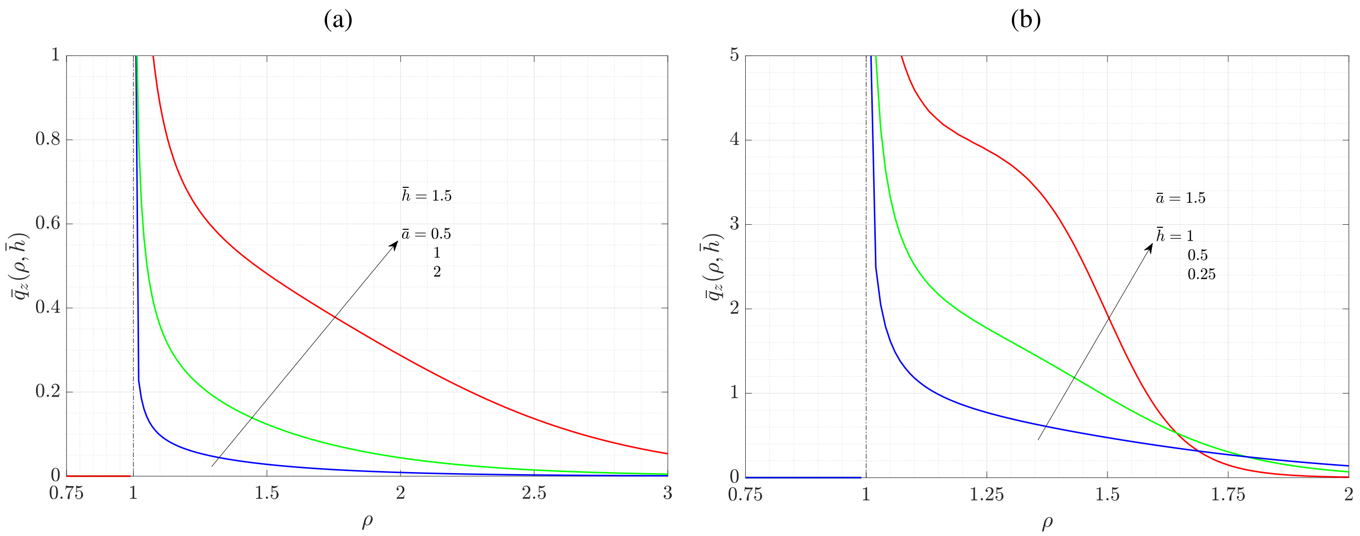

Fig. 10: Radial distribution of $\bar{q}_z$ on the lower crack plane ($\zeta = \bar{h}^-$) for: (a) various values of $\bar{a}$ with $\bar{h} = 1.5$; (b) different values of $\bar{h}$ with $\bar{a} = 1.5$.

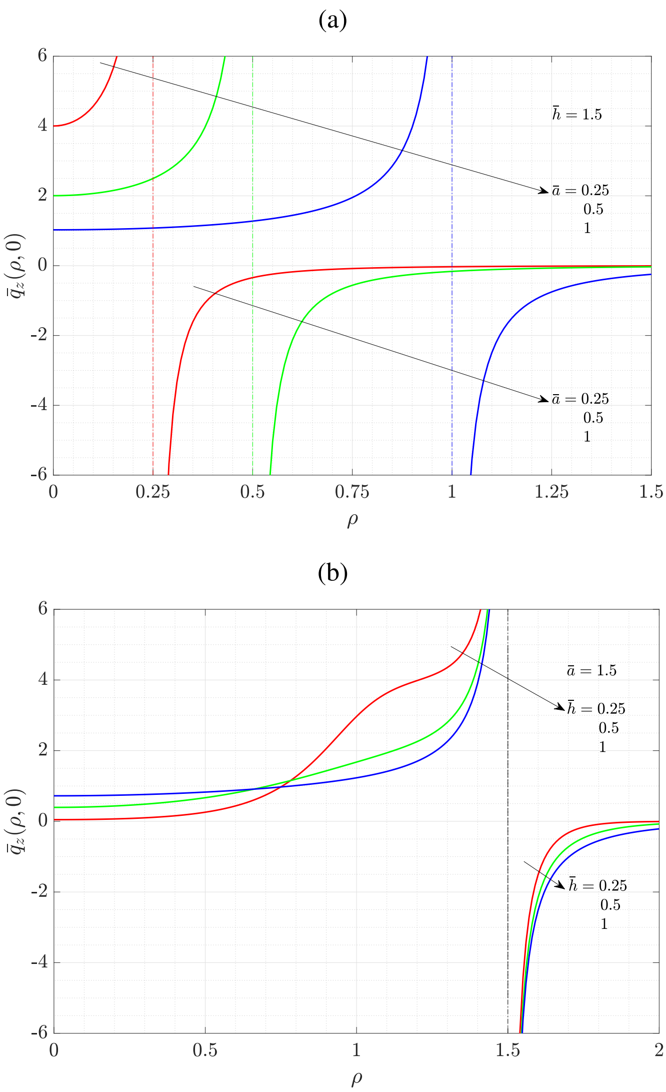

Fig. 11: Radial distribution of $\bar{q}_z$ on the external surface $\zeta = 0$ for: (a) various values of $\bar{a}$ with $\bar{h} = 1.5$; (b) different values of $\bar{h}$ with $\bar{a} = 1.5$.

Regarding the heat fluxes, Figs. 9 and 10 illustrate the distribution of $\bar{q}_r$ and $\bar{q}_z$ on the lower crack plane ($\zeta = \bar{h}^-$), respectively. The results are plotted for various values of the dimensionless parameters $\bar{a}$ and $\bar{h}$. From these figures, it is evident that both heat fluxes exhibit singular behavior near the crack tip. Specifically, the heat flux in the radial direction shows singularity in the vicinity $\rho \to 1^-$, whereas the heat flux in the axial direction displays singularity in the vicinity $\rho \to 1^+$.

Furthermore, as depicted in Fig. 9, the heat flux in the radial direction $\bar{q}_r$ vanishes at the center ($\rho = 0$), increases as ρ increases within the circular area $\rho < 1$, and exhibits significant variations in the vicinity of the crack tip ($\rho \to 1^-$). Along the remaining part of the crack plane (i.e., $\rho > 1$), $\bar{q}_r$ consistently remains zero, which is also shown in Figs. 6(b) and 7(b).

As dictated by the boundary condition (2b), the heat flux in the axial direction should vanish within the circular region $\rho < 1$. This condition is indicated in Fig. 10. It is also seen from this figure that $\bar{q}_z$ decays rapidly with increasing ρ ($\rho > 1$), eventually approaching zero as ρ becomes larger.

Moreover, Figs. 9(a) and 10(a) indicate that a larger radius $\bar{a}$ of the heated area results in larger heat fluxes on the lower crack plane. Similarly, from Figs. 9(b) and 10(b), it can be observed that as the crack is closer to the partially heated external surface ($\zeta = 0$), the heat fluxes on the lower crack plane are larger in magnitude.

The analysis of $\bar{q}_z$ variation at the plane $\zeta = 0$ is also of particular interest. The profiles of $\bar{q}_z$ along the radial direction at the external surface ($\zeta = 0$) are presented in Figs. 11(a) and (b) for different values of $\bar{a}$ and $\bar{h}$, respectively. It is clear that $\bar{q}_z$ is singular at $\rho = \bar{a}$ and varies significantly in its vicinity ($\rho \to \bar{a}^{\pm}$).

Notably, within the circular area of radius $\bar{a}$, $\bar{q}_z$ is positive, while it becomes negative on the remaining part of the external surface ($\rho > \bar{a}$). Additionally, the magnitude of $\bar{q}_z$ increases as ρ varies from 0 to $\bar{a}$. This trend also holds true for $\rho > \bar{a}$ (where $\bar{q}_z$ is negative), and it eventually tends toward zero as ρ becomes larger. Further analysis of both figures reveals that the profile of $\bar{q}_z$ varies across different combinations of $\bar{a}$ and $\bar{h}$. This difference is less noticeable when varying $\bar{h}$, especially when ρ is greater than $\bar{a}$, as shown in Fig. 11(b).

D. Heat flux intensity factor

In this subsection, we examine how the dimensionless parameters $\bar{a}$ and $\bar{h}$ influence the normalized heat flux intensity factor $\bar{K}_T$. To this end, we display in Fig. 12 a contour plot of $\bar{K}_T$ as a function of both $\bar{a}$ and $\bar{h}$. The plot is presented on a log-linear scale to better highlight the $\bar{K}_T$ variation. It is noteworthy to see from this figure that, as $\bar{a}$ increases up to 0.6, the magnitude of $\bar{K}_T$ consistently falls within the range of 0.1 to 0.2. This observation remains consistent when $\bar{a}$ exceeds 0.6, and $\bar{h}$ ranges from 3 to 5.

Additionally, for a fixed value of $\bar{h}$, the magnitude of the heat flux intensity factor rapidly increases as $\bar{a}$ rises from 0.6 to 1.2, then tends to stabilize with further increases in the value of $\bar{a}$. On the other hand, when $\bar{a}$ exceeds 1.2, $\bar{K}_T$ decreases monotonically as $\bar{h}$ increases. In other words, the closer the crack is to the external surfaces, the larger the magnitude of the heat flux intensity factor.

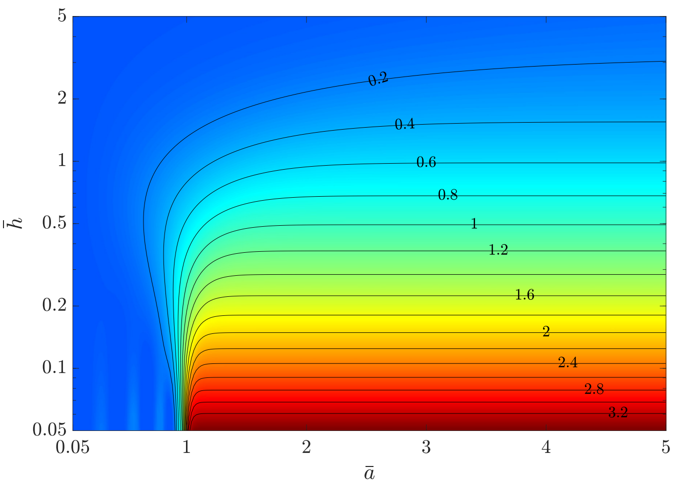

Fig. 12: Contour plot of the normalized heat flux intensity factor $\bar{K}_T$ versus $\bar{a}$ and $\bar{h}$ presented on a semi-logarithmic scale.

V. Conclusion

In this study, we investigated a heat conduction problem in a layer with prescribed temperature conditions that also containing a circular crack, either internal or external. Closed-form expressions were derived for various physical quantities, including temperature, heat fluxes, and heat flux intensity factor. Numerical results were presented to gain insight into the behavior of these quantities and their dependence on various parameters, such as the surface radius of the applied temperatures and the layer thickness.

The proposed method has demonstrated its effectiveness in solving the current heat conduction problem. Furthermore, its broad applicability extends beyond this specific case, allowing it to handle a wide range of mixed boundary value problems in the field of heat conduction, as well as in other scientific domains such as thermo-elasticity [15, 16], electrostatics [41, 42] and fluid mechanics [43, 44].

Our results may serve as valuable analytical tools for validating solutions obtained through numerical approaches. Furthermore, they can be utilized to derive thermal displacements and stresses for the corresponding thermoelastic problems, which will be addressed in future research endeavors.

Appendices

A Evaluation of the integrals

This appendix is dedicated to providing comprehensive details regarding the derivation of expressions for some integrals involved in this study.

A. $\int_0^\infty \xi \coth(h\,\xi)\, J_0(r\,\xi)\, J_1(a\,\xi)\, \mathrm{d}\xi$

Knowing that $\lim_{\xi\to\infty} \coth(h\,\xi) = 1$, the following integral can be rewritten as

$$\begin{aligned}&\int_0^\infty \xi \coth(h\,\xi)\, J_0(r\,\xi)\, J_1(a\,\xi)\, \mathrm{d}\xi \\ &= \int_0^\infty \xi \left[\coth(h\,\xi) - 1\right] J_0(r\,\xi)\, J_1(a\,\xi)\, \mathrm{d}\xi \\ &\quad + \int_0^\infty \xi\, J_0(r\,\xi)\, J_1(a\,\xi)\, \mathrm{d}\xi.\end{aligned} \tag{A.1}$$

Making use of the identity $\xi\, J_1(\xi) = -\partial J_0(a\,\xi)/\partial a$ and changing the order of integration and derivation, we get

$$\int_0^\infty \xi\, J_0(r\,\xi)\, J_1(a\,\xi)\, \mathrm{d}\xi = -\frac{\partial}{\partial a}\int_0^\infty J_0(a\,\xi)\, J_0(r\,\xi)\, \mathrm{d}\xi. \tag{A.2}$$

By virtue of [27, Eq. (6.576 2)], the integral on the right hand side of (A.2) can be evaluated as

$$\int_0^\infty J_0(a\,\xi)\, J_0(r\,\xi)\, \mathrm{d}\xi = \frac{F\left(\frac{1}{2},\, \frac{1}{2};\, 1;\, \frac{4\,r\,a}{(r+a)^2}\right)}{r+a}, \tag{A.3}$$

where F stands for the Gauss hypergeometric function defined by the following power series [27, Eq. (9.14)]

$$F(\alpha,\, \beta;\, \gamma;\, x) = \sum_{n=0}^{\infty} \frac{(\alpha)_n\, (\beta)_n}{(\gamma)_n}\, \frac{x^n}{n!}, \tag{A.4}$$

with $(\alpha)_n = \Gamma(\alpha+n)/\Gamma(\alpha)$, and $|x| < 1$. We denote by Γ the gamma function defined by $\Gamma(x) = \int_0^\infty t^{x-1}\, \mathrm{e}^{-t}\, \mathrm{d}t$, for $x > 0$. In addition, from [27, Eq. (8.113 1)], we have

$$F\left(\frac{1}{2},\, \frac{1}{2};\, 1;\, \frac{4\,r\,a}{(r+a)^2}\right) = \frac{2}{\pi} K\left(\frac{2\sqrt{r\,a}}{r+a}\right). \tag{A.5}$$

We insert (A.5) into (A.3) and proceed with the differentiation with respect to a, using the formula $\frac{\mathrm{d}K(x)}{\mathrm{d}x} = \frac{E(x)}{x\,(1-x^2)} - \frac{K(x)}{x}$ [27, Eq. (8.123 2)]. The resulting equation is then introduced into (A.1), and hence, we obtain

$$\begin{aligned}&\int_0^\infty \xi \coth(h\,\xi)\, J_0(r\,\xi)\, J_1(a\,\xi)\, \mathrm{d}\xi \\ &= \int_0^\infty \xi \left[\coth(h\,\xi) - 1\right] J_0(r\,\xi)\, J_1(a\,\xi)\, \mathrm{d}\xi \\ &\quad - \frac{1}{\pi\,a}\left[\frac{E\left(\frac{2\sqrt{a\,r}}{r+a}\right)}{r-a} - \frac{K\left(\frac{2\sqrt{a\,r}}{r+a}\right)}{r+a}\right].\end{aligned} \tag{A.6}$$

Regarding the evaluation of the integral on the right-hand side of (A.6), it is worth noting that it converges rapidly. Therefore, it can be truncated to an integral from 0 to a sufficiently large number and subsequently evaluated numerically using a suitable method.

B. $\int_0^\infty \xi\, N_n(\xi)\, J_1(r\,\xi)\, \mathrm{d}\xi$

We use the relation $\xi\, J_1(\xi) = -\partial J_0(r\,\xi)/\partial r$ to express the considered integral as

$$\int_0^\infty \xi\, N_n(\xi)\, J_1(r\,\xi)\, \mathrm{d}\xi = -\frac{\partial}{\partial r}\int_0^\infty N_n(\xi)\, J_0(r\,\xi)\, \mathrm{d}\xi. \tag{A.7}$$

Then, with the help of (15), we get

$$\begin{aligned}&\frac{\partial}{\partial r}\int_0^\infty N_n(\xi)\, J_0(r\,\xi)\, \mathrm{d}\xi \\ &= \frac{4}{\pi\, b^2}\, \frac{\partial}{\partial r}\left[\frac{\sqrt{b^2-r^2}}{r}\, H(b-r)\, U_{2\,n+1}(r/b)\right]\end{aligned} \tag{A.8a}$$

$$\begin{aligned}&= \frac{4}{\pi\, b^2}\left[\frac{\sqrt{b^2-r^2}}{r}\, U_{2\,n+1}(r/b)\, \frac{\partial}{\partial r} H(b-r) \right.\\ &\quad \left. + H(b-r)\, \frac{\partial}{\partial r}\left(\frac{\sqrt{b^2-r^2}}{r}\, U_{2\,n+1}(r/b)\right)\right].\end{aligned} \tag{A.8b}$$

Knowing that $\partial H(b-r)/\partial r = \delta(b-r) = 0$ for $r \neq b$, and

$$\lim_{r\to b^-}\left[\frac{\sqrt{b^2-r^2}}{r}\, \delta(b-r)\, U_{2\,n+1}(r/b)\right] = 0, \tag{A.9}$$

we determine that the first term involved in (A.8b) vanishes.

On the other hand, by employing the variable change $\rho = r/b$, the remaining partial derivative involved in (A.8b) can be transformed into the following form

$$\frac{\partial}{\partial r}\left[\frac{\sqrt{b^2-r^2}}{r}\, U_{2\,n+1}(r/b)\right] = \frac{\partial}{b\,\partial\rho}\left[\frac{\sqrt{1-\rho^2}}{\rho}\, U_{2\,n+1}(\rho)\right]. \tag{A.10}$$

Before proceeding with differentiation, let us introduce the differentiation formula for the Chebyshev polynomials U_n as follows

$$\frac{\mathrm{d}}{\mathrm{d}x}\, U_n(x) = \frac{(n+1)T_{n+1}(x) - x\, U_n(x)}{x^2-1}, \tag{A.11}$$

where T_n represents Chebyshev's polynomials of the first kind of degree n, defined by [27, Eq. (8.940 1)] as $T_n(x) = \cos(n \arccos x)$. Here, it is worth mentioning that (A.11) is obtained by differentiating the polynomials in their trigonometric forms. Considering (A.11), we perform the differentiation on the right-hand side of (A.10). This operation results in

$$\begin{aligned}&\frac{\partial}{\partial \rho}\left[\frac{\sqrt{1-\rho^2}}{\rho}\, U_{2\,n+1}(\rho)\right]\\&= -\frac{2\,(n+1)\,\rho\, T_{2\,n+2}(\rho) + (1-\rho^2) U_{2\,n+1}(\rho)}{\rho^2\,\sqrt{1-\rho^2}}.\end{aligned} \tag{A.12}$$

By making use of the following recursion formulas [27, Eq. (8.941 3 and 2)]

$$T_n(x) = U_n(x) - x\, U_{n-1}(x), \tag{A.13a}$$
$$U_{n+1}(x) - 2\,x\, U_n(x) + U_{n-1}(x) = 0, \tag{A.13b}$$

(A.12) can be expressed in terms of Chebyshev's polynomials of the second kind only, and further can be simplified to

$$\begin{aligned}&\frac{\partial}{\partial \rho}\left[\frac{\sqrt{1-\rho^2}}{\rho}\, U_{2\,n+1}(\rho)\right]\\&= \frac{2\,(n+1)\,\rho\, U_{2\,n}(\rho) - \left[(2\,n+1)\,\rho^2 + 1\right] U_{2\,n+1}(\rho)}{\rho^2\,\sqrt{1-\rho^2}}.\end{aligned} \tag{A.14}$$

Hence, by inserting (A.14) into (A.10) and remembering that $\rho = r/b$, we find that

$$\begin{aligned}&\frac{\partial}{\partial r}\left[\frac{\sqrt{b^2-r^2}}{r}\, U_{2\,n+1}(r/b)\right]\\&= \frac{1}{r^2\,\sqrt{b^2-r^2}}\big\{2\,(n+1)\,b\,r\, U_{2\,n}(r/b)\\&\quad - \left[(2\,n+1)\,r^2 + b^2\right] U_{2\,n+1}(r/b)\big\}.\end{aligned} \tag{A.15}$$

Via substitution of (A.15) into (A.7), one finally obtains the following analytical expression for the integral under consideration

$$\begin{aligned}&\int_0^\infty \xi\, N_n(\xi)\, J_1(r\,\xi)\,\mathrm{d}\xi\\&= -\frac{4\,H(b-r)}{\pi\, b^2\, r^2\,\sqrt{b^2-r^2}}\big\{2\,(n+1)\,b\,r\, U_{2\,n}(r/b)\\&\quad - \left[(2\,n+1)\,r^2 + b^2\right] U_{2\,n+1}(r/b)\big\}.\end{aligned} \tag{A.16}$$

C. $\int_{\eta_0}^\infty \bar{N}_n(\eta)\,\bar{Y}_m(\eta)\,\mathrm{d}\eta$

Upon introducing the variable change $\eta = b\,\xi$, the functions $\bar{M}_n$, $\bar{X}_m$, $\bar{N}_n$, and $\bar{Y}_m$ are expressed as follows

$$\bar{M}_n(\eta) = M_n(\eta/b) = J_{n+1/2}\,(\eta/2)\; J_{-(n+1/2)}(\eta/2), \tag{A.17a}$$
$$\bar{N}_n(\eta) = \eta\left[\bar{M}_n(\eta) - \bar{M}_{n+1}(\eta)\right], \tag{A.17b}$$
$$\bar{X}_m(\eta) = X_m(\eta/b) = J^2_m\,(\eta/2)\,, \tag{A.17c}$$
$$\bar{Y}_m(\eta) = \eta\left[\bar{X}_m(\eta) - \bar{X}_{m+2}(\eta)\right]. \tag{A.17d}$$

On the other hand, the asymptotic expansion of the Bessel function J_ν for large values of the argument x reads [27, Eq. (8.451 1)]

$$\begin{aligned}J_\nu(x) = \sqrt{\frac{2}{\pi\, x}}&\left[\cos\!\left(x - (2\,\nu+1)\,\frac{\pi}{4}\right) - \frac{4\,\nu^2-1}{8\,x}\right.\\&\left.\times \sin\!\left(x - (2\,\nu+1)\,\frac{\pi}{4}\right) + O\!\left(\frac{1}{x^2}\right)\right].\end{aligned} \tag{A.18}$$

We then use (A.18) along with the trigonometric identities below

$$\begin{aligned}&\cos(x)\,\cos(y) = \left[\cos(x+y) + \cos(x-y)\right]/2,\\&\cos(x)\,\sin(y) = \left[\sin(x+y) - \sin(x-y)\right]/2,\\&\cos(x+y) = \cos(x)\,\cos(y) - \sin(x)\,\sin(y),\\&\sin(x+y) = \cos(x)\,\sin(y) + \sin(x)\,\cos(y),\end{aligned} \tag{A.19}$$

to get the following asymptotic expansions of $\bar{M}_n$ and $\bar{X}_m$

$$\bar{M}_n(\eta) = \frac{2}{\pi\,\eta}\left[\sin(\eta) + \frac{2\,n\,(n+1)\cos(\eta)}{\eta}\right] + O\!\left(\frac{1}{\eta^3}\right), \tag{A.20a}$$

$$\begin{aligned}\bar{X}_m(\eta) = \frac{2}{\pi\,\eta}&\Big[1 + (-1)^m\,\sin(\eta) + (-1)^m\\&\times\left(4\,m^2-1\right)\frac{\cos(\eta)}{2\,\eta}\Big] + O\!\left(\frac{1}{\eta^3}\right).\end{aligned} \tag{A.20b}$$

Substituting (A.20a) and (A.20b) into (A.17b) and (A.17d), respectively, with some algebraic manipulations, we obtain

$$\bar{N}_n(\eta) = -\frac{8\,(n+1)\cos(\eta)}{\pi\,\eta} + O\!\left(\frac{1}{\eta^2}\right), \tag{A.21a}$$
$$\bar{Y}_m(\eta) = -\frac{16\,(-1)^m\,(m+1)\cos(\eta)}{\pi\,\eta} + O\!\left(\frac{1}{\eta^2}\right). \tag{A.21b}$$

By virtue of (A.21), the following integral can be approximated as

$$\begin{aligned}\int_{\eta_0}^\infty \bar{N}_n(\eta)\,\bar{Y}_m(\eta)\,\mathrm{d}\eta &\simeq \frac{128\,(-1)^m\,(m+1)\,(n+1)}{\pi^2}\\&\quad\times\int_{\eta_0}^\infty \frac{\cos(\eta)^2}{\eta^2}\,\mathrm{d}\eta.\end{aligned} \tag{A.22}$$

We shall proceed to perform integration by parts on the right-hand side of (A.22). Given that $\left.\frac{\cos(\eta)^2}{\eta}\right|_{\eta_0}^{\infty} = -\frac{\cos(\eta_0)^2}{\eta_0}$ and the identity $2\,\cos x\,\sin x = \sin 2\,x$, one gets

$$\int_{\eta_0}^\infty \frac{\cos(\eta)^2}{\eta^2}\,\mathrm{d}\eta = \frac{\cos(\eta_0)^2}{\eta_0} + \mathrm{si}(2\,\eta_0), \tag{A.23}$$

where si is the sine integral function defined previously by (51). Finally, inserting (A.23) into (A.22), yields

$$\begin{aligned}\int_{\eta_0}^\infty \bar{N}_n(\eta)\,\bar{Y}_m(\eta)\,\mathrm{d}\eta &\simeq \frac{128\,(-1)^m\,(m+1)\,(n+1)}{\pi^2}\\&\quad\times\left[\frac{\cos(\eta_0)^2}{\eta_0} + \mathrm{si}(2\,\eta_0)\right].\end{aligned} \tag{A.24}$$

D. $\int_0^\infty \xi \coth(h\,\xi)\, N_n(\xi)\, J_0(r\,\xi)\,\mathrm{d}\xi$

From (A.21a), we have

$$N_n(\xi) = \frac{\bar{N}_n(b\,\xi)}{b} \sim -\frac{8\,(n+1)\cos(b\,\xi)}{\pi\, b^2\,\xi}, \quad \text{as} \quad \xi \to \infty. \tag{A.25}$$

Knowing that $\lim_{\xi\to\infty} \coth(h\,\xi) = 1$, we get

$$\begin{aligned}&\int_0^\infty \xi \coth(h\,\xi)\, N_n(\xi)\, J_0(r\,\xi)\,\mathrm{d}\xi\\&= \int_0^\infty \left[\xi \coth(h\,\xi)\, N_n(\xi) + \frac{8\,(n+1)\cos(b\,\xi)}{\pi\, b^2}\right]\\&\quad\times J_0(r\,\xi)\,\mathrm{d}\xi - \frac{8\,(n+1)}{\pi\, b^2}\int_0^\infty \cos(b\,\xi)\, J_0(r\,\xi)\,\mathrm{d}\xi.\end{aligned} \tag{A.26}$$

Recalling the relation [27, Eq. (6.671 2)], yields

$$\int_0^\infty \cos(b\,\xi)\, J_0(r\,\xi)\,\mathrm{d}\xi = \frac{1}{\sqrt{r^2-b^2}}, \qquad r > b. \tag{A.27}$$

Finally, after substitution of (A.27) into (A.26), the resulting expression is

$$\begin{aligned}&\int_0^\infty \xi \coth(h\,\xi)\, N_n(\xi)\, J_0(r\,\xi)\,\mathrm{d}\xi \\ &= \int_0^\infty \left[\xi \coth(h\,\xi)\, N_n(\xi) + \frac{8\,(n+1)\cos(b\,\xi)}{\pi\, b^2}\right] \\ &\quad \times J_0(r\,\xi)\,\mathrm{d}\xi - \frac{8\,(n+1)}{\pi\, b^2\sqrt{r^2-b^2}}.\end{aligned} \tag{A.28}$$

B Exact solution for the half-space case ($h \to \infty$)

In this appendix, we present an exact solution for a steady-state heat conduction problem within a semi-infinite medium. This medium is exposed to a constant temperature over a circular region on its external surface. The corresponding governing equation is given by (1), and it is subject to the boundary condition (2a). In addition, the regularity condition requires the thermal fields to vanish at infinity ($\sqrt{r^2+z^2} \to \infty$).

By following the same solution procedure presented in the subsection III.*A*, one obtains

$$T_H(\xi, z) = \frac{\mathrm{e}^{-z\,\xi}\, A(\xi)}{\xi}, \tag{B.1}$$

where A denotes an unknown function. Then, Applying the boundary condition (2a) and Hankel transform theorem, we obtain

$$A(\xi) = a\, T_0\, J_1(a\,\xi). \tag{B.2}$$

Substituting (B.2) into (B.1) and performing the Hankel inversion transform given by (3b) yields the explicit formula below

$$T = a\, T_0 \int_0^\infty \mathrm{e}^{-z\,\xi}\, J_0(r\,\xi)\, J_1(a\,\xi)\,\mathrm{d}\xi. \tag{B.3}$$

Subsequently, the following expressions for heat fluxes are derived

$$q_r = a\,k\,T_0 \int_0^\infty \xi\,\mathrm{e}^{-z\,\xi}\, J_1(a\,\xi)\, J_1(r\,\xi)\,\mathrm{d}\xi, \tag{B.4a}$$
$$q_z = a\,k\,T_0 \int_0^\infty \xi\,\mathrm{e}^{-z\,\xi}\, J_0(r\,\xi)\, J_1(a\,\xi)\,\mathrm{d}\xi. \tag{B.4b}$$

Acknowledgement

The support from Directorate-General for Scientific Research and Technological Development (DG-RSDT) of Algerian government in the form of research grant is gratefully acknowledged. The Laboratory of Green and Mechanical Development (LGMD) of National Polytechnic School (ENP) is also gratefully acknowledged for the resources and support.

References

[1] K. Cole, J. Beck, A. Haji-Sheikh, and B. Litkouhi, *Heat conduction using Greens functions*. New York: CRC Press, 2010.

[2] D. W. Hahn and M. N. Özisik, *Heat conduction*. New Jersey: John Wiley & Sons, 2012.

[3] S. Kakaç, Y. Yener, and C. P. Naveira-Cotta, *Heat conduction*. New York: CRC Press, 2018.

[4] R. S. Dhaliwal, "Mixed boundary value problem of heat conduction for infinite slab," *Applied Scientific Research*, vol. 16, no. 1, pp. 228–240, 1966. doi: 10.1007/BF00384070

[5] R. S. Dhaliwal, "An axisymmetric mixed boundary value problem for a thick slab," *SIAM Journal on Applied Mathematics*, vol. 15, no. 1, pp. 98–106, 1967. doi: 10.1137/0115006

[6] J. V. Beck, "Large time solutions for temperatures in a semi-infinite body with a disk heat source," *International Journal of Heat and Mass Transfer*, vol. 24, no. 1, pp. 155–164, 1981. doi: 10.1016/0017-9310(81)90104-6

[7] R. C. Mehta and T. K. Bose, "Temperature distribution in a large circular plate heated by a disk heat source," *International Journal of Heat and Mass Transfer*, vol. 26, no. 7, pp. 1093–1095, 1983. doi: 10.1016/S0017-9310(83)80136-7

[8] G. M. L. Gladwell, J. R. Barber, and Z. Olesiak, "Thermal problems with radiation boundary conditions," *The Quarterly Journal of Mechanics and Applied Mathematics*, vol. 36, no. 3, pp. 387–401, 1983. doi: 10.1093/qjmam/36.3.387

[9] T. F. Lemczyk and M. M. Yovanovich, "Thermal constriction resistance with convective boundary conditions—1. half-space contacts," *International Journal of Heat and Mass Transfer*, vol. 31, no. 9, pp. 1861–1872, 1988. doi: 10.1016/0017-9310(88)90200-1

[10] T. F. Lemczyk and M. M. Yovanovich, "Thermal constriction resistance with convective boundary conditions—2. layered half-space contacts," *International Journal of Heat and Mass Transfer*, vol. 31, no. 9, pp. 1873–1883, 1988. doi: 10.1016/0017-9310(88)90201-3

[11] T. V. Rao, "Effect of surface layers on the constriction resistance of an isothermal spot. part I: Reduction to an integral equation and numerical results," *Heat and Mass Transfer*, vol. 40, no. 6-7, pp. 439–453, 2004. doi: 10.1007/s00231-003-0490-4

[12] T. V. Rao, "Effect of surface layers on the constriction resistance of an isothermal spot. part II: Analytical results for thick layers," *Heat and Mass Transfer*, vol. 40, no. 6-7, pp. 455–466, 2004. doi: 10.1007/s00231-003-0491-3

[13] N. Laraqi, E.-K. Chahour, E. Monier-Vinard, N. Fahdi, C. Zerbini, and M.-N. Nguyen, "Simple and accurate correlations for some problems of heat conduction with nonhomogeneous boundary conditions," *Thermal Science*, vol. 21, no. 1 Part A, pp. 125–132, 2017. doi: 10.2298/TSCI160411243L

[14] X.-F. Li and K. Y. Lee, "Effect of heat conduction of penny-shaped crack interior on thermal stress intensity factors," *International Journal of Heat and Mass Transfer*, vol. 91, pp. 127–134, 2015. doi: 10.1016/j.ijheatmasstransfer.2015.07.087

[15] X.-Y. Li, P.-D. Li, G.-Z. Kang, W.-Q. Chen, and R. Müller, "Steady-state thermo-elastic field in an infinite medium weakened by a penny-shaped crack: Complete and exact solutions," *International Journal of Solids and Structures*, vol. 84, pp. 167–182, 2016. doi: 10.1016/j.ijsolstr.2016.02.001

[16] P.-D. Li, X.-Y. Li, and G.-Z. Kang, "Axisymmetric thermo-elastic field in an infinite space containing a penny-shaped crack under a pair of symmetric uniform heat fluxes and its applications," *International Journal of Mechanical Sciences*, vol. 115, pp. 634–644, 2016. doi: 10.1016/j.ijmecsci.2016.07.027

[17] B. Kebli and Z. Baka, "Annular crack in a thermoelastic half-space," *Journal of Thermal Stresses*, vol. 43, no. 11, pp. 1379–1414, 2020. doi: 10.1080/01495739.2020.1782294

[18] J. Wang, M. Dai, and C.-F. Gao, "The effect of interfacial thermal resistance on interface crack subjected to remote heat flux," *Zeitschrift für angewandte Mathematik und Physik*, vol. 71, no. 12, pp. 1–21, 2020. doi: 10.1007/s00033-019-1235-7

[19] G. C. Sih, "Heat conduction in the infinite medium with lines of discontinuities," *Journal of Heat Transfer*, vol. 87, no. 2, pp. 293–298, 1965. doi: 10.1115/1.3689092

[20] C. Chao and R. Chang, "Steady-state heat conduction problem of the interface crack between dissimilar anisotropic media," *International Journal of Heat and Mass Transfer*, vol. 36, no. 8, pp. 2021–2026, 1993. doi: 10.1016/S0017-9310(05)80133-4

[21] D. Y. Tzou, "The singular behavior of the temperature gradient in the vicinity of a macrocrack tip," *International Journal of Heat and Mass Transfer*, vol. 33, no. 12, pp. 2625–2630, 1990. doi: 10.1016/0017-9310(90)90198-4

[22] T.-C. Chiu, S.-W. Tsai, and C.-H. Chue, "Heat conduction in a functionally graded medium with an arbitrarily oriented crack," *International Journal of Heat and Mass Transfer*, vol. 67, pp. 514–522, 2013. doi: 10.1016/j.ijheatmasstransfer.2013.08.022

[23] S.-W. Tsai, T.-C. Chiu, and C.-H. Chue, "Temperature distribution and heat flow around a crack of arbitrary orientation in a functionally graded medium," *Journal of Engineering Mathematics*, vol. 87, no. 1, pp. 123–137, 2014. doi: 10.1007/s10665-013-9664-3

[24] H. Deng, B. Yan, H. Su, X. Zhang, and X. Lv, "An interaction integral method for calculating heat flux intensity factor with the XFEM," *International Journal of Thermal Sciences*, vol. 136, pp. 379–388, 2019. doi: 10.1016/j.ijthermalsci.2018.09.022

[25] H. Deng, B. Yan, H. Su, X. Zhang, and X. Lv, "Study on transient heat flux intensity factor with interaction integral," *International Journal of Thermal Sciences*, vol. 146, p. 106014, 2019. doi: 10.1016/j.ijthermalsci.2019.106014

[26] L. Debnath and D. Bhatta, *Integral transforms and their applications*. New York: Chapman and Hall/CRC, 2015.

[27] I. S. Gradshteyn and I. M. Ryzhik, *Table of integrals, series, and products*. London: Academic press, 2014.

[28] I. N. Sneddon, "The elementary solution of dual integral equations," *Glasgow Mathematical Journal*, vol. 4, no. 3, pp. 108–110, 1960. doi: 10.1017/S2040618500034006

[29] I. N. Sneddon, *Mixed boundary value problems in potential theory*. North-Holland, 1966.

[30] D. G. Duffy, *Mixed boundary value problems*. New York: CRC Press, 2008.

[31] M. Sakamoto, "An elastic layer with a penny-shaped crack subjected to internal pressure," *JSME International Journal, Series A, Solid Mechanics and Material Engineering*, vol. 46, no. 1, pp. 10–14, 2003. doi: 10.1299/jsmea.46.10

[32] B. Kebli and F. Madani, "The Reissner-Sagoci problem for an interfacial crack in an elastic bilayer medium under torsion of an embedded rigid circular disc," *Theoretical and Applied Fracture Mechanics*, vol. 110, 2020. doi: 10.1016/j.tafmec.2020.102825

[33] K. Miura, M. Sakamoto, and Y. Tanabe, "Analytical solution of axisymmetric indentation of multi-layer coating on elastic substrate body," *Acta Mechanica*, vol. 231, pp. 4077–4093, 2020. doi: 10.1007/s00707-020-02752-1

[34] K. Miura, M. Sakamoto, and Y. Tanabe, "Analytical solution for the axisymmetric problem of a penny-shaped crack under internal pressure in a multi-layer composite," *Mechanical Engineering Journal*, vol. 8, no. 2, 2021. doi: 10.1299/mej.21-00025

[35] K. Miura, C. Oyama, M. Sakamoto, and Y. Tanabe, "Indentation method accounting for thickness effect of viscoelastic layer," *ZAMM-Journal of Applied Mathematics and Mechanics/Zeitschrift für Angewandte Mathematik und Mechanik*, vol. 101, no. 10, 2021. doi: 10.1002/zamm.202000272

[36] B. Kebli and A. Gouadria, "Axisymmetric torsion problem by a rigid disc of an elastic half-space weakened by an annular crack," *Theoretical and Applied Fracture Mechanics*, vol. 123, 2023. doi: 10.1016/j.tafmec.2022.103676

[37] Z. Baka and B. Kebli, "Heat conduction problem for a half-space medium containing a penny-shaped crack," *Archive of Applied Mechanics*, vol. 93, no. 2, pp. 635–662, 2023. doi: 10.1007/s00419-022-02291-2

[38] I. Sevostianov, "Thermal conductivity of a material containing cracks of arbitrary shape," *International Journal of Engineering Science*, vol. 44, no. 8-9, pp. 513–528, 2006. doi: 10.1016/j.ijengsci.2006.04.001

[39] R. Li, Y. Zhong, B. Tian, and Y. Liu, "On the finite integral transform method for exact bending solutions of fully clamped orthotropic rectangular thin plates," *Applied Mathematics Letters*, vol. 22, no. 12, pp. 1821–1827, 2009. doi: 10.1016/j.aml.2009.07.003

[40] Y. Zhong and Q. Xu, "Analysis bending solutions of clamped rectangular thick plate," *Mathematical Problems in Engineering*, vol. 2017, 2017. doi: 10.1155/2017/7539276

[41] S. Choo, M. Leong, and W. Low, "The contact resistance at the interface between a disc electrode and an infinite slab: Mixed-boundary-value solutions," *Solid-State Electronics*, vol. 29, no. 5, pp. 535–543, 1986. doi: 10.1016/0038-1101(86)90075-4

[42] K. Seki, "Quantifying the spreading currents over the circular contact region in a good conducting cover layer on a substrate," *Journal of Physics D: Applied Physics*, vol. 53, no. 43, p. 435103, 2020. doi: 10.1088/1361-6463/ab9e37

[43] J. P. Tanzosh and H. A. Stone, "Transverse motion of a disk through a rotating viscous fluid," *Journal of Fluid Mechanics*, vol. 301, p. 295–324, 1995. doi: 10.1017/S0022112095003909

[44] A. M. Davis and S. G. L. Smith, "Tangential oscillations of a circular disk in a viscous stratified fluid," *Journal of Fluid Mechanics*, vol. 656, pp. 342–359, 2010. doi: 10.1017/S0022112010001205

Zakaria Baka received his Engineering, Master's, and Ph.D. degrees in Mechanical Engineering from the Ecole Nationale Polytechnique (ENP), Algiers, Algeria, in 2013, 2014, and 2024, respectively. He is currently conducting research at the Laboratory of Green and Mechanical Development (LGMD), ENP. His research interests include engineering mechanics, solid mechanics, heat transfer, elasticity, and thermo-elasticity.

Belkacem Kebli is a full Professor at the Department of Mechanical Engineering at the Ecole Nationale Polytechnique (ENP), Algiers, Algeria. He received High Studies Diploma (DES) in Functional Analysis from Ferhat Abbas University, Setif in 1986, and Ph. D. degree in Physics and Mathematics from Mechnikov University, Odessa in 1991. His main research interests include Elasticity theory, Fracture mechanics, and both Analytical and Numerical solutions of PDEs.

Electrochemical Behavior of Corrosion on Borided and Non-borided Steel Immersed in NaCl 3.5% and HCl Solutions

Sarra Laid, Mohamed-Elamine Djeghlal, and Hichem Salhi

Abstract− This paper assesses the ability of borided and non-borided Z80 WCrV 18-04-01 steel to resist corrosion by employing linear polarization resistance (LPR) and electrochemical impedance spectroscopy (EIS) methods. The steel samples were subject to boriding using the powder boriding method for different durations (1 hour, 2 hours, and 8 hours) at a temperature of 1223 K. Structural analysis of the borided steel surfaces revealed the presence of a double layer of FeB / Fe2B on the Z80 WCrV 18-04-01 steel. The properties of linear polarization resistance and electrochemical impedance spectroscopy were evaluated on the surfaces of both borided and non-borided steels amples by immersing them in corrosive solutions of 1M HCl (pH = 0.13) and 3.5% NaCl saline. The measurements of electrochemical impedance spectroscopy were analyzed over a 7-day exposure period in both corrosive solutions. Equivalent electrical circuits were used to model the impedance curves acquired for both the borided and non-borided steel samples. The findings from both electrochemical methods suggest that the boride layers formed on the surfaces of the steel provide effective protection against corrosive effects in both environments, but this protection is observed only during the first day of immersion.

***Keywords*− Steel, corrosion mechanism, corrosion resistance, EIS technique.**

I. Introduction

Boriding involves the thermal diffusion of boron into the surface layer of the part to be treated. The relatively small size and high mobility of boron atoms enable their diffusion into the substrate material, resulting in the formation of a metal-boride layer on the surface. This layer can be either single-phase or double-phase, depending on the conditions of the boriding process. Unlike many other surface treatments, boron can diffuse into most alloys and metals to produce hard boride layers. Boriding ferrous materials leads to the formation of a well-defined composition layer, which can be either a single phase (Fe2B) or a double phase (FeB/Fe2B). This formation occurs as a result of the boriding process. The determination of the case depth, which refers to the measurement of the thickness of each layer, holds significant importance in understanding the mechanical and chemical properties of borided steels. The thickness of the boride layer is influenced by various factors, including the temperature and duration of the boriding process, the chemical composition of the steel, and the concentration of boron in the vicinity of the sample surface [1, 2, 3].

Corrosion resistance is considered one of the properties significantly enhanced by boriding. In recent years, numerous studies have been conducted to evaluate the corrosion resistance of borided steels using alternative methods beyond conventional continuous and cyclic immersion corrosion tests [4, 5].

Materials with Surface coatings are frequently evaluated for their corrosion resistance using electrochemical echniques. In their study, Tavakoli and Mousavi Khoie [6] employed electrochemical techniques to evaluate the corrosion resistance of various borided steels types in a 3% NaCl solution. Impedance spectroscopy, an electrochemical test, was conducted for exposureperiods of 1 and 4 hours, as well as 2 to 4 days, and the results clearly demonstrated that the presence of boride layers significantly substantially enhanced the corrosion resistance within the tested range of boriding conditions. Similarly, in the study conducted by Jiang et al. [7], the corrosion behavior of low-carbon borided steels immersed in a 3.5% NaCl solution was evaluated using both the polarization method and electrochemical impedance spectroscopy (EIS) technique. However, the exposure duration of borided steels to the acidic solution was not specified in this particular study). The outcomes of the electrochemical tests indicated significant improvement in the corrosion resistance o flow-carbon borided steel due to the presence of Fe2B on its surface, in comparison to the untreated steel. Similar findings were observed in the boriding of AISI 316L stainless steel using the powder-pack method [5]. Electrochemical experiments were carried out to evaluate the corrosion behavior of the material under various conditions. Tafel extrapolation and linear polarization methods were employed in 1 mol/dm3 HCl, 1 mol/dm3 NaOH, and 0.9% NaCl solutions. The material was exposed to each solution for 1 and 168 hours at a temperature of 310 K. The existence of FeB/Fe2B layers on the surface of borided stainless steel resulted in a reduction of the estimated corrosion rate when exposed to the HCl solution. Conversely, the corrosion resistance of the borided stainless steel showed a decrease when exposed to the NaOH and NaCl solutions. A noticeable

Manuscript received June 12, 2023; revised December 18, 2024.

S. Laid and M.-E. Djeghlal are with Materials Science and Engineering Laboratory, Department of Metallurgy, Ecole Nationale Polytechnique, Algeria. (email: sara.laid@g.enp.edu.dz, dmlamine2015@gmail.com)

H. Salhi is with Corrosion and protection laboratory, research and development center, Dar El Beida, Algiers, Algeria. (email: salhihichem@gmail.com)

Digital Object Identifier (DOI): 10.53907/enpesj.v4i2.215

trend of increasing corrosion resistance in the borided samples was observed with longer exposure periods in all tested solutions. The polarization resistance technique is used to measure the corrosion resistance of materials by applying a small potential perturbation, E, to the working metal electrode. This perturbation is typically around ±10 mV from the open circuit potential value, and it is applied at a fixed potential scan rate. The current response obtained from the experiments is documented, and the linear polarization resistance (LPR) is defined as the ratio between the applied potential and the corresponding current response. It is important to note that LPR is inversely correlated with the corrosion current [8]. Electrical impedance spectroscopy (EIS) is widely utilized and highly effective technique in the field of corrosion studies. Typically, the Analysis of impedance measurements involves the utilization of equivalent electrical circuits consisting of passive elements such as resistors, capacitors, inductors and constant phase elements. These circuits are used to extract valuable information about the electrochemical properties of the system, especially those associated with corrosion and its underlying mechanisms.

II. Experimental Work

Material and boriding process

The powder-pack boriding process was conducted on steel Z80WCrV 18-04-01. Chemical composition of this steel is:0.81wt.%C, 0.17wt.%Mn, 0.23 wt.% Si, 0.019 wt.% S, 0.018 wt.% P, 0.08 wt.% Ni, 4.25 wt.% Cr, 0.09 wt.% Mo, 1.08 wt.% V, 17.60 wt.% W and 0.05wt.%Co. Prior to boriding, The specimens underwent a series of preparation steps to ensure their cleanliness and quality. Firstly, they were carefully polished to achieve a smooth surface. Subsequently, they were cleaned using an alcoholic solution and deionized water for a duration of 15 minutes, employing ultrasound to enhance the cleaning process. After cleaning, the samples were thoroughly dried and stored under clean room conditions to maintain their integrity. The specimens were enclosed within a sealed cylindrical container made of AISI 304 steel. This container contained a mixture consisting of 5% B4C, 5% NaBF4, and 90% SiC. The entire assembly was then subjected to a temperature of 1223 K for durations of 1 hour, 2 hours, and 8 hours. Upon completion of the heat treatment, the container was carefully extracted from the furnace and allowed to cool gradually until it reached room temperature. The borided specimens were cut into cross-sections and then embedded in Bakelite for metallographic preparation. The preparation process involved grinding the samples using SiCs and paper with grit sizes ranging from 240 to 4000. The depths of the boride layers were examined using a Scanning Electron Microscope (SEM) under clear field observation. The microstructure of the boride layers developed on the surface of Z80 WCrV 18-04-01 steel was verified using X-ray diffraction (XRD) with a standard 2θ-ω scan procedure. X-ray diffraction analysis was conducted using an XPERT PRO analytical instrument equipped with Cu $K\alpha$ radiation at a wavelength of 0.154 nm was employed for this analysis.

III. Results and Discussion

Optical microscopy (OM)

Micro-structural observations of transversal sections of borided samples of Z80 steel were performed by sing an optical microscope (TESCAN SEM instrument). It should be noted that the observations were carried out on transversal sections previously polished with an abrasive paper with granularity increasing from 240 to 4000 and a finishing with a diamond solution of 9 and 3µm. The obtained results are illustrated in figure 1.

(a)
(b)
(c)

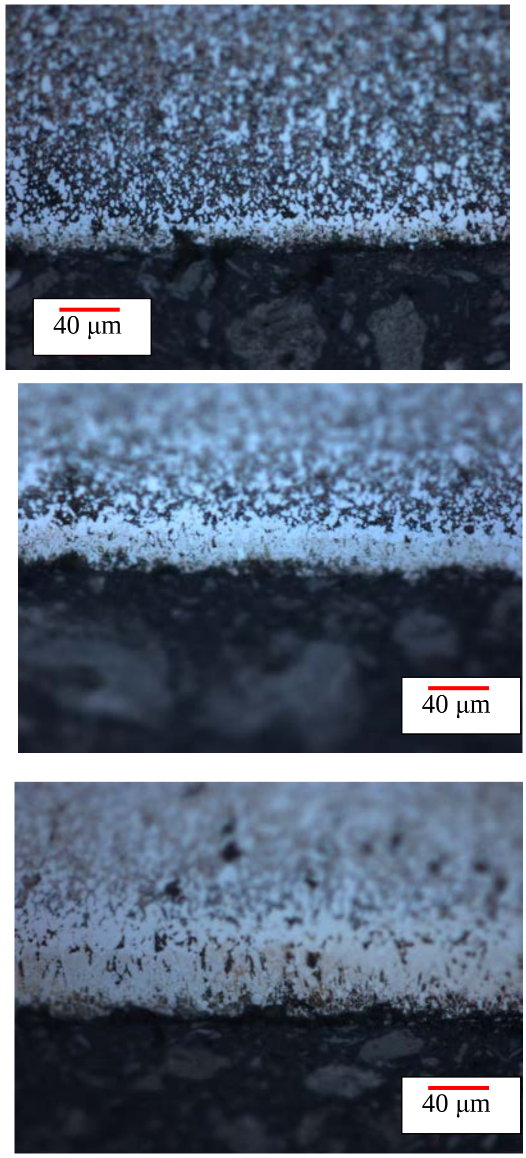

Fig.1: Optical micrographs carried out on transversal sections of borided samples at: (a) 1 hour, (b) 2 hours, (c) 8 hours.

X-Rays Diffraction (XRD)

The X-ray diffraction (XRD) technique was employed to analyze the microstructure of the boron layers formed on the surface of Z80 alloyed steel. The analysis included both non-borided samples and samples subjected to boriding for 1 hour, 2 hours, and 8 hours. The XRD analysis was conducted using an XPERTPRO analysis instrument with CuKα radiation, which has a wavelength of λ = 0.154 nm. The scanning procedure followed the regular 2θ-ω scanning pattern. The angular step size (2θ) during XRD digitization was 0.0260, and the temporal step size was 245.9154 seconds.

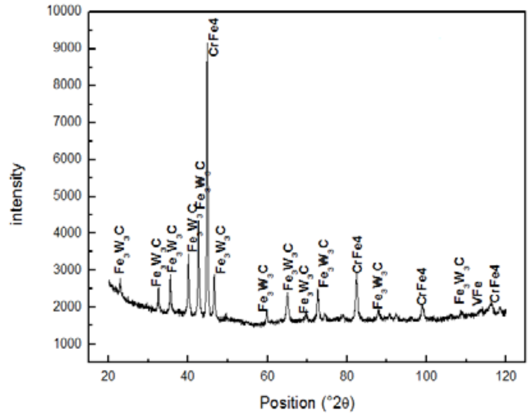

Fig 2: X-ray diffraction diagrams obtained on the steel surface without boriding

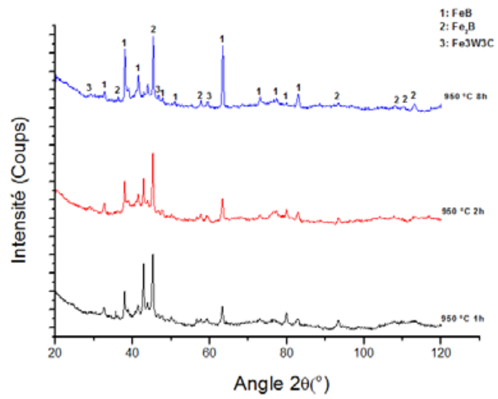

Fig.3: X-ray diffraction diagrams obtained on the surface of borided steel during 1 hour, 2 hours and 8 hours.

Micro-structural observations of transversal sections of borided Z80 steel were carried out by using a scanning electron microscope (SEM TESCAN instrument) to measure the depths of the layers of boron. It should be noted that the SEM observations were carried out on transversal sections previously polished with an abrasive paper of granularity increasing from 240 to 4000 and a finishing with a diamond solution of 9 and 3 µm. The obtained results are illustrated in figure 4.

(a)

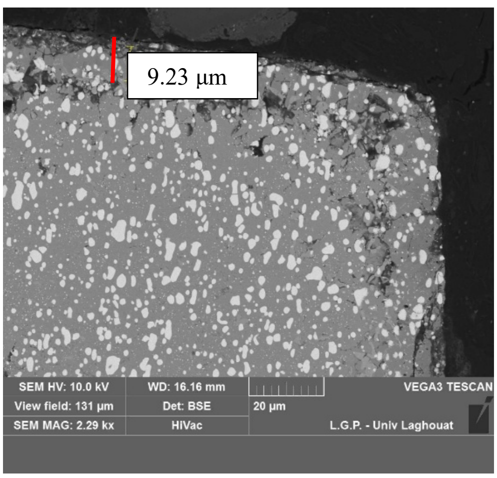

(b)

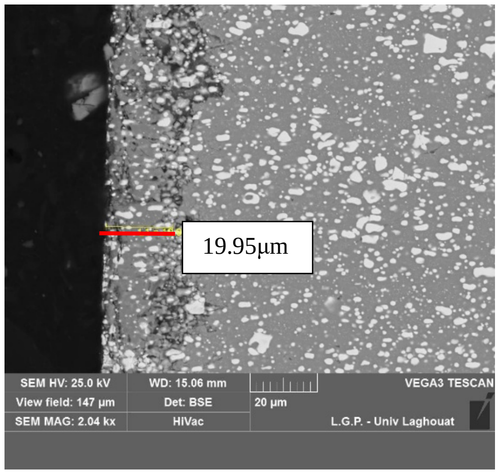

(c)

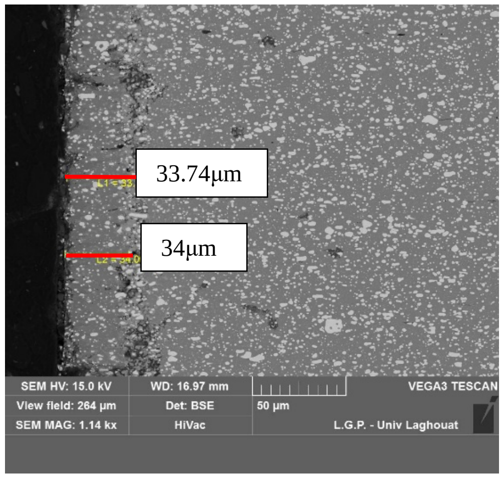

Fig.4: SEM micrographs carried out on transversal sections of borided samples at: (a) 1 hours, (b) 2 hours (c) 8 hours of treatment

Sectional views of Z80 borided steel at different times are shown in Fig 1 and Fig 4.The X-ray diffraction (XRD) pattern shown in Figure 3 confirms the presence of a saw-tooth morphology in the boron layer formed on the surface of Z80 steel. This morphology comprises a layer of Fe2B with isolated FeB teeth. Upon structural examination of the Surface, it was determinated that a FeB/Fe2B layer with a total thickness of 9.23 ± 0.69 µm was present after a duration of 1 hour of treatment. The presence of a saw-tooth morphology in the boron layer can be attributed to the enhanced diffusion pathways within the Fe2B crystal lattice, as suggested by previous research [9].After subjecting the Z80 steel to a boriding process for 2 hours, examinations of the surface revealed the presence of a FeB / Fe2B layer with a total thickness of 19.95 ± 1.10 µm. similarly, for Z80 steel borided for 8 hours, the surface examination indicated the presence of an FeB / Fe2B layer with a total thickness of 33.72 ± 1.78 µm.

A simple observation reveals a direct correlation between the thickness of the boron layer formed and the treatment temperature and duration. Spicifically, higher temperatures and longer treatment durations result in the formation of thicker layers.

The X-ray diffraction (XRD) analysis carried out on the surface of the borided steel Z80 (as shown in Figure 3) confirmed the presence of the FeB-Fe2B layer.

Electrochemical study

a) Corrosion in 3.5% NaCl solution

The effect of the addition of boron atoms on the corrosion behavior of borided Z80 steel was evaluated by performing electrochemical tests in 3.5% NaCl solution. No mechanical load was applied in this case. The measurement chain is used in potentio-dynamic mode, that is mean the current is measured following a scanning around the thermodynamic equilibrium potential. The scan rate was 0.5 mV / s. The impedance diagrams presented in this work were obtained by using "Volta-lab.PG.Z 402" impedance-measurement equipment. Data acquisition and treatment is done through Voltmaster and EClab software.

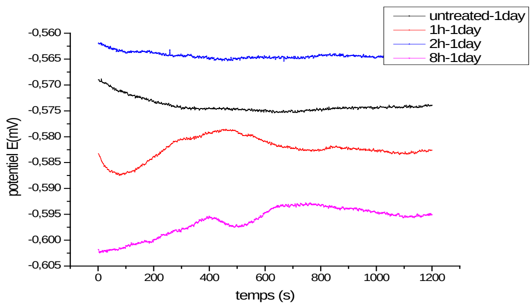

(a)

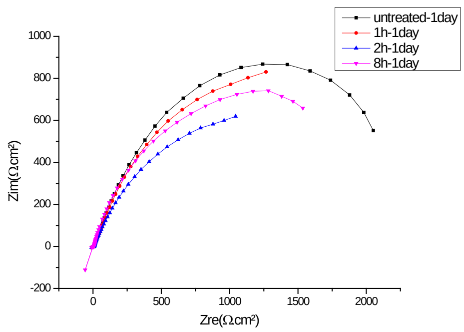

(b)

Fig.5: Evolution of the open-circuit potential, EOCP (a), and electrochemical impedance spectroscopy (Nyquist format) (b) of Z80 steel according to the immersion time in a 3.5% NaCl solution of non-borided and borided steel at 1, 2 and 8 hours.

The Nyquist plots obtained for borided and non-borided Z80 steel are shown in Fig.5, the results are summarized in the Table 1 and Fig.9. The corrosion resistance of Z80 steel has reached a maximum value of 2590 Ω.cm2 during the 08 hours of exposure to treatment based on linear polarization resistance testing (LPR). According to electrochemical impedance spectroscopy (EIS) the maximum value is 2580 Ω.cm2 for a treatment that lasted 8 hours, which confirms the tests of the linear polarization resistance.

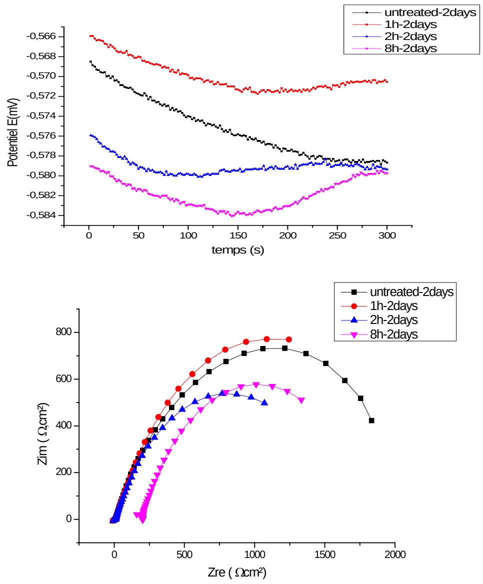

Fig.6: Evolution of the open-circuit potential, EOCP (a), and electrochemical impedance spectroscopy (Nyquist format) (b) of Z80 steel according to the immersion time in a 3.5% NaCl solution of non-borided and borided steel at 1h, 2h and 8h after 2 days of immersion in NaCl

The Nyquist plots obtained for the borided and non-borided Z80 steel, which remained in the NaCl solution for 2 days, are shown in Fig 6, the results are summarized in the Table 2 and Fig 10. The corrosion resistance of Z80 steel reached a maximum value of 1370 Ω.cm2 for untreated steel according to linear polarization resistance tests and according to electrochemical impedance spectroscopy the maximum value is 1310 Ω.cm2, which confirms the linear polarization resistance tests. So, it is concluded that the untreated steel has a better resistance against corrosion, and this is due to the degradation of the surface layer (FeB / Fe2B) which leaves a rough surface (the dendritic form of the double FeB layer / Fe2B) which causes corrosion.

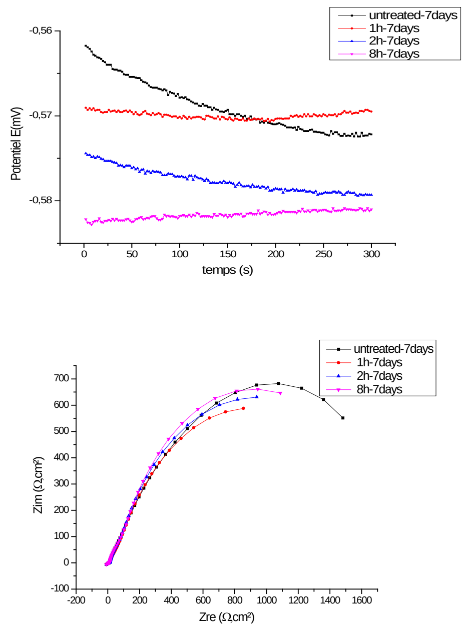

Fig.7: Evolution of the open-circuit potential, EOCP (a), and electrochemical impedance spectroscopy (Nyquist format) (b) of Z80 steel according to the immersion time in a 3.5% NaCl solution of non borided steel and borided at 1h, 2h and 8h after 7 days of immersion in NaCl.

The Nyquist plots obtained for borided and non borided Z80 steel are shown in Fig.7, the results are summarized in the Table 3 and Fig 11. The corrosion resistance of Z80 steel reached a maximum value of 1240 Ω.cm2 for untreated steel based on linear polarization resistance tests. According to electrochemical impedance spectroscopy the maximum value is 1200 Ω.cm2 also for untreated steel, which confirms the linear polarization resistance tests.

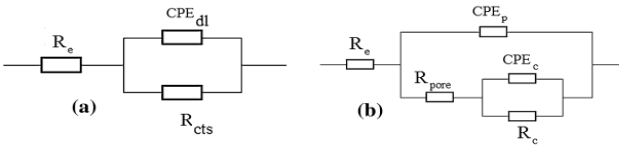

Fig.8: EECs used for numerical fitting of impedance data: (a) Z80 non-borided, and (b) Z80 borided steel

Table 1: Results of electrochemical impedance spectroscopy (EIS) in 3.5% NaCl solution

Non-borided steel	R_e $[\Omega.cm^2]$	R_{cts} $[\Omega.cm^2]$	CPE_{dl} $[\mu F/ cm^{-2}]$	N_{cts}			
Z80 WCrV18-04-01	6.707	1220	121.4	0.7873			
Borided steel Z80 WCrV18-04-01	R_e $[\Omega.cm^2]$	R_{pore} $[\Omega.cm^2]$	CPE_p $[\mu F/ cm^{-2}]$	N_{pore}	R_c $[\Omega.cm^2]$	CPE_c $[\mu F /cm^2]$	N_c
1 hour	5.92	1580	365	0.6465	9.776	567	0.7542
2 hours	5.44	1520	681	0.5251	40.7488	385.4	0.7875
8 hours	1.422	2580	445.2	0.7317	329.1	587	0.6023

Linear polarization resistance (LPR) gave the following results:

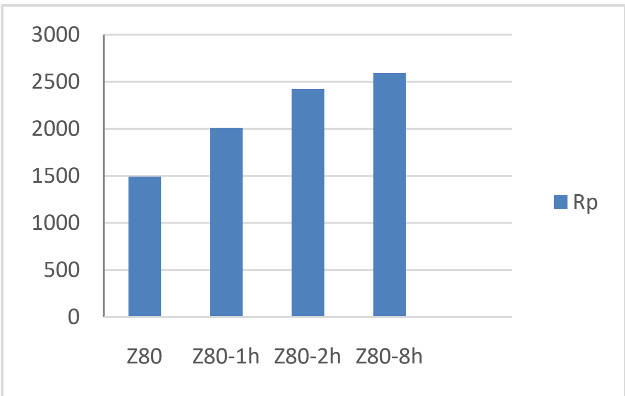

Fig.9: Evolution of the polarization resistance of Z80 steel immersed in a 3.5% NaCl solution of non-borided and borided steel at 1, 2 and 8 hours.

Table 2: Results of electrochemical impedance spectroscopy (EIS) after 2 days of immersion of the samples in the NaCl solution

Non-borided steel	$R_e[\Omega.cm^2]$	$R_{cts}[\Omega. cm^2]$	$CPE_{dl}[\mu F/ cm^{-2}]$	N_{cts}			
Z80 WCrV18-04-01	5.78	1310	26950	0.8163			
Borided steel Z80 WCrV18-04-01	R_e $[\Omega. cm^2]$	R_{pore} $[\Omega. cm^2]$	CPE_p $[\mu F/ cm^{-2}]$	N_{pore}	R_c $[\Omega .cm^2]$	CPE_c $[\mu F / cm^2]$	N_c
1 hour	6.63	1030	232	0.9389	443.9	873.4	0.7427
2 hours	6.30	1150	30.65	1	10.59	385.4	0.6914
8 hours	126.08	1100	902.2	0.7504	12.09	0.5086	0.7115

After 2 days of immersing the samples in the NaCl solution, the linear polarization resistance (LPR) gave the following results:

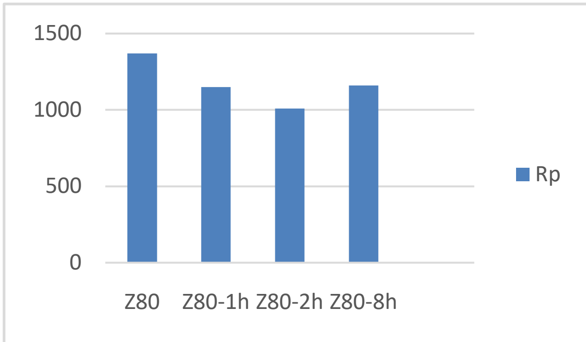

Fig.10: Evolution of the polarization resistance of Z80 steel immersed in a 3.5% NaCl solution of non borided and borided steel at 1h, 2h and 8h after 2 days of immersion in NaCl

Table 3: Results of electrochemical impedance spectroscopy (EIS) after 7 days of immersion of the samples in the NaCl solution

Non-borided steel	R_e $[\Omega.cm^2]$	R_{cts} $[\Omega. cm^2]$	CPE_{dl} $[\mu F/ cm^{-2}]$	N_{cts}			
Z80 WCrV18-04-01	7.22	1200	386.3	0.7282			
Borided steel Z80 WCrV18-04-01-	R_e $[\Omega.cm^2]$	R_p $[\Omega.cm^2]$	CPE_{pore} $[\mu F/ cm^{-2}]$	N_{pore}	R_c $[\Omega.cm^2]$	CPE_c $[\mu F/cm^2]$	N_c
1 hour	7.4624	1010	653.5	0.8358	138.56	963.7	0.7085
2 hours	6.83	1010	587.5	0.8684	176.32	909.6	0.7331
8 hours	10.848	998	937.6	0.8255	108.73	0.4349	0.9074

After 7 days of immersing the samples in the NaCl solution, the linear polarization resistance (LPR) gave the following results

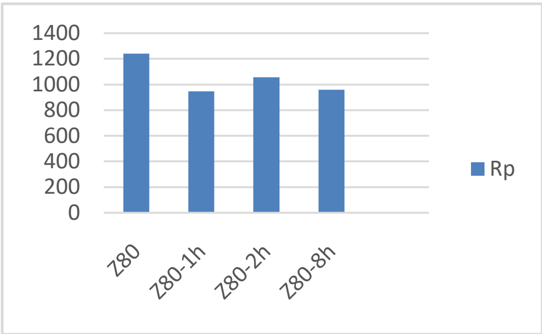

Fig.11: Evolution of the polarization resistance of Z80 steel immersed in a 3.5% NaCl solution of non-borided and borided steel at 1h, 2h and 8h after 7 days of immersion in NaCl

From Fig.7, we notice that the potential of Z80 steel decreases with the increase of the boriding treatment time, it means that steel becomes less noble, thus reducing their resistance to corrosion (Fig 11). This tendency can be attributed to the high porosity content and micro-cracks formed in the FeB and Fe2B layers as well as the rough appearance of the borided layer which is dependent on saw-tooth in the FeB-Fe2B inter-phase [8]. It should be noted that the aggressive Cl- ions can diffuse into the cracks of the boron layers, reaching the base metal, resulting in film degradation, dissolution corrosion of the base steel and formation of ferrous ions [8]. The reaction of OH- produced by the reduction of rust on the coating surface [9], accordingly to the electrochemical process:

$$2Fe + O_2 + H_2O \Longrightarrow 2Fe(OH)_2$$

Re [Ω.cm2]: electrolyte resistance;

Rcts[Ω.cm2]: resistance of the electron charge transfer of the substrate;

Rpore[Ω.cm2]: resistance of the pore ;

Rc[Ω.cm2]: resistance of the boride layer;

CPEp[μF/ cm-2]: capacitance of the pore;

CPPEdl[μF/ cm-2]: electrochemical double layer of the substrate;

CPEc[μF/cm2]: capacitance of the boride layer.

b) Corrosion in HCl 1M solution

The corrosion assessment for both treated and non-treated Z80 steel immersed in a 1M HCl solution was conducted through two methods: monitoring the open circuit potential (EOCP) over time, and carrying out the EIS technique by using an electrochemical workstation of the “Volta-lab.PG.Z 402” brand.

The experiments were conducted at room temperature with the open circuit potential (EOCP) measured using a conventional three-electrode cell configuration. The cell consisted of a cylindrical platinum rod serving as the counter electrode, an Ag / AgCl mini electrode acting as the reference electrode, and the working electrode placed horizontally at the bottom of the cell. The working electrode was affixed to an acrylic cylinder, exposing a surface area of 1 cm2. Before initiating the electrochemical testing, the samples were submerged in the electrolyte solution for approximately 30 minutes to allow for the stabilization of the open circuit potential (EOCP) at room temperature. The electrochemical impedance spectroscopy (EIS) measurements were carried out over a period of 7-days while the samples were exposed to the acid solution. In this technique, a sinusoidal input signal E0 Sin (xt) was applied to the electrode system at a specific frequency, x. The measurements were conducted within a frequency range of 1 MHz to 10 MHz, using a sinusoidal alternating potential disturbance with amplitude of 10 mV (rms). To estimate the electrochemical parameters, the experimental data was fitted with a suitable Constant Phase Element CPE model.

(a)

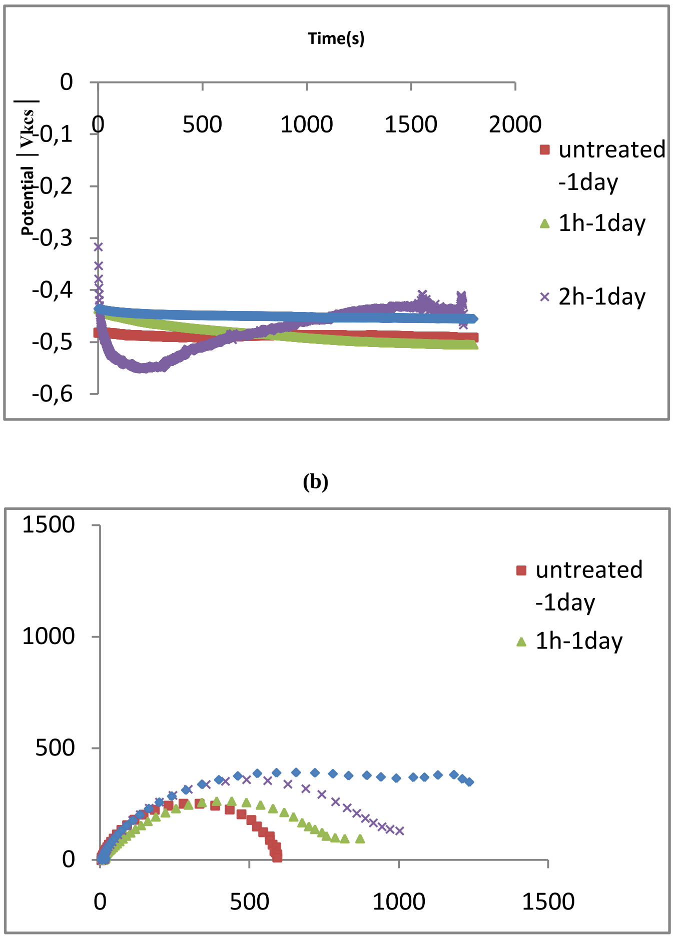

Fig.12: Evolution of the open-circuit potential, EOCP (a), and electrochemical impedance spectroscopy (Nyquist format) (b) of Z80 steel according to the time of immersion in a HCl 1M solution of non borided and borided steel at 1 hour, 2 hours and 8 hours.

Figure 12 displays the Nyquist plots obtained for both treated and non-treated Z80 steel, while table 4 and figure 14 summarize the results. The corrosion resistance of Z80 steel reached a maximum value of 1083 Ω.cm2 during the 08 hours of exposure to treatment based on electrochemical impedance spectroscopy tests. The increase in corrosion potential values for Z80 borided steel proves that the layer of boron formed on the surface of the steel protects the steel against corrosion. By analyzing the data presented, the piece of steel immersed in a solution of hydrochloric acid for one hour was subjected to boriding at 950 °C, for boriding for 8 hours, it presents the lowest corrosion rate.

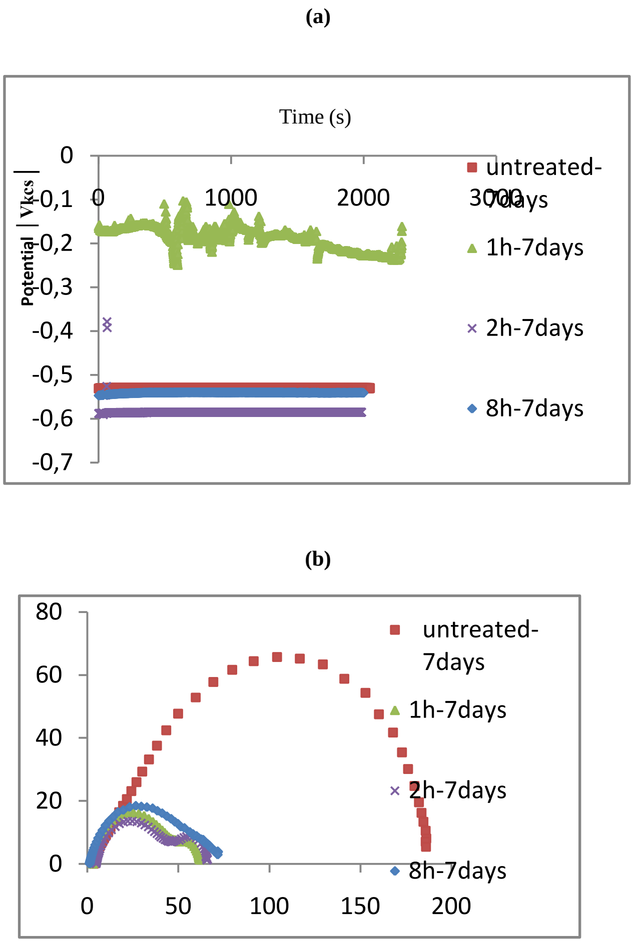

Fig.13: Evolution of the open-circuit potential, EOCP (a) and electrochemical impedance spectroscopy (Nyquist format) (b) of Z80 steel according to the time of immersion in a HCl 1M solution of non borided and borided steel at 1 hour, 2 hours and 8 hours after 7 days of immersion in HCl.

Figure 13 displays the Nyquist plots obtained for both treated and non-treated Z80 steel, which remained in the 1M HCl solution for 7 days, the results are summarized in the Table 5 and Fig 15. Based on electrochemical impedance spectroscopy tests, the untreated Z80 steel exhibited a corrosion resistance with a maximum value of 142 Ω.cm2. Therefore, it is concluded that the untreated steel has a better resistance against corrosion, and this is always due to the degradation of the surface layer (FeB/Fe2B) which leaves a rough surface (the dendritic form of the double layer FeB/Fe2B) which causes corrosion.

Table 4: Results of electrochemical impedance spectroscopy (EIS) in HCl 1M solution

	R_s[Ω.cm^2]	R_{dl}[Ω.cm^2]	$Q_{dl}10^{-3}$ [F.cm^2]	N
Z80	9,1565	594.94	0.0005	0.89281
Z80-1 hour	8.1834	790.97	0.00050472	0.74023
Z80-2 hours	5.6705	930.85	0.0005	0.84092
Z80-8 hours	5.3358	1083	0.00030028	0.79513

Linear polarization resistance (LPR) gave the following results

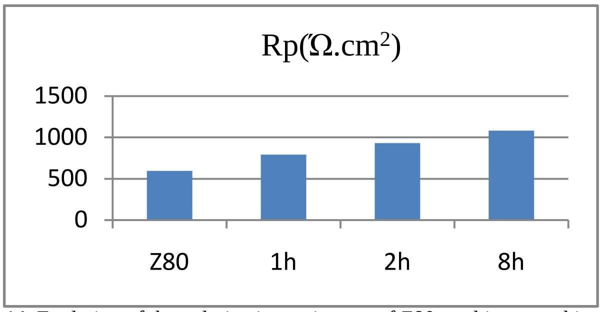

Fig.14: Evolution of the polarization resistance of Z80 steel immersed in a HCl 1M solution of non-boraided and borided steel at 1 hour, 2 hours and 8 hours.

Table 5 : Results of electrochemical impedance spectroscopy (EIS) after 7 days of immersion of samples in HCl 1M solution

	R_s [Ω.cm^2]	R_{dl} [Ω.cm^2]	$Q_{dl}10^{-3}$ [F.cm^2]	n	P
Z80	35.747	142.85	0.0005	0.84384	0.0005
Z80-1 hour	3.1884	57.644	5.6924 E-05	0.61679	0.0005
Z80-2 hours	4.5478	40.734	/	0.76684	0.00021486

After 7 days of immersing the samples in the HCl solution, the linear polarization resistance (LPR) gave the following results:

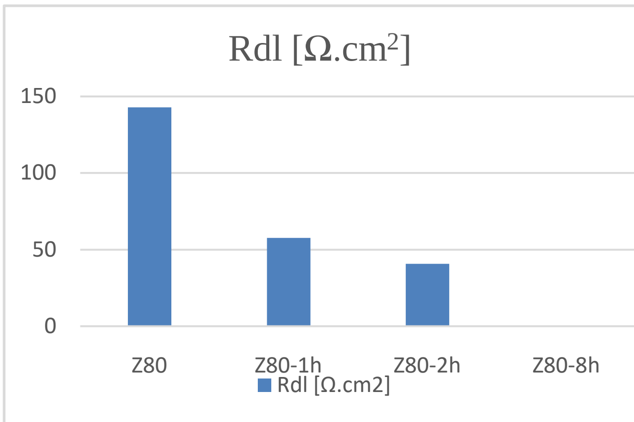

Fig.15: Evolution of the polarization resistance of Z80 steel immersed in a HCl 1M solution of non-borided and borided steel at 1h, 2h and 8h after 7 days of immersion in HCl.

The double boron layer (FeB/Fe2B)has thermal expansion coefficients, which lead to the formation of compressive constraints leading to the creation of cracks. This type of defect allows chloride ions to penetrate through the formed boron layer thus migrating to the surface of the steel. Chloride ions diffuse through cracks in boron layers formed on the steel surface and form ferrous ions. These react with hydroxide ions to form iron hydroxides. The following equations summarize the recommended phenomenon:

$$Fe + 2Cl- + 4H_2O \longrightarrow FeCl_2 + 4H_2O + 2e-$$

$$O_2 + 2H_2O + 4e - -\longrightarrow 4OH-$$

$$FeCl_2 + 4H_2O + 2OH- \longrightarrow Fe(OH)_2 + 2Cl- + 4H_2O$$

$$4Fe(OH)_2 + 2H_2O + O2 \longrightarrow 4Fe(OH)_3$$

Rs [Ω.cm2]: Resistance of the solution;
Rdl [Ω.cm2]: Load transfer resistance;
Qdl10-3 [F.cm-2]: Constant phase element of the double layer / constant phase element of the deposit;
n: The coefficient of frequency dispersion (It represents a measure of surface inhomogeneities).

c) Comparison between the behavior of Z80 steel in a HCl 1M solution and 3.5% NaCl

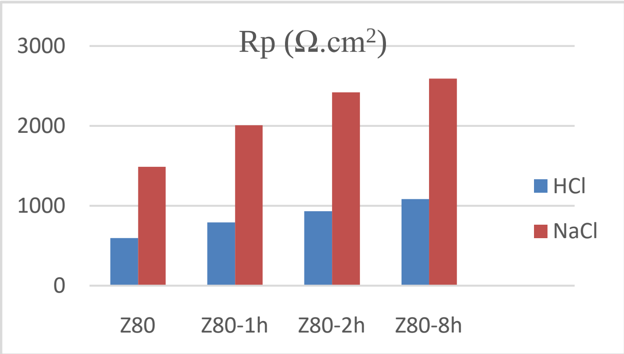

Fig.16: Evolution of the polarization resistance of Z80 steel immersed in a HCl 1M and 3.5% NaCl solution of non-borided and borided steel at 1 hour, 2 hours and 8 hours.

Note that the polarization resistance changes in the same way in both solutions, it increases with the increase of the surface treatment time. Accordingly to the analyzes of plots obtained from polarization resistance and electrochemical EIS tests, corrosion resistance increases with increasing boriding treatment time.

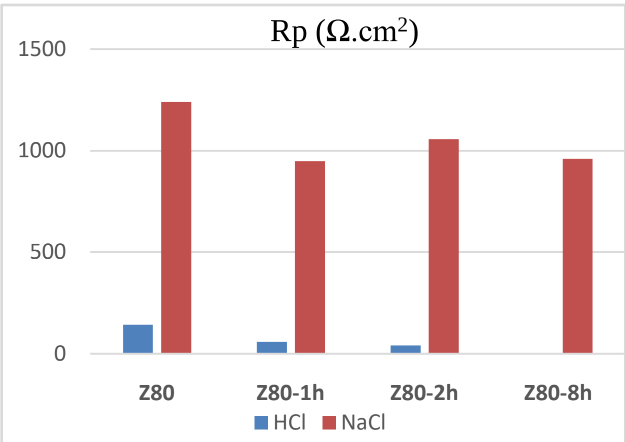

Fig.17: Evolution of the polarization resistance of Z80 steel immersed in a HCl 1M and 3.5% NaCl solution of non-borided and borided steel at 1 hour, 2 hours and 8 hours after 7days of immersion in the solutions.

From Figure 16 and Figure 17, we can see that the polarization resistance changes in the same way in both NaCl and HCl solutions. Also, Z80 steel resists better in saline solution than in acidic solution. The formation of a bilayer (FeB/ Fe2B) leads to the formation of cracks increasing the possibility for chloride ions to come into contact with the steel surface, accelerating the corrosion phenomenon. Corrosion resistance decreases with increasing sample immersion time in both 3.5% NaCl and HCl 1M solutions, which allows us to say that the surface layer of the samples deteriorates over time of exposure.

IV. Conclusion

Based on the results obtained, we can conclude with the following points:

- Aggressive ions, such as chloride ions (Cl-), have the ability to permeate through protective layers and initiate corrosion. These ions diffuse into the pores and eventually reach the steel substrate.
- Electrochemical Impedance Spectroscopy (EIS) is a highly effective and non-destructive technique used to investigate corrosion and various electrochemical phenomena occurring within metal samples.
- The corrosion rates of borided steel are typically influenced by the presence of micro-cracks and porosities within the coating. These porosities have a detrimental effect on the coating quality and significantly decrease its corrosion resistance.
- The presence of porosities within the study material can compromise the integrity of interfacial regions, creating vulnerable areas that can facilitate failure. These local defects can establish a direct pathway for corrosive environments to reach the boride layers.

References

[1] L.G. Yu, K.A. Khor, and G. Sundararajan Boriding Mild Steel Using the Spark Plasma Sintering (SPS) Technique, Surf. Coat. Technol. 157, p 226–230. (2002)
[2] L.A.Arteaga-Hernandez, C.A.Cuao-Moreu, C.E.Gonzalez-Rivera, M.Alvarez-Vera, J.A.Ortega-Saenz, M.A.L.Hernandez-Rodriguez 2021 Study of boriding surface treatment in the tribological behavior of an AISI 316L stainless steel. Wear. 477 203825. (2021)
[3] Bülent Aktaş, Mehmet Toprak, Adnan Çalık, and Ali Tekgüler, Effect of pack-boriding on the tribological behavior of Hardox 450 and HiTuf Steels, Rev. Adv. Mater. Sci.; 59p314–321(2020)
[4] I. Campos, M. Palomar, A. Amador, R. Ganem, and J. Martinez, Evaluation of the Corrosion Resistance of Iron Boride Coatings Obtained by Paste Boriding Process, Surf. Coat. Technol., 201, p 2438–2442. (2006)
[5] Y. Kayali, A. Buyuksagis, I. Gunes, and Y. Yalcin, Investigation of Corrosion Behaviors at Different Solutions of Boronized AISI, 316 L Stainless Steel, Prot. Met. Phys. Chem. Surf., 49, p 348–358. (2013).
[6] H.Tavakoli and S.M. Mousavi Khoie, An Electrochemical Study of the Corrosion Resistance of Boride Coating Obtained by Thermo-reactive Diffusion, Mater. Chem. Phys., 124, p 1134–1138. (2010)
[7] J. Jiang, Y. Wang, Q. Zhong, Q. Zhou, and L. Zhang, Preparation of Fe2B Boride Coating on Low-Carbon Steel Surfaces and its Evaluation of Hardness and Corrosion Resistance, Surf. Coat. Technol , 206, p 473–478. (2011)
[8] J. Fontana, Corrosion Engineering 1986, 3rd ed., Mc Graw-Hill, New York,NY. (1986)
[9] Dybkov, R. Siderko, L.V. Goncharuk, V.G. Khoruzha, and A.V.Samelyuk, Microstructure, Growth Kinetics, and Abrasive Wear Resistance of Boride Layers on Fe-30% Cr Alloy, Powder Metall. Met. Ceram., 51, p 518–530. (2013)

Sarra Laid is a PhD student at Materials Science and Engineering Laboratory, Department of Metallurgy, Ecole Nationale Polytechnique, Algiers, Algeria.

Mohamed-Elamine Djeghlal is Professor at Department of Metallurgy, Ecole Nationale Polytechnique, Algiers, Algeria. His main research areas are: Thermodynamics, Material Characterization, Heat Treatment, and Crystallization.

Hichem Salhi is research fellow at Corrosion and protection laboratory, research and development center, Dar El Beida, Algiers, Algeria.

Comprehensive Study, Simulation and Analysis of the Fault effects on the Performance of Different Photovoltaic Array Configurations

Faiza Belhachat and Cherif Larbes

Abstract−Photovoltaic (PV) system fault analysis is crucial for improving the safety and efficiency of PV systems. Faults not only degrade performance but also negatively impact system longevity. Power output can be significantly affected by configuration, PV technology, partial shading (PS), and other operating conditions. Therefore, an accurate fault analysis requires studying the impact of faults on the performance of different photovoltaic array configurations (PVACs). The article conducts a detailed study and analysis of faults such as partial shading, bypass diode, open circuit, short circuit, line-to-ground, line-to-line, and degradation. To analyze the combined effecton different configurations,the case of multiple faults occurring simultaneously, with varying irradiance is also considered. The PVACs examined include Series (S), Series-Parallel (SP), Total-Cross-Tied (TCT), Honey-Comb (HC) and Bridge-Linked (BL). A 6x4 PV array was modeled and simulated under various scenarios to assess their impact on the performance of different PVACs and to determine the most suitable configuration for maximizing power output under these conditions. The obtained simulation results are compared and discussed. It has beenfound that using appropriate PVAC can minimize the impact of faults. The results show the superiority of S and SP PVACs, which provide the best performance in most fault scenarios. Furthermore, the TCT PVAC is no longer suitable in the case of a fault, unlike in the case of partial shading, where it outperforms the other PVACs in several situations.

Key words− Fault, photovoltaic, configuration, performance, effect.

I. Introduction

In recent years, the number of photovoltaic (PV) solar power plants has steadily increased worldwide. In fact, PV power generation systemsoffer undeniable advantages, including long life, low aging effects, low maintenance, low operating costs and robustness. However, various types of failures can occur in PV systems requiring testing and performance measurements of PV modules during maintenance work. Additionally, these failuressignificantly reduce the power generated by the PV array, which inevitably leads to a reduction in theefficiency and performance of the entire system. All system components whether modules, DC circuits or inverters can be a source of interference. The main faults of PV modules that can significantly affect the efficiency of power generation include cell failure, dirt, broken glass, delaminationand discoloration, hot spots and bypass diode failure [1-5]. The shading fault is a common fault that can occur in PV systems.In fact, changing the connections of the modules within a PV array using S, SP, HC, BL and TCT connections is one of the methods to lessen the effects of partial shading (PS) [6]. Experimental investigations on different PV array configurations (PVACs) have shown that the TCT configuration has the lowest mismatch loss in the case of PS compared to the other PVACs [6]. Shading is a special case of the mismatch defect as it reduces the amount of sunlight reaching the cells, leading to a reduction in power generation across the array. However, other faults can appear in a configuration even inthe presence of PS affectingthe PVACsperformance [7-9].

As a result, it is necessary to study and analyze these defects and their impact on the behavior of the different PVACs in order to identify the most resilient configurations that perform best under faulty conditions. While the performance of the different PVACs under partial shading has been widely studied in the literature [6], the impact of various faults on the efficacy of the existing configurations has not been thoroughlyinvestigated in previous works, a gap that this study aims to address.Thus, studying theseimpactsis essential for analyzing the performance of each configuration and selecting the onemost suitable to ensure optimal performance in the case of faults. This paper provides a comparative analysis and evaluation of faults such as partial shading, bypass diode failure, open circuit, short circuit, line to ground, line to line and degradation across various configurations including S, SP, BL, HCand TCT.The effect of multiple faults is also examined. A comparison of the performance results shows that selecting the appropriate configuration under faulty conditions can improve the system's efficiency. The study was conducted using an array of 24 PV modules organized in six rows and four columns, modeled in Simulink. The main contributions of this paper are:

- An increase in energy production is accomplished by using the appropriate PVAC for various fault scenarios.

- Five configurations have been tested including S, SP, TCT, HC and BL in order to choose the most appropriate depending on the fault encountered.

- Various faults such as partial shading, bypass diode failure, open circuit, short circuit, line to ground, line to line and degradationwere considered in this study.

Manuscript received March 9, 2024; revised December 19, 2024..

F. Belhachat, and C.Larbes are with Electonics Department of Ecole Nationale Polytechnique (e-mail: faiza.belhachat@g.enp.edu.dz, cherif.larbes@g.enp.edu.dz)

Digital Object Identifier (DOI): 10.53907/enpesj.v4i2.261

- The case of multiple failuresinPVarray interconnections was also examined.

-It has been demonstrated that the S and SP PVACs are the most appropriate in the case of faults and that the performance of the TCT PVACs has been severely degraded under these fault conditions.

- Assessing the impact of each configuration, which allows for the systematic selection of the most resilient configuration to failures, minimizing losses.

The paper is organized as follows: Section 2 presents the model of the PV module. In Section 3, the modeling and simulation of different PVACs are presented. Section 4, describes the different faults that can occur on PV modules. Section 5 presents the study, analysis and simulation of the impact of faults on different PVACs. The results obtained under faulty conditions are discussed in Section 6. The conclusion is provided in Section 7.

II. PV Module Modeling

To simulate the functioning of a solar PV cell, it is necessary to establish its electronic model. Solar PV modules consist of several solar cells connected in series. A PV array can be created by combining multiple solar panels. In this section, a one-diode solar cell model for simulatingPV arrays with dimensions N_sx$N_p$is described. The equivalent electrical circuit of the model based on a single diode is depicted in Fig.1.

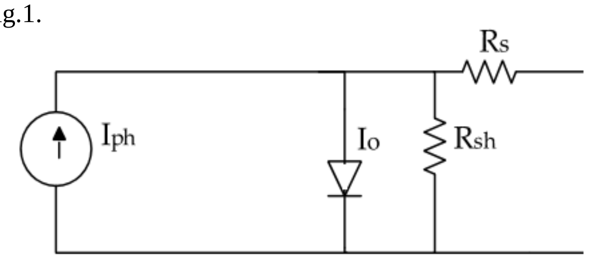

Fig.1: Equivalent circuit of PV solar cell.

A PV panel consists of N_p and N_s solar cells arranged in parallel and series, respectively. The resulting PV module current is shown in equation (1):

$$I = N_p\left(I_{pv} - I_0\left[\exp\left(\frac{V + I_{pv}R_s}{V_t N_s} - 1\right)\right]\right) - \left(\frac{V + I_{pv}R_s}{V_t N_s} - 1\right) \qquad (1)$$

Where I_0 is the reverse saturation current, R_s is the series resistance and R_p is the parallel resistance, whereas V_t represents the thermal voltage at any temperature given by:

$$V_t = \frac{N_s KT}{q} \qquad (2)$$

K is the Boltzmann constant equal to 1.3805 x 10-23, *q* is the electron's charge constant of 1.9×10^{-19} C and *T* is the temperature at STC. A single 150W PV module is used to simulate a 6x4 PV array using Matlab/Simulink for different configurations. Table 1 contains the specifications of the PV module under consideration. The model parameters used are shown in Table 2.

Table.1
Technical details of the CA Solar MS-150M PV module.

Characteristics	**Value**
Maximum Power (W)	149.89
Cells per module (N_{cell})	72
Open circuit voltage V_{oc} (V)	43.2
Short-circuit current I_{sc} (A)	4.87
Voltage at maximum power point V_{mp}(V)	34.4
Current at maximum power point I_{mp} (A)	4.36
Temperature coefficient of V_{oc} (%/deg.C)	-0.39718
Temperature coefficient of I_{sc} (%/deg.C)	0.060411

Table.2
Model parameters for the CA Solar MS-150M PV module

Model parameters	**Value**
Light-generated current I_L (A)	4.8982
Diode saturation current I_0 (A)	$5.5248e^{-10}$
Diode ideality factor	1.0227
Shunt resistance Rsh (ohms)	131.2651
Series resistance R_s (ohms)	0.75917

Fig. 2 shows the I-V and P-V characteristics of the CA Solar MS-150M PV module.

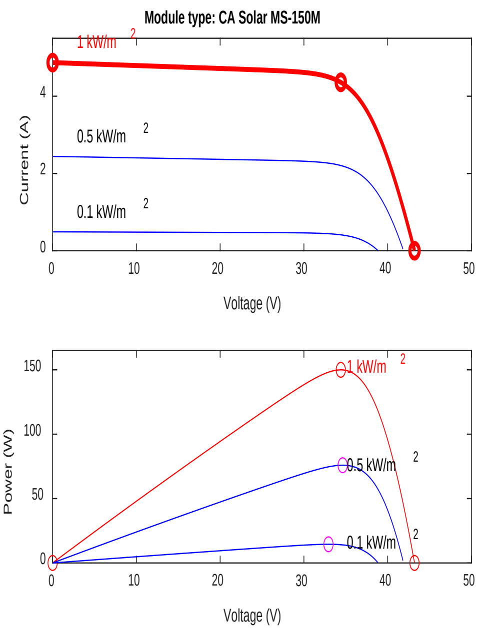

Fig.2:I-V and P-V characteristics of the CA Solar MS-150M PV module.

III. Modeling And Simulation Of Pv Array Configurations (PVACs)

The PVAC refers to the way in which the PV modules are connected inside the array. Many connectivity topologies for PV modules are suggested in the literature, including S, SP, TCT, HC and BL connections. The S and SP topologies are the basic arrangements for connecting PV modules. The PV array's voltage can be raised thanks to the modules' series coupling. In the P connection, the total current is the sum of all the currents. The SP connection is the most popular connection type, which is made by connecting the PV modules in series to form a string or branch (to achieve the necessary voltage required). These strings are connected in parallel to increase the total output current. In the TCT configuration, the modules are first connected in parallel to form parallel connection groups; these will then be connected in series. Therefore, the PV modules are fully connected in this type of coupling. The HC and BL topologies reduce the number of connections between modules of adjacent strings by about half, compared to the topology TCT, which considerably reduces the quantity and time of wiring from the PV array.

Fig 3 depictsillustrative schemefor the different PVACs that are intended for the analysis of the impact of faults on PV arrays, including S, SP, TCT, BL and HCinterconnections.Fig 4 shows the Simulink model of TCT PVAC.

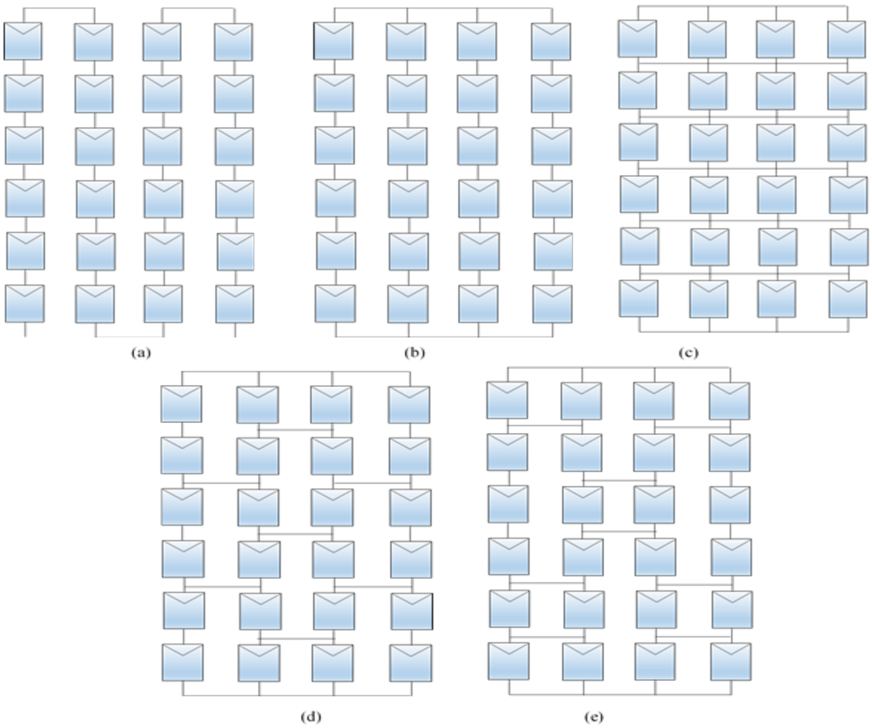

Fig.3: Different PVACs: (a) S. (b) SP. (c) TCT. (d) BL. (e) HC.

Fig.4: A modeling of a 6x4 TCT PVAC.

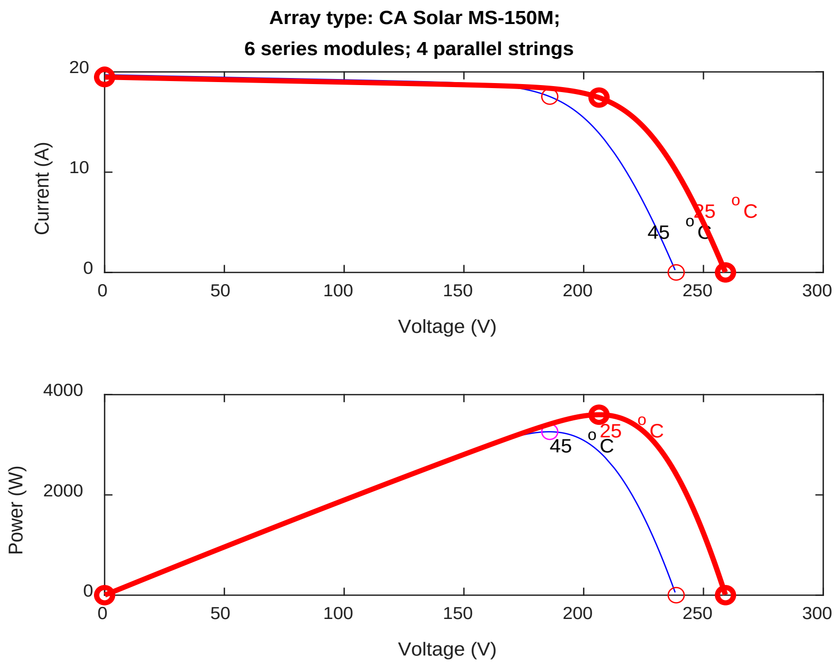

Fig.5**:** P-V and I-V characteristics of the TCT PVAC under uniform conditions.

Fig.5shows the P-V and I-V characteristics of the TCT configuration under uniform conditions. All PVACs exhibit the same characteristics under these operating conditions. Table 3 presents the maximum power, voltage and current for different PVACsunder standard test conditions (STC).

Table. 3
Power, voltage and current of different PVACs.

Configuration	S	SP	TCT	HC	BL
Power (W)	3600	3600	3600	3600	3600
Voltage (V)	827	206.1	206.1	206.1	206.1
Current (A)	4.353	17.47	17.47	17.47	17.47

IV. Considered Faults

In this section, we provide a brief description of the faults considered in this study.

A. Partial shading

Shading happens when a solar panel part is blocked by an object such as a tree or building, hence reducing the light quantity received by the solar cells. Because most of the cells are in series, if a part of the panel becomes shaded, then the whole module produces less power. This may also lead to hot spots that damage the cells over time [10].

B. Bypass diode failure

The fault of the bypass diode occurs when the bypass diode in a solar module fails to function correctly. Normally, the working principle of bypass diodes is to protect the panels: they shield against partial shading or cell failure. With a faulty or shaded cell, a bypass diode provides an alternate path for current so that it can bypass the affected cell, preventing damage to the entire panel. A bypass diode fault removes this protection, leading to significant energy losses, hot spots, and potential damage to the solar cells or even the cover panel, which reduces the overall efficiency of the PV system [10].

C. Open circuit

An open circuit happens when there is a break in the circuit, thus current flow cannot take place. It can result from poor connections, disconnected cable, or defective solar module. The inability of the system to produce power is primarily because there is no way the current will flow between the panels and the inverter. Power loss is hence total [10].

D. Short circuit

A short circuit occurs when there is a direct connection between two conductors, causing excessive current to flow uncontrolled.The occurrence could be from poor wiring, physical damages to the solar cells, or internally damaged components. Therefore, a short circuit results in extra current that may flow and damage components, perhaps even damage the section of the panel irreversibly or even reduce its efficiency, which can be a fire hazard [10].

E. Degradation fault

A degradation fault in a photovoltaic module refers to the gradual decline in the panel's performance over time. As a result, the module is no longer able to produce power at its original capacity. This can be caused by several factors, which, over time, lead to a loss in efficiency [10].

F. Line-to-line fault

A line-to-line fault occurs when there is a short-circuit connection between two live conductors of a system. In this case, abnormal high current flows between the two lines but does not circulate to perform useful work. This could damage cables, circuit breakers, or inverters. Such faults can lead to power production shutdowns in a PV system and increase the risk of fire or equipment overheating, thus compromising safety and system performance [10].

G. Line-to-Ground Fault

A line-to-ground fault occurs when an energized conductor comes into contact with the ground or an earthed metallic surface. The risks involved include energy loss, equipment malfunction, and danger to life from electric shock due to leakage current to the earth. In the PV system, this fault can cause disturbances that require the intervention of protective devices, such as circuit breakers, to prevent further damage [10].

V. Study, Analysis And Simulation Of The Impact Of Faults On Different Pvacs

In this section, several types of faults are analyzed and simulated, including faults with and without PS, as well as other cases of combined faults.For this reason, a PV array with 6x4 modules is simulated, consisting of six rows and four strings. Fig.6 shows an example of some faults considered in this paper for the 6 X4 SP PV array.

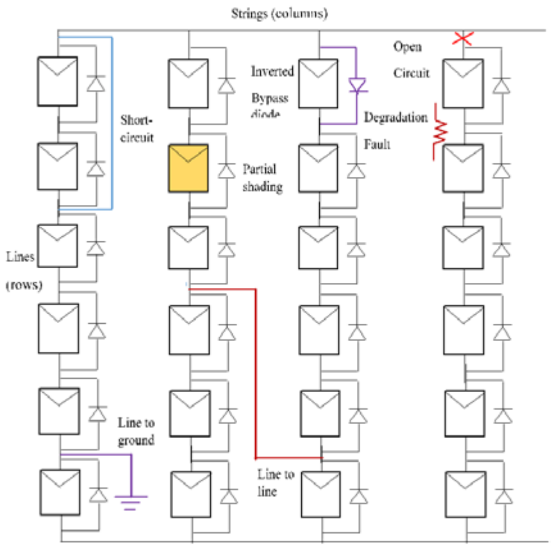

Fig.6: Example of some defects considered in the 6 X4 SP PV array

Different failure cases will be tested to evaluate their impact on each PVAC in order to determine which configuration is the most appropriate and resilient in these failure situations. To do this, we considered two cases: the case of a single fault and the case of multiple faults. The faults considered for performance analysis are bypass diode failure, short-circuit, ground faults, line- to-line, degradation and partial shading. All fault scenarios are examined and the obtained results are compared in terms of the maximum power point and relative power losses (ΔP_L (%)).

A.Partial shading fault (PS)

Table 4 shows the scenario of the PS fault.The comparison of the performance of the different PVACs in the caseof a PS fault is shown in Table 5. In this fault scenario, the S PVAC is the best configuration as it offers the highest performance and is followed by the TCT PVAC. For a better evaluation of various faults, different scenarios are tested with and without the presence of PS in the following sections.

B. Diode bypass fault

B.1. Diode bypass fault without PS

The bypass diode faults without PS consideration are summarized in Table6. The comparison of the performance of the different PVACs in the case of bypass diode failure without PS is shown in Table 7.

- In the case of a disconnected bypass diode under uniform operating conditions, there is no change, and it is obvious that all the PVACs have the same power value.
- In the case of a short-circuited or reversed bypass diode without PS, the S PVAC provides the highest value of power, followed by the SP PVAC and therefore the S configuration has the lowest power loss compared to all PVACs.

Table.4

Scenario of a PS fault.

Assignation	**Fault description**
F-PS	The last three modules of the third string are shaded at 300 W/m^2+ the last three modules of the fourth string are also shaded at 300 W/m^2

Table.5

PVACs performance in case of a PS fault.

PSfault	S		SP		TCT		HC		BL	
	P(W)	ΔP_L (%)	P(W)	ΔP_L (%)	P(W)	ΔP_L (%)	P(W)	ΔP_L (%)	P(W)	ΔP_L (%)
F-PS	**2391**	**33.5833**	1778	50.6111	1835	49.0277	1818	49.5	1823	49.3611

Table.6

Scenario of a diode bypass fault without PS.

Assignation	**Fault description**
F-DBP-D$_1$	The first bypass diode is disconnected from the first string
F-DBP-D$_2$	The first four bypass diodes are disconnected from the first string
F-DBP-SC$_1$	The first bypass diode is short-circuited in the first string
F-DBP-SC$_2$	The first four bypass diodes are short-circuited in the first string
F-DBP-I$_1$	The first bypass diode is inverted in the first string
F-DBP-I$_2$	The first four bypass diodes are inverted in the first string

Table.7

PVACs performance in case of a diode bypass fault without PS.

Diode bypass Fault	S		SP		TCT		HC		BL	
	P(W)	ΔP_L (%)	P(W)	ΔP_L (%)	P(W)	ΔP_L (%)	P(W)	ΔP_L (%)	P(W)	ΔP_L (%)
F-DBP-D$_1$	**3600**	-	**3600**	-	**3600**	-	**3600**	-	**3600**	-
F-DBP-D$_2$	**3600**	-	**3600**	-	**3600**	-	**3600**	-	**3600**	-
F-DBP-C$_1$	**3436**	4.5555	3224	10.4444	2856	20.6666	2942	18.2777	3018	16.1666
F-DBP-C$_2$	**3277**	8.9722	821.8	77.1722	569.3	84.1861	663.1	81.5805	637.4	82.2944
F-DBP-I$_1$	**3440**	4.4444	3237	10.0833	2875	20.1388	2960	17.7777	3035	15.6944
F-DBP-I$_2$	**2866**	20.3888	868.8	75.8666	612.7	82.9805	708.4	80.3222	682.2	81.05

B.2. Diode bypass fault with PS

Table 8 shows the bypass diode fault scenariosunderpartially shaded conditions.The comparison of the performance of the different PVACs in the case of bypass diode failure with PS is shown in Table 9.

- For the shading scenario F-PS_1, the S configuration exhibits the best performance, whereas in the second scenario (F-PS_2), the TCT PVAC provides the highest performance. So, it depends on the shading pattern, its intensity and its location.
- For the same shading scenarios in the presence of a fault in the bypass diode, the following can be observed:
- For the fault of a disconnected bypass diode, in the scenarios F-PS-DBP-D_1, F-PS-DBP-D_2, F-PS-DBP-D_3 and F-PS-DBP-D_4, the PVAC that provides the greatest power and the lowest relative loss is the TCT configuration followed by the HC PVAC.
- For the fault of a short-circuited bypass diode, in the scenarios F-PS-DBP-SC_1, F-PS-DBP-SC_2 and F-PS-DBP-SC_3, the PVAC that provides the greatest power and the lowest relative loss is the S configuration.
- For the fault of a shorted bypass diode, in the F-PS-DBP-SC_4 scenario, the PVAC that provides the greatest power and the lowest relative loss is the SP configuration.
- For the fault of an inverted bypass diode, in the F-PS-DBP-I_1 scenario, the PVAC that provides the greatest power and the lowest relative loss is the BL PVAC.
- For the fault of an inverted bypass diode, in the scenarios F-PS-DBP-I_2 and F-PS-DBP-I_3, the configuration that provides the greatest power and the lowest relative loss is the S PVAC
- For the fault of an inverted bypass diode, in the F-PS-DBP-I_4 scenario, the PVAC that provides the greatest power and the lowest relative loss is the HC PVAC.

Table.8
Scenario of a diode bypass fault with PS.

Assignation	Fault description
F-PS1	The first module of the first string is partially shaded at 400 W/m^2
F-PS2	The 6 modules of the first string are shaded at 400 W/m^2
F-PS-DBP-D_1	The first module of the first string is shaded at 400 W/$m^2$with its bypass diode disconnected
F-PS-DBP-D_2	The 6 modules of the first string are shaded at 400 W/m^2 with their diodes disconnected
F-PS-DBP-SC_1	The first module of the first string is shaded at 400 W/$m^2$with its bypass diode short-circuited
F-PS-DBP-SC_2	The 6 modules of the first string are shaded at 400 W/$m^2$with their bypass diodes short-circuited
F-PS-DBP-I_1	The first module of the first string is shaded at 400 W/m^2 with its reversed bypass diode
F-PS-DBP-I_2	The 6 modules of the first bypass diode string are shaded at 400 W/m^2 with their bypass diodes inverted
F-PS-DBP-SC_3	The first three modules of the first string are shaded at 400 W/$m^2$with their bypass diodes short-circuited, and the last three modules of the same string are shaded at 400 W/m^2 without fault in their bypass diodes
F-PS-DBP-SC_4	The first three modules of the first string are shaded at 400 W/m^2 with their bypass diodes shorted-circuited, and the last three modules of the same string are unshaded and faultless in their bypass diodes (without bypass faults and without shading in the three last modules)
F-PS-DBP-D_3	The first three modules of the first string are shaded at 400 W/$m^2$with their bypass diodes disconnected, and the last three modules of the same string are shaded at 400 W/m^2 without fault in their bypass diodes
F-PS-DBP-D_4	The first three modules of the first string are shaded at 400 W/m^2 with their bypass diodes disconnected, and the last three modules of the same string are unshaded and faultless in their bypass diodes (without bypass faults and without shading in the three last modules)
F-PS-DBP-I_3	The first three modules of the first string are shaded at 400 with their bypass inverted, and the last three modules of the same string are shaded at 400 W/m^2 without fault in their bypass diodes
F-PS-DBP-I_4	The first three modules of the first string are shaded at 400 W/$m^2$with their bypass diodes inverted, and the last three modules of the same string are unshaded and faultless in their bypass diodes (without bypass faults and without shading in the three last modules)

Table.9
PVACs performance in case of a diode bypass fault with PS.

Faults	S		SP		TCT		HC		BL	
	P(W)	ΔP_L (%)	P(W)	ΔP_L (%)	P(W)	ΔP_L (%)	P(W)	ΔP_L (%)	P(W)	ΔP_L (%)
F-PS1	**3432**	4.6666	3211	10.8055	3121	13.3055	3059	15.0277	3012	16.3333
F-PS2	1672	53.5555	2936	18.4444	**3121**	13.3055	3059	15.0277	3012	16.3333
F-PS-DBP-D_1	694.7	80.7027	688.1	80.8861	**697.8**	80.6166	694.1	80.7194	688.1	80.8861
F-PS-DBP-D_2	694.7	80.7027	688.1	80.8861	**697.8**	80.6166	694.1	80.7194	688.1	80.8861
F-PS-DBP-SC_1	**3436**	4.5555	3224	10.4444	2856	20.6666	2942	18.2777	3018	16.33
F-PS-DBP-SC_2	**684.1**	80.9972	0	100	0	100	0	100	0	100
F-PS-DBP-I_1	1672	53.5555	2936	18.4444	2874	20.1666	2960	17.7777	**3012**	16.3333
F-PS-DBP-I_2	**684.7**	80.9805	1.989	99.9447	1.991	99.9446	1.998	99.9445	1.989	99.9447
F-PS-DBP-SC_3	**688.3**	80.8805	678.7	81.1472	653	81.8611	675.1	81.2472	666.5	81.4861
F-PS-DBP-SC_4	694.2	80.7166	**1053**	70.75	979.4	72.7944	1035	71.25	1024	71.555
F-PS-DBP-D_3	693.2	80.7444	688.1	80.8861	**697.8**	80.6166	694.1	80.7194	688.1	80.8861
F-PS-DBP-D_4	698.8	80.5888	701.8	80.5555	**1218**	66.1666	993.8	72.3944	717.3	80.075
F-PS-DBP-I_3	**688.5**	80.875	679.6	81.1222	655.9	81.7805	676.2	81.2166	668.6	81.4277
F-PS-DBP-I_4	694.5	80.7083	701.8	80.5055	969.7	73.0638	**989.6**	72.5111	717.3	80.075

C. Short-circuit fault with and without PS

Complex partial shading scenario which is illustrated in Table 10 is used to evaluate short-circuit fault under complex PS conditions.Table11 shows the short-circuit fault with and without PS.

The comparison of the performance of the different PVACs in the case of short-circuits failure with and without PS is shown in Table 12:

- In all the scenarios of short-circuited modules with PS, the S PVAC presents the best performance in terms of power and losses (i.e. the highest power and the lowest loss) and it is followed by the SP PVAC which comes in second position.
- In this default scenario, the S PVAC is the best configuration as it offers the highest performance in terms of maximum power and losses, followed by the SP PVAC.

Table.10
Complex PS scenario.

	String 1	String 2	String 3	String 4
Row 1	1000 W/m^2	1000 W/m^2	500 W/m^2	1000 W/m^2
Row 2	300 W/m^2	1000 W/m^2	600 W/m^2	1000 W/m^2
Row 3	400 W/m^2	300 W/m^2	1000 W/m^2	1000 W/m^2
Row 4	1000 W/m^2	200 W/m^2	800 W/m^2	200 W/m^2
Row 5	600 W/m^2	500 W/m^2	1000 W/m^2	1000 W/m^2
Row 6	200 W/m^2	200 W/m^2	1000 W/m^2	400 W/m^2

Table.11
Scenario of a short-circuit fault with and without PS.

Assignation	**Fault description**
F-SC1	The first module of the first string is short-circuited but without shading
F-PS-SC1	The first module of the 1st string is short-circuited without shade and the 1st module of the last string is shaded at 400 W/m^2 but without fault in the bypass diode
F-SC2	The first four modules of the last string are short-circuited
F-PS-SC2	The first four modules of the last string are short-circuited and shaded at 200 W/m^2, 300 W/m^2, 400 and W/m^2 500 W/m^{2}respectively
F-PS-SC3	The first four modules of the last string are short-circuited and shaded at 200 W/m^2, 300 W/m^2, 400 and W/m^2 500 W/m^{2}respectively + The first four modules of the third string are shaded at 200 W/m^2, 300 W/m^2, 400 W/m^{2}and 500 W/m^2 respectively
F-PS-SC4	The first four modules of the last string are short-circuited without shading + The first four modules of the third string are shaded at 200 W/m^2, 300 W/m^2, 400 W/m^{2}and 500 W/m^2 respectively
F-CPS-WSC	Shading scenario of table10 without short-circuit fault.
F-CPS-SC	Shading scenario of table10 + The first four modules of the last string are short-circuited

Table.12
PVACs performance in cases of a short-circuit fault with and without PS.

SC Faults	S		SP		TCT		HC		BL	
	P(W)	ΔP_L (%)	P(W)	ΔP_L (%)	P(W)	ΔP_L (%)	P(W)	ΔP_L (%)	P(W)	ΔP_L (%)
F-SC1	**3436**	4.5555	3224	10.4444	2856	20.6666	2942	18.2777	3018	16.1666
F-PS-SC1	**3248**	9.7777	3038	15.6111	2856	20.6666	2847	20.9166	2894	19.6111
F-SC2	**2847**	20.9166	821.8	77.1722	573.7	84.0638	663.1	81.5805	637.4	82.2944
F-PS-SC2	**2847**	20.9166	821.8	77.1722	573.7	84.0638	663.1	81.5805	637.4	82.2944
F-PS-SC3	**1973**	45.1944	758.1	78.9416	573.7	84.0638	662.6	81.5944	637.1	82.3027
F-PS-SC4	**1973**	45.1944	758.1	78.9416	573.7	84.0638	662.6	81.5944	637.1	82.3027
F-CPS-WSC	1452	59.6666	1551	56.9166	1716	52.3333	1707	52.5833	**1731**	51.9166
F-CPS-SC	**1085**	69.8611	690.3	80.825	508.5	85.875	535.1	85.1361	527.9	85.3361

D. Degradation fault

D.1. Degradation faults without PS

Table 13 shows the degradation fault. The comparison of the performance of the different PVACs in the case of degradation failure is shown in Table 14.

D.2. Degradation faults with partial shading

In this fault scenario, the S configuration is the most efficient PVAC as it offers the highest performance, followed by the SP configuration.

Table 15 shows the degradation faults with partial shading. The comparison of the performance of the different PVACs in the case of a degradation fault with PS is shown in Table 16.

E. Ground faults

Table 17 shows the ground fault. The comparison of the performance of the different PVACs in the case of a ground fault is shown in Table 18.

Table.13
Scenario of a degradation fault without PS.

Assignation	**Fault description**
F-DEG-1	This fault is represented by a resistance of 2 ohms between the first and second modules of the first string
F-DEG-2	This fault is represented by a resistance of 2 ohms between the first and second modules of the first string and a resistance of 6 ohms between the second and third modules of the second string

Table.14
PVACs performance in case of a degradation fault without PS.

Degradation fault	S		SP		TCT		HC		BL	
	P(W)	ΔP_L (%)	P(W)	ΔP_L (%)	P(W)	ΔP_L (%)	P(W)	ΔP_L (%)	P(W)	ΔP_L (%)
F-DEG-1	**3561**	1.0833	3555	1.25	3531	1.9166	3538	1.7222	3545	1.5277
F-DEG-2	**3441**	4.4166	3403	5.4722	3350	6.9444	3375	6.25	3353	6.8611

Table.15
Scenario of a degradation fault with PS.

Assignation	**Fault description**
F-DEG-PS1	Degradation fault in the first string (resistance of 2 ohms between the first and second modules) + the first two modules of the first string are shaded at 500 W/m^2 and 500 W/m^2 respectively
F-DEG-PS2	Degradation fault in the first string (2 ohms between the first and second modules) + the first string is not shaded + the first two modules of the second string are shaded at 500 W/m^{2}and 500 W/m^2 respectively
F-DEG-PS3	Degradation fault in the first string (2 ohms between the first and the second module) + The first two modules of the first string and also the second first modules of the second string are shaded at 500 W/m^2 and 500 W/m^2
F-WDEG-PS	The first two modules of the first string and also the second first modules of the second string are shaded at 500 W/m^{2}and 500W/m^2 respectively without defect of degradation

Table.16
PVACs performance in case of a degradation fault with PS.

Degradation fault	S		SP		TCT		HC		BL	
	P(W)	ΔP_L (%)	P(W)	ΔP_L (%)	P(W)	ΔP_L (%)	P(W)	ΔP_L (%)	P(W)	ΔP_L (%)
F-DEG-PS1	**3200**	11.1111	3051	15.25	3165	12.0833	3073	14.6388	3137	12.8611
F-DEG-PS2	**3200**	11.1111	3030	15.8333	3148	12.5555	3110	13.6111	3127	13.1388
F-DEG-PS3	**2785**	22.6388	2362	34.3888	2445	32.0833	2420	32.7777	2402	33.2777
F-WDEG-PS	**2829**	21.4166	2365	34.3055	2447	32.0277	2423	32.6944	2405	33.1944

Table.17
Scenario of a ground fault.

Assignation	**Fault description**
F-GRD-1	This fault is located between the first and the second module of the first string and also between the second and the third module of the second string

Table18.
PVACs performance in case of a ground fault.

Ground faults	S		SP		TCT		HC		BL	
	P(W)	ΔP_L (%)	P(W)	ΔP_L (%)	P(W)	ΔP_L (%)	P(W)	ΔP_L (%)	P(W)	ΔP_L (%)
F-GRD-1	2634	26.8333	**3237**	10.0833	2856	20.6666	2986	17.0555	3018	16.1666

F. Line to line fault

Table19 shows the line-to-line fault.The comparison of the performance of the different PVACs in the case of a line-to-line fault is shown in Table 20.

In this fault scenario, the SP PVAC is the best configuration because it offers the highest power and is followed by the BL PVAC.

G. Open circuit fault

F-OPC:The fifth module of the third string is disconnected.
The series configuration is poorly suited to this type of fault, the TCT and HC PVACs provide the highest powers with lower losses

H. Multiple faults

Table 21 shows the cases of multiple faults.The comparison of the performance of the different PVACs in the case of multiple faultsis shown in Table 22.

- In the case of multiple faults (scenario F-MLP_1, F-MLP_2 and F-MLP_3), we notice that it is the SP PVAC which presents the best performance.

- In the case of multiple faults (scenario F-MLP_4 and F-MLP_5), we notice that it is the configuration S that presents the best performance.

Table.19
Scenario of a line-to-line fault.

Assignation	**Fault description**
F-LL-1	In this fault, the wire is connected between the first and second modules of the first string and also between the second and third modules of the second string

Table.20
PVACs performance in case of a line-to-line fault.

Line to line fault	S		SP		TCT		HC		BL	
	P(W)	ΔP_L (%)	P(W)	ΔP_L (%)	P(W)	ΔP_L (%)	P(W)	ΔP_L (%)	P(W)	ΔP_L (%)
F-LL-1	2634	26.8333	**3237**	10.0833	2856	20.6666	2986	17.0555	**3018**	16.1666

Table.21
Scenario of multiple faults.

Assignation	**Fault description**
F-MLP1	The last three modules of the third string are shaded at 300 W/m^2. The last three modules of the fourth string are shaded at 300 W/m^2 + the first three modules of the third string are shorted and the first three modules of the fourth string are shorted
F-MLP2	The last three modules of the 3rd string are shaded at 300 W/m^2 and the last three modules also of the fourth string are shaded at 300 W/m^2 + the first three modules of the third string and the first three modules of the fourth string are short-circuited + line to ground fault in the first string between the first and second modules and in the second string between the 2nd and third modules)
F-MLP3	The last three modules of the 3rd string are shaded at 300 W/m^2 and the last three modules also of the fourth string are shaded at 300 W/m^2 + the first three modules of the third string and the first three modules of the fourth string are short-circuited + a resistance of 6 ohms between the first and second modules of the first string
F-MLP4	The last three modules of the 3rd string are shaded at (100 W/m^2,200 W/m^{2}and 300 W/m^2) respectively and the last three modules of the fourth string are shaded at (400 W/m^2,500 W/m^{2}and 600 W/m^2) respectively + short circuit in the first three modules of the third and fourth string + a resistor of 6ohms between the 1st and 2nd modules of the first string
F-MLP5	The first four modules of the last string are short-circuited without shadowing + The first four modules of the third string are shadowing at 200 W/m^2, 300 W/m^2, 400 W/m^{2}and 500 W/m^{2}respectively + degradation fault (represented by an ohm resistance of 6 in the last string between 5th and 6th modules)

Table.22
PVACs performance in cases of multiple faults.

Combined faults	S		SP		TCT		HC		BL	
	P(W)	ΔP_L (%)	P(W)	ΔP_L (%)	P(W)	ΔP_L (%)	P(W)	ΔP_L (%)	P(W)	ΔP_L (%)
F-MLP1	1186	67.0555	**1223**	66.0277	1039	71.1388	1087	69.8055	1086	69.8333
F-MLP2	430.3	88.0422	**1223**	66.0277	1039	71.1388	1087	69.8055	1086	69.8333
F-MLP3	1121	68.8611	**1221**	66.0833	1039	71.1388	1087	69.8055	1086	69.8333
F-MLP4	**1279**	64.4722	1233	65.75	1077	70.0833	1092	69.6666	1094	69.6111
F-MLP5	**1955**	45.6944	987.4	72.5722	560.8	84.4222	671.9	81.3361	638.8	82.2555

VI. Results And Discussion

In this study, a thorough comparative analysis of faults and their impact on the efficiency of various PV interconnection schemes, including S, SP, HC, BL, and TCT are presented.
- The TCT and HC PVACs can improve power generation in open circuit faults. Thus, in the presence of PS and without any other faults, the TCTconnection is considered the most optimal PVAC and shows the best performance.
- In case of fault, the S PVAC presents the best performance and the SP PVAC comes in second in terms of performance. Except for a few certain situations where the results change.
- The TCT PVAC which presented the best performance in the majority of cases of shading, suffered from serious performance degradation.
- Under multiple faults, SP and S PVACs outperform other interconnections, but the SPPVAC is the most adequate.
- The performance of some PVACs under faulty conditions with the presence of PS may change in some situations compared to faults without PS.
- The performance of the various PVACs varies depending on the scenario used, i.e. the power generated varies depending on the location of the fault, the type of fault, whether the fault occurs with PS, or without PS.

VII. Conclusion

This paper provides a comprehensive examination of the impact of faults on the performance of various PVACs such as S, SP, HC, BL and TCT.
The performance of each PVACwas assessed under typical fault conditions such as partial shading, open-circuit, degradation, short circuit, bypass diode failure, line to line and line to ground.A case of multiple faults in a PV array under uniform irradiance and PS is also investigated to evaluate their impact on the various PV interconnections considered.The different PVACs have been tested and analyzed under several fault scenarios in order to identify the most resilient PVACunder fault conditions, allowing for improvements in system performance by optimizing the power of the appropriatePVAC.
This study helps in selecting the PVACthat is the least sensitive to the various faults, thereby improving power generation.
In future work, we recommend practical verification of these PVACs under fault conditions and the investigation of additional fault types.

References

[1] S. Gul, A. UlHaq, M.Jalal, A. Anjum, I. Ullah Khalil, A Unified Approach for Analysis of Faults in Different Configurations of PV Arrays and Its Impact on Power Grid. Energies 13 (156) (2020).

[2] D.S. Pillai, F .Blaabjerg, N.Rajasekar, A Comparative Evaluation of Advanced Fault Detection Approaches for PV Systems. IEEE Journal of photovoltaics 9 (2) (2019).

[3] S. R.Madeti, S.N. Singh, A comprehensive study on different types of faults and detection techniques for solar photovoltaic system. Solar Energy 158 (2017) 161–185.

[4] A. Triki-Lahiani, A. Bennani-Ben Abdelghanib, I. SlamaBelkhodja, Fault detection and monitoring systems for photovoltaic installations: A Review. Renewable and Sustainable Energy Reviews 82 (2018) 2680–2692.

[5] D.S. Pillai, N. Rajaseka, A comprehensive review on protection challenges and fault diagnosis in PV systems. Renewable and Sustainable Energy Reviews 91 (2018) 18–40.

[6] F. Belhachat, C. Larbes, Modeling, analysis and comparison of solar photovoltaic array configurations under partial shading conditions. Solar Energy 120 (2015) 399–418. https://doi.org/10.1016/j.solener.2015.07.039

[7] F. Belhachat, C. Larbes, Comprehensive review on global maximum power point tracking techniques for PV systems subjected to partial shading conditions. Solar Energy 183 (2019) 476–500. https://doi.org/10.1016/j.solener.2019.03.045.

[8] F. Belhachat, C. Larbes, “A review of global maximum power point tracking techniques of photovoltaic system under partial shading conditions”, Renewable and Sustainable Energy Reviews 92 (2018) 513–553.https://doi.org/10.1016/j.rser.2018.04.094

[9] F. Belhachat, C. Larbes, Global Maximum Power Point Tracking Based on ANFIS Approach for PV Array Configurations under Partial Shading Conditions. Renewable and Sustainable Energy Reviews 77 (2017) 875–889.https://doi.org/10.1016/j.rser.2017.02.056

[10] F. Belhachat, C. Larbes, R. Bennia, Recent advances in fault detection techniques for photovoltaic systems: An overview, classification and performance evaluation, Optik-International Journal for Light and Electron Optics 306 (2024) 171797. https://doi.org/10.1016/j.ijleo.2024.171797.

Faiza Belhachat received the electronic engineering degree from the University of Science and Technology Houari Boumedienne (USTHB), Algiers, Algeria; the “Magister” degree in electronic-solar electricity- from the Ecole Nationale Polytechnique (ENP), Algiers, Algeria; and also the Doctorate in Science in electronic engineering from the ENP. Her current research interests include photovoltaic systems, intelligent control, and embedded systems.

Cherif Larbes received the “Ingeniorat d’Etat” degree in electronics from Ecole Nationale Polytechnique, Algiers, Algeria, in 1985 and the Ph.D. degree in engineering from the University of Lancaster, UK, in 1990. He is currently a FullProfessor with the Department of Electronics, Ecole Nationale Polytechnique, Algiers, Algeria. He is the director of the “Dispositifs de Communication et de Conversion Photovoltaïque” Research Laboratory (LDCCP). His current research interests include intelligent control, power converters, electrical machine drives and photovoltaic systems. He authored over 100 journal and conference papers.

Methylene Blue degradation using plasma: A comparative study between the microwave plasma jet over water surface and the nanosecond pulsed discharge in gas bubbles in water

Aloui Nadir and Belgacem Ibtissem

Abstract—This paper investigates the Methylene Blue degradation using two common reactors: the nanosecond pulsed discharge in oxygen bubbles and the Argon Microwave plasma jet above the treated solution. The aim of this study is to compare the evolution of the reactors performance when the electrical conductivity increases. In deionized water, the Methylene Blue degradation rate and the energy efficiency (0.19 min^{-1} and 99 mg/kWh, respectively) in the Nanosecond pulsed discharge configuration were significantly higher than the Argon microwave plasma jet (0.08 min^{-1} and 10 mg/kWh). However, when the solution electrical conductivity is increased from 5 to 200 µS/cm, the energy efficiency of the nanosecond pulsed discharge drops significantly by ∼82%, whereas the performance of the microwave plasma jet reactors decreases by ∼37% only for a greater variation of the electrical conductivity of the solution (from 5 to 10 000 µS/cm). Under these conditions the efficiency of both reactors becomes comparable, suggesting the necessity to consider various parameters to compare the reactors efficiency.

***Keywords*—Nanosecond pulsed discharge, Microwave plasma jet discharge, Methylene Blue, electrical conductivity, energy efficiency.**

Nomenclature

NPD	Nanosecond Pulsed Discharge .
Ar MWPJ	Argon Microwave Plasma Jet .
MB	Methylene Blue.

I. Introduction

Water pollution is the result of introducing harmful substances into water bodies, causing degradation in their quality. This issue is becoming even more serious due to the increase in human activities such as urbanization [1] and industrialization [2], which introduce high levels of various pollutants into water resources, often referred to as "emergent pollutants" [3–6]. The emergent contaminants refer to a broad of compounds present in wastewater at low concentrations (ng/L-µg/L), that not have been previously monitored or regulated but are currently recognized as an important contributors to water pollution. These pollutants could classify into several groups such as: pharmaceuticals, personal care products, pesticides, micro plastics, industrial chemicals and hormone; also, they can be natural or synthetic substances [7, 8]. Despite the lack of knowledge about them, the emergent contaminants are identified as a potential threatens for both environment and human health [3, 9]. Therefore, the detection and the elimination of emergent contaminants is a crucial task nowadays. Recently, the plasma based technology has been proposed as an alternative to eliminate emergent contaminants from wastewater. In fact, when the plasma is coupled with water, large broad of reactive species such as Ozone (O_3) [10], hydrogen peroxide (H_2O_2) [10, 11] hydroxyl radical (OH) [12] oxygen atoms (O) [13], among others could be produced making it a promising technology for wastewater treatment. Effectively, the plasma showed a high potential to eliminate emergent pollutants such as: dyes [14, 15], pharmaceuticals products [16] and even pesticides [17]. However, plasma-based water treatment remains a relatively new technology that requires further development before it can be effectively used at larger scale. At this stage, one of the most critical tasks that should be considered to achieve this purpose is to evaluate the plasma technology for water treatment in order to establish a road map for further research. In this context, Malik, 2010 [18] made a comparative study between 27 types of plasma reactors to assess the most efficient configuration for water treatment. In the mentioned work, the energy yield at 50% was used as parameter to assess the plasma reactors performance. The results achieved by this study showed that the reactors efficiency depends on several parameters like the gas composition, the liquid distribution, i.e. deep layer, thin film or water sprayed and finally the signal of the power supply (pulse, DC or AC). Overall, the pulsed discharges in the gas phase and in contact with thin layers or fine droplets of solution are the most efficient reactors. However, despite the very important conclusions highlighted by Malik, 2010 [18], the comparison between plasma reactors should be extended to take into consideration other factors. In the present study, a different approach is adopted to compare the performance of two widely employed plasma-based water treatment reactors: the nanosec-

Manuscript received June 16, 2024; revised December 23, 2024.

N. Aloui is with LRS-EAU Laboratory, Ecole Nationale Polytechnique, Algiers, ALGERIA (e-mail: nadir.aloui@g.enp.edu.dz)
I. Belgacem is with LRS-EAU Laboratory, Ecole Nationale Polytechnique, Algiers, ALGERIA (e-mail: ibtissem.belgacem@gmail.com)

Digital Object Identifier (DOI): 10.53907/enpesj.v4i2.272

ond pulsed discharge (NPD) reactor operating in gas bubbles within water and the argon microwave plasma jet (Ar MWPJ) in direct contact with the water surface. This comparison focuses on evaluating how the performance of these reactors evolves under varying operating conditions, particularly the electrical conductivity of the treated solution. Electrical conductivity was chosen as the primary variable because, in practical scenarios, the electrical conductivity of wastewater is significantly higher than that of deionized water. By systematically altering this parameter, the study aims to bridge the gap between controlled laboratory conditions and real-world applications, providing insights into the adaptability and efficiency of these reactors under conditions that are similar to actual wastewater compositions. This work highlights the critical role of solution conductivity in Plasma-based water purification, offering a deeper understanding of the challenges facing this technology.

II. METHODS AND MATERIALS

In this study, we investigate the Methylene Blue (MB) degradation at initial concentration of 5 and 10 mg/L using NPD in O_2 bubbles and the Ar MWPJ above water surface, respectively.

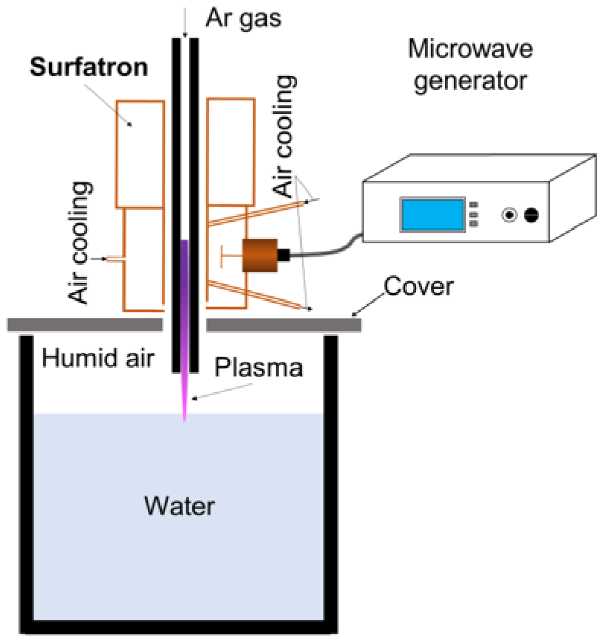

Fig. 1: Schematic of the the Ar MPWJ setup used to degrade MB solution.

The Fig.1 shows the experimental setup of the Ar MWPJ. The energy provided by the microwave generator (SAIREM GMS200W) operating at 2.45 GHz is coupled to the Argon gas (purity >99.995%) using a Surfatron device (SAIREM S-WAVE 6 A). The Argon gas is supplied at a flow rate of 0.5 L/min through a quartz tube with inner and outer diameters of 2 mm and 6 mm, respectively. The experiments are conducted using a closed cell covered with an aluminum circular plate. The quartz tube is inserted into the closed cell through a 7 mm diameter hole in the aluminum plate to generate the MWPJ in contact with 100 mL of MB solution. During the experiments, the compressed air is used to cool the Surfatron device and the quartz tube. The microwave power is maintained at 100 W throughout the process.

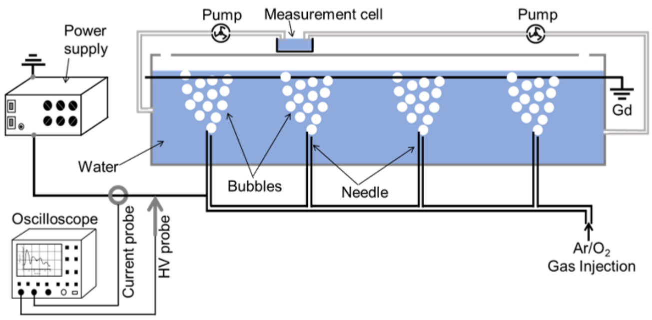

Fig. 2: Schematic of the the NPD in O_2 bubbles setup used to degrade MB solution.

Regarding the NPD in O_2 bubbles we used the setup shown in (Fig.2). The discharge is produced using a nanosecond negative polarity pulsed power supply (NSP 120-20-N-500-TG-H, Eagle Harbor Technologies) at an amplitude of -20 kV, a pulse width of 500 ns and a frequency of 1kHz. The high voltage was connected to four hollow-needles-like (inner and outer diameter of 0.3 and 0.5 mm, respectively), whereas the grounded electrode was a stainless-steelwire (1 mm diameter) placed at 8 mm above the needles. A mass flow controller was used to inject O_2 (purity >99.995%) into MB solution through the hollow needles at flow rate of 4 L/min (1 L/min per needle). The volume of the MB solution was 300 mL. 200 mL was filled in the cylindrical cell where the electrodes are mounted, whereas the remaining 100 mL is filled in cell to perform the absorbance measurements. Two pumps (Ismatec™ MS-2/6 Reglo Analog Pump) were utilized at flow rate of 50 mL/min to ensure the MB solution recirculation.

In both configurations, the MB degradation is monitored using an UV-Vis absorption spectrophotometer (Cary 5000 UV–Vis-NIR, Agilent). The decoloration efficiency is assessed based on the absorbance intensity at 664 nm, and the MB concentration was deduced based on a calibration curve. The KCl was used to alter the solution electrical conductivity and the H_2O_2 production is measured is distilled water (without MB) using drop count titration method based on Sodium Thiosulfate titrant.

III. RESULTS AND DISCUSSION

A. MB degradation

The (Fig.3a) shows the evolution of the normalized absorbance (at 664 nm) as function of plasma processing time for both configurations the Ar MWPJ and the NPD in O_2 bubbles. The results show that the MB degradation efficiency is considerably higher in the NPD than the Ar MWPJ; the $t_{50\%}$ which represents the time required to eliminate 50% of MB molecules is 15 min in the Ar MWPJ configuration. Whereas in the NPD reactor the $t_{50\%}$ is only 5min.

To estimate the MB degradation rate, a kinetic study is carried out. Since the MB concentration decreases exponentially during processing (Fig.3a), we assume that its degradation is described by first order kinetics (1).

$$-ln(C_t/C_O) = kt \tag{1}$$

With C_t (mg/L) is MB concentration at time t, C_0 (mg/L) is the MB initial concentration and k (min^{-1}) is the first order rate constant.

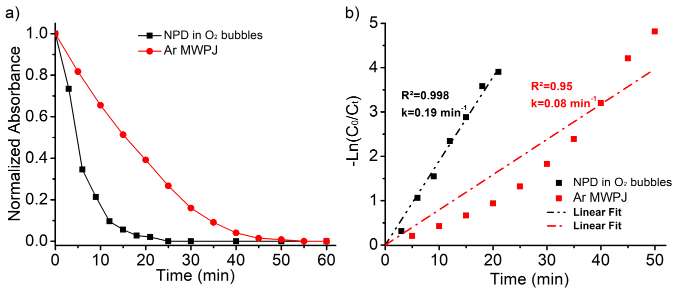

Fig. 3: (a) Temporal evolution of the normalized absorbance (at 664 nm) of MB solution in the Ar MWPJ and NPD in O_2 bubbles reactors. (b) First order kinetics of MB degradation solution in the Ar MWPJ and NPD in O_2 bubbles reactors.

The results of the kinetic study (Fig.3b) show that the correlation coefficient R^2 is 0.95 and 0.998 in the Ar MWPJ and the nanosecond pulsed discharge configurations, respectively. This confirms our assumption indicating that MB degradation is represented by first-order kinetics.

The constant degradation rate in Ar MWPJ is 0.08 min^{-1}, whereas, in the NPD in O_2 bubbles, it is 0.19 min^{-1}. These results demonstrate that the MB degradation in this latter configuration is $\sim$2.5 time faster than the Ar MWPJ. To understand the reason behind the superiority of the NPD in MB degradation, the H_2O_2 production in water (without MB) is measured during plasma processing. The presence of H_2O_2 in water indicates the production of hydroxyl (OH) radicals which are known to be responsible for the degradation of MB [19, 20].

The (Fig.4) shows the H_2O_2 production as function of plasma processing in both configurations. In the NPD in O_2 bubbles, the H_2O_2 production increases linearly after 30 min of processing to reach $\sim$54 mg/L with rate of $\sim$1.9 mg/Lmin. On the other hand, in the Ar MWPJ, the H_2O_2 production reaches 20 mg/L after 40 min of processing with rate of $\sim$0.5 mg/Lmin. After this period no further increase in H_2O_2 production is registered.

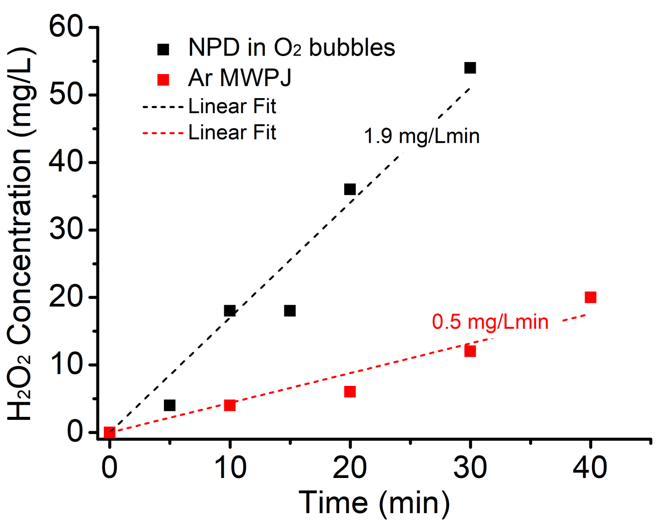

Fig. 4: H_2O_2 production using the NPD in O_2 bubbles and the Ar MWPJ.

The high production rate of H_2O_2 in the NPD reactor indicate that this configuration produces more OH radicals, explaining thus, the high MB degradation rate observed in this reactor. In fact, when the NPD in O_2 bubbles is used, the oxygen atoms could be produced (2) to generate supplementary OH radicals (3) and ozone (O_3) (4) [21]. This latter (O_3) play an important role in MB degradation [22] by a direct oxidization or by generating more OH radicals when reacting with H_2O_2 (5) [23]. Overall, the production of O atoms and O_3 in the NPD configuration can enhance the OH production which is beneficial for MB degradation. Besides the ozone production, the generation of the discharge in gas bubbles enhances the mass transfer of reactive species to the liquid bulk, making this configuration more efficient.

$$e + O_2 \rightarrow 2O + e \tag{2}$$

$$O + H_2O \rightarrow 2OH \tag{3}$$

$$O + O_2 \rightarrow O_3 \tag{4}$$

$$O_3 + H_2O_2 \rightarrow OH + HO_2 + O_2 \tag{5}$$

B. *Energy efficiency*

The energy yield at 50% ($Y_{50\%}$) is used in this study to assess the energy efficiency of the studied configurations (NPD in O_2 bubbles and the Ar MWPJ). This parameter represents the amount of eliminated contaminants per unit of delivered energy at 50% degradation of MB, and it is expressed by equation (6) [18]:

$$Y_{50\%} = \frac{V \times C_0 \times \frac{C_0 - C}{C_0}}{P \times t_{50\%}} \tag{6}$$

With V(L) is the volume of MB solution, C_0(mg/L) is the initial concentration, C(mg/L) is the MB concentration at 50% of conversion, P(kW) is the delivered power, and $t_{50\%}$(h) is the time to reach 50% of MB degradation.

The delivered power by the microwave generator was set at 100 W, whereas in the NPD in $O2$ bubbles, we measured the dissipated power using a monitor that was added to the plug wall where the pulse generator is connected. The consumed power in that case was 181 W.

The table I shows once again the superiority of the NPD in O_2 bubbles compared to Ar MWPJ; the $Y_{50\%}$ in NPD in O_2 bubbles (99 mg/kWh) is 10 times higher than the Ar MWPJ (10 mg/kWh). This significant difference between the two reactors is not attributed only the fast MB degradation in the NPD configuration, but also due to the physic of both plasmas. In the Ar MWPJ an important portion of power is dissipated to heat the surrounding air, resulting in a local temperature increase. This is evident from the previous experimental results who indicated that the plasma gas temperature can reach very high values (few thousands of Kelvin) [15, 24, 25]. On the other hand, in the NPD, the short duration of the voltage pulse allows only electrons the gain a high energy to initiate the ionization process, whereas the heavier ions remains close to room temperatures [18]. This feature indicates that the NPD allows plasma ignition with less energy dissipation, explaining the high energy efficiency of this configuration.

Table. I

THE ENERGY YIELD ($Y_{50\%}$) OF THE NPD IN O_2 BUBBLES AND THE AR MPWJ

Configuration	$t_{50\%}$ (min)	P (W)	$Y_{50\%}$ (mg/kWh)
NPD in O_2 bubbles	5	181	99
Ar MWPJ	15	100	10

C. *The effect of electrical conductivity on the reactors performance*

Most of the previous studies investigated the plasma based water treatment using deionized water, but in reality the wastewaters exhibit very high electrical conductivities. Therefore, it is crucial to assess the reactors efficiency under conditions of high values of solution electrical conductivity. Herein, we investigate the impact of this parameter on the performance of the NPD in O_2 bubbles and the Ar MWPJ. It is worth to mention that during our experiments we observed that increasing the electrical conductivity beyond 200 µS/cm in the NPD configuration prevents plasma ignition, probably due to the fast current dissipation in the liquid [26]. On the other hand, the electrodeless design of the Ar MWPJ allowed increasing the solution conductivity to very high values (> 50 000 µS/cm) without altering the plasma jet ignition. At this stage, we believe that the Ar MWPJ is more suitable for highly conductive solutions.

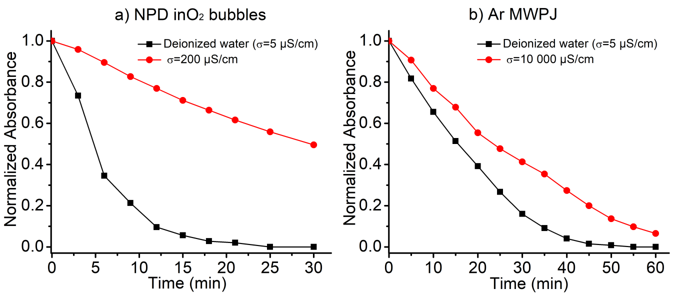

Fig. 5: Effect of the solution electrical conductivity on the MB degradation rate in: a) the NPD in O_2 bubbles, and b) the Ar MWPJ

The Fig.5a and Fig.5b illustrate the effect of the electrical conductivity on MB degradation in the NPD in O_2 bubbles and the Ar MPWJ, respectively. In the former configuration, increasing the electrical conductivity to 200µS/cm decreases the MB degradation rate considerably where the $t_{50\%}$ increases from 5 min at deionized water (5µS/cm) to 30 min at 200 µS/cm. this reduction could be explained by the fact that at high electrical conductivity the contact plasma-water is reduced (due to short plasma channels) which reduces the reactive species production. Regarding the Ar MWPJ configuration, the initial solution conductivity is adjusted at 10 000 µS/cm (for σ< 10- 000 µS/cm no significant change in the MB degradation rate is observed). At this electrical conductivity, the MB degradation rate decreases; the $t_{50\%}$ increases from 15 min at deionized water (5 µS/cm) to 24 min at 10 000 µS/cm. In fact, this reduction is considered minor compared to the significant increase in solution electrical conductivity. Moreover, the observed reduction in the MB degradation rate is not caused by the presence of ionic products in general, but mainly by Cl^- ions (Provided from KCl dissociation) that have an inhibitory effect on OH radicals [27–29].

The table II shows the variation of the energy yield ($Y_{50\%}$) as function of the electrical conductivity. The $Y_{50\%}$ in the NPD configuration drops significantly by 82% (from 99 to 17 mg/kWh) when the electrical conductivity is increased from 5 to 200 µS/cm, whereas in the Ar MWPJ, the $Y_{50\%}$ drops only by 37% to reach 6.3 mg/kWh when the electrical conductivity is increased to 10 000 µS/cm. Overall, the results discussed in this section suggest the possibility to use the Ar MWPJ configuration for solutions with high electrical conductivities. On the other hand, the NPD in O_2 bubbles loses its efficiency rapidly for small electrical conductivity variations. These observations highlight the necessity to consider different operating conditions to assess the reactors performance.

Table. II

THE EFFECT OF ELECTRICAL CONDUCTIVITY ON THE ENERGY YIELD ($Y_{50\%}$) IN THE NPD IN O_2 BUBBLES AND THE AR MWPJ CONFIGURATIONS.

Configuration	NPD in O_2 bubbles		Ar MPWJ	
conductivity (µS/cm)	5	200	5	10 000
$Y_{50\%}$(mg/kWh)	99	17	10	6.3

IV. CONCLUSION

In the present study, we investigated the MB degradation using two configurations: the NPD in O_2 bubbles and the Ar MWPJ above the water surface. In the deionized water, the NPD in O_2 bubbles demonstrated superior MB degradation because of its ability to generate higher concentration of reactive species such as O_3, O, OH and H_2O_2. Furthermore, the energy yield ($Y_{50\%}$) at 50% demonstrated that the energy efficiency in the NPD in O_2 is higher compared to the Ar MWPJ (99 vs 10 mg/kWh, respectively). Unlike the Ar MWPJ, where a significant portion of power is dissipated to heat to the surrounding environment, the NPD ensures plasma ignition with minimal power dissipation, making it highly effective in terms of energy efficiency.

the other hand, at high solution conductivities, the NPD configuration prevents plasma ignition which causes a significant drop of energy efficiency that decreases from 99 mg/kWh in deionized water to achieve 17 mg/kWh at 200 µS/cm, whereas the performance of the Ar MWPJ drops by 37% only (from 10 to 6.3 mg/kWh) when the electrical conductivity is increased to 10 000 µS/cm . These findings suggest the possibility to use Ar MWPJ configuration for high conductive solutions.

The results of this study reveal the complexity of the comparison task between plasma reactors, suggesting thus the necessity to take into consideration other parameters to properly estimate the reactors performance.

REFERENCES

[1] H. Rashid, M. M. Manzoor, S. Mukhtar, *et al.*, "Urbanization and its effects on water resources: An exploratory analysis," *Asian Journal of Water, Environment and Pollution*, vol. 15, no. 1, pp. 67–74, 2018.

[2] H. Hayzoun, C. Garnier, G. Durrieu, V. Lenoble, C. Bancon-Montigny, A. Ouammou, and S. Mounier, "Impact of rapid urbanisation and industrialisation on river sediment metal contamination," *Environmental monitoring and assessment*, vol. 186, pp. 2851–2865, 2014.

[3] C.-C. Lee, C.-Y. Hsieh, C. S. Chen, and C.-J. Tien, "Emergent contaminants in sediments and fishes from the tamsui river (taiwan): Their spatial-temporal distribution and risk to aquatic ecosystems and human health," *Environmental Pollution*, vol. 258, p. 113733, 2020.

[4] H. B. Quesada, A. T. A. Baptista, L. F. Cusioli, D. Seibert, C. de Oliveira Bezerra, and R. Bergamasco, "Surface water pollution by pharmaceuticals and an alternative of removal by low-cost adsorbents: A review," *Chemosphere*, vol. 222, pp. 766–780, 2019.

[5] D. Montes-Grajales, M. Fennix-Agudelo, and W. Miranda-Castro, "Occurrence of personal care products as emerging chemicals of concern in water resources: A review," *Science of the Total Environment*, vol. 595, pp. 601–614, 2017.

[6] J. Derksen, G. Rijs, and R. Jongbloed, "Diffuse pollution of surface water by pharmaceutical products," *Water Science and Technology*, vol. 49, no. 3, pp. 213–221, 2004.

[7] N. Morin-Crini, E. Lichtfouse, G. Liu, V. Balaram, A. R. L. Ribeiro, Z. Lu, F. Stock, E. Carmona, M. R. Teixeira, L. A. Picos-Corrales, *et al.*, "Worldwide cases of water pollution by emerging contaminants: a review," *Environmental Chemistry Letters*, vol. 20, no. 4, pp. 2311–2338, 2022.

[8] A. R. Bracamontes-Ruelas, L. A. Ordaz-Díaz, A. M. Bailón-Salas, J. C. Ríos-Saucedo, Y. Reyes-Vidal, and L. Reynoso-Cuevas, "Emerging pollutants in wastewater, advanced oxidation processes as an alternative treatment and perspectives," *Processes*, vol. 10, no. 5, p. 1041, 2022.

[9] R. K. Mishra, S. S. Mentha, Y. Misra, and N. Dwivedi, "Emerging pollutants of severe environmental concern in water and wastewater: A comprehensive review on current developments and future research," *Water-Energy Nexus*, 2023.

[10] P. Lukes, A. T. Appleton, and B. R. Locke, "Hydrogen peroxide and ozone formation in hybrid gas-liquid electrical discharge reactors," *IEEE Transactions on Industry Applications*, vol. 40, no. 1, pp. 60–67, 2004.

[11] A. Anpilov, E. Barkhudarov, Y. B. Bark, Y. V. Zadiraka, M. Christofi, Y. N. Kozlov, I. Kossyi, V. Kop'Ev, V. Silakov, M. Taktakishvili, *et al.*, "Electric discharge in water as a source of uv radiation, ozone and hydrogen peroxide," *Journal of Physics D: Applied Physics*, vol. 34, no. 6, p. 993, 2001.

[12] M. Sahni and B. R. Locke, "Quantification of hydroxyl radicals produced in aqueous phase pulsed electrical discharge reactors," *Industrial & engineering chemistry research*, vol. 45, no. 17, pp. 5819–5825, 2006.

[13] T. J. Manning, "Production of ozone in an electrical discharge using inert gases as catalysts," 2000.

[14] J. Diamond, J. Profili, and A. Hamdan, "Characterization of various air plasma discharge modes in contact with water and their effect on the degradation of reactive dyes," *Plasma Chemistry and Plasma Processing*, vol. 39, pp. 1483–1498, 2019.

[15] A. Hamdan, J.-L. Liu, and M. S. Cha, "Microwave plasma jet in water: Characterization and feasibility to wastewater treatment," *Plasma Chemistry and Plasma Processing*, vol. 38, pp. 1003–1020, 2018.

[16] M. Magureanu, D. Piroi, N. B. Mandache, V. David, A. Medvedovici, and V. I. Parvulescu, "Degradation of pharmaceutical compound pentoxifylline in water by non-thermal plasma treatment," *Water research*, vol. 44, no. 11, pp. 3445–3453, 2010.

[17] M. Magureanu, C. Bradu, and V. Parvulescu, "Plasma processes for the treatment of water contaminated with harmful organic compounds," *Journal of Physics D: Applied Physics*, vol. 51, no. 31, p. 313002, 2018.

[18] M. A. Malik, "Water purification by plasmas: Which reactors are most energy efficient?," *Plasma Chemistry and Plasma Processing*, vol. 30, pp. 21–31, 2010.

[19] L. O. de Brito Benetoli, B. M. Cadorin, V. Z. Baldissarelli, R. Geremias, I. G. de Souza, and N. A. Debacher, "Pyrite-enhanced methylene blue degradation in non-thermal plasma water treatment reactor," *Journal of hazardous materials*, vol. 237, pp. 55–62, 2012.

[20] R. Zhou, T. Zhang, R. Zhou, A. Mai-Prochnow, S. B. Ponraj, Z. Fang, H. Masood, J. Kananagh, D. McClure, D. Alam, *et al.*, "Underwater microplasma bubbles for efficient and simultaneous degradation of mixed dye pollutants," *Science of the Total Environment*, vol. 750, p. 142295, 2021.

[21] M. Magureanu, D. Piroi, F. Gherendi, N. B. Mandache, and V. Parvulescu, "Decomposition of methylene blue in water by corona discharges," *Plasma Chemistry and Plasma Processing*, vol. 28, pp. 677–688, 2008.

[22] L. Grabowski, E. Van Veldhuizen, A. Pemen, and W. Rutgers, "Breakdown of methylene blue and methyl orange by pulsed corona discharge," *Plasma Sources Science and Technology*, vol. 16, no. 2, p. 226, 2007.

[23] P. Lukes and B. R. Locke, "Plasmachemical oxidation processes in a hybrid gas–liquid electrical discharge reactor," *Journal of Physics D: Applied Physics*, vol. 38, no. 22, p. 4074, 2005.

[24] C. Schopp, F. Nachtrodt, H. Heuermann, U. W. Scherer, D. Mostacci, T. Finger, and W. Tietsch, "A novel 2.45 ghz/200 w microwave plasma jet for high temperature applications above 3600 k," in *Journal of Physics: Conference Series*, vol. 406, p. 012029, IOP Publishing, 2012.

[25] J. Amaro-Gahete, F. J. Romero-Salguero, and M. C. Garcia, "Modified surfatron device to improve microwave-plasma-assisted generation of rons and methylene blue degradation in water," *Chemosphere*, vol. 349, p. 140820, 2024.

[26] K.-Y. Shih and B. R. Locke, "Optical and electrical diagnostics of the effects of conductivity on liquid phase electrical discharge," *IEEE Transactions on Plasma Science*, vol. 39, no. 3, pp. 883–892, 2011.

[27] T. M. Elmorsi, Y. M. Riyad, Z. H. Mohamed, and H. M. Abd El Bary, "Decolorization of mordant red 73 azo dye in water using h2o2/uv and photo-fenton treatment," *Journal of Hazardous Materials*, vol. 174, no. 1-3, pp. 352–358, 2010.

[28] N.-y. Gao, Y. Deng, and D. Zhao, "Ametryn degradation in the ultraviolet (uv) irradiation/hydrogen peroxide (h2o2) treatment," *Journal of Hazardous Materials*, vol. 164, no. 2-3, pp. 640–645, 2009.

[29] R. Yuan, S. N. Ramjaun, Z. Wang, and J. Liu, "Concentration profiles of chlorine radicals and their significances in• oh-induced dye degradation: kinetic modeling and reaction pathways," *Chemical engineering journal*, vol. 209, pp. 38–45, 2012.

Aloui Nadir was born in Annaba, Algeria, in 1995. He received the Engineer's degrees in Hydraulic Engineering from Ecole Nationale Polytechnique (ENP) of Algiers in 2019. He is currently a Ph.D. student at the Hydraulic Department at the same Engineering School. His current research interests include interaction of plasma with liquid.

Belgacem Ibtissem Earned her Ph.D. degree from University of Science and Technology Houari Boumediene, Algiers, Algeria. Her current research interests include CFD, two phase flow and plasma interaction with two phase medium.